Sequential subspace optimization for nonlinear inverse problems with an application in terahertz tomography

Dissertation

zur Erlangung des Grades des
Doktors der Naturwissenschaften
der Fakultät Mathematik und Informatik
der Universität des Saarlandes

eingereicht im März 2017
in Saarbrücken

von

Anne Wald

UNIVERSITÄT
DES
SAARLANDES

Tag des Kolloquiums: 30.06.2017

Mitglieder des Prüfungsausschusses:

Vorsitzender: Professor Dr. Mark Groves

1. Berichterstatter: Professor Dr. Thomas Schuster

2. Berichterstatter: Professor Dr. Dr. h.c. mult. Alfred K. Louis

3. Berichterstatter: Professor Dr. Bernd Hofmann

Protokollführer: Dr. Steffen Weißer

Dekan: Professor Dr. Frank-Olaf Schreyer

Acknowledgements

First of all, I would like to express my sincerest gratitude towards my supervisor Professor Thomas Schuster. My decision to study mathematics was made when I attended his lectures “Höhere Mathematik für Ingenieure I, II” back in 2005 when I was a junior student at Saarland University. All the more it is a pleasure also to finish my studies in his Numerics group and I am deeply grateful for this opportunity and all his support.

Second, I want to thank Professor Alfred K. Louis for being the co-referee of this thesis and for his contributions to my mathematical education.

For his comments on the proof of Theorem 2.12, I want to express my gratitude to Heiko Hoffmann.

I want to thank Professor Ernst-Ulrich Gekeler for supervising my Bachelor and Master thesis in mathematics and Professor Karsten Kruse for supervising my Diploma thesis in physics. In this context, I also want to thank all my former colleagues and my co-authors Viktoria Wollrab and Daniel Riveline.

Also, I want to express my gratitude to my colleagues from the Numerics group, in particular Jens Tepe, whose research is strongly related to mine, for the joint work, but also to Julia Seydel, Dimitri Rothermel, Frederik Heber, Petra Schuster and Claudia Stoffer. For their friendship, but also for various mathematical discussions, I want to thank Philip Oberacker, Heiko Hoffmann, Christian Tietz, Robert Knobloch, Alexandra Lauer, Bernadette Hahn, Gaël Rigaud, Jonas Vogelgesang, and Aref Lakhal.

A special thanks goes to Philip Oberacker and Heiko Hoffmann for proof-reading this thesis and to Alice Oberacker for helping me with the parallelization in my codes.

Last but not least I thank my family (especially my parents Jutta and Ulrich, my brother Philip, and my grandmother Helga) and my beloved partner Philip Oberacker for their constant support.

Contents

List of Tables ix

List of Figures xi

Abstract xiii

Zusammenfassung xiii

Introduction 1

1. Sequential subspace optimization 7
- 1.1. SESOP for linear inverse problems 7
  - 1.1.1. Regularizing sequential subspace optimization 11
  - 1.1.2. RESESOP with two search directions 12
- 1.2. SESOP for nonlinear inverse problems 16
  - 1.2.1. The case of exact data 18
  - 1.2.2. The case of noisy data 19
  - 1.2.3. An algorithm with two search directions 20
- 1.3. Convergence and regularization properties 23
- 1.4. A first numerical example 31
  - 1.4.1. Discretization 32
  - 1.4.2. Reconstructions with Landweber and RESESOP 34
  - 1.4.3. A first outlook 39

2. Terahertz tomography 41
- 2.1. Propagation of electromagnetic waves 41
  - 2.1.1. Maxwell's equations 42
  - 2.1.2. The wave equation 43
  - 2.1.3. The Helmholtz equation 43
  - 2.1.4. Absorbing, isotropic media and the complex refractive index 44
  - 2.1.5. The superposition principle 44
  - 2.1.6. The inhomogeneous Helmholtz equation for the scattered field 45
- 2.2. Gaussian beams 45
- 2.3. Boundary values for the Helmholtz equation 48
- 2.4. An analysis of the inverse problem of THz tomography 49
  - 2.4.1. Existence and uniqueness 52
  - 2.4.2. The linearized scattering problem 60
  - 2.4.3. The adjoint linearized problem 65
  - 2.4.4. The observation operator in THz tomography 67
- 2.5. Terahertz tomography: direct and inverse problem 70
- 2.6. Numerical reconstructions with the Landweber method 73

3. SESOP in complex Hilbert spaces **81**
3.1. Sequential subspace optimization in complex Hilbert spaces 81
3.2. Reconstruction of the complex refractive index from simulated data 85

Conclusion and outlook **91**

A. Notation and formulas **95**
A.1. Notations 95
A.2. Optimization parameters 95

B. Some supplementary mathematical theory **97**
B.1. Functional analytic tools 97
B.2. Partial differential equations 98
B.2.1. Some theory for linear elliptic partial differential equations 98

Bibliography **101**

List of Tables

1.1. Some key data to evaluate the performance of the methods (A), (B) and (C) in the case of noisy data u_h^δ 35

1.2. Some key data to evaluate the performance of the methods (A), (B) and (C) in the case of exact data u_h 37

2.1. Parameters of the numerical Landweber experiment 78

2.2. Key data of the reconstruction with a nonlinear Landweber method, $f = 2.5 \cdot 10^{10}\,\mathrm{Hz}$ 79

3.1. Parameters of the numerical RESESOP experiment 85

3.2. Some key data to evaluate the performance of the RESESOP method (Algorithm 3.2) at the identification of m of the tested object using a Gaussian beam with a frequency $f = 0.1\,\mathrm{THz}$. 86

3.3. Some key data to evaluate the performance of the RESESOP method (Algorithm 3.2) in comparison with the Landweber method at the identification of m of the object from Chapter 2, using the microwave frequency $f = 2.5 \cdot 10^{10}\,\mathrm{Hz}$. 88

3.4. Some key data to evaluate the performance of the RESESOP method (Algorithm 3.2) at the identification of the complex refractive index of the tested object using a Gaussian beam with a microwave frequency $f = 2.5 \cdot 10^{10}\,\mathrm{Hz}$. 89

List of Figures

1.1. Metric projection of x onto a convex set C. 8

1.2. Illustration of the metric projection onto the intersection of two stripes in $\mathbb{R}^2$ 14

1.3. Surface plot of (a) exact function u_h and (b) exact parameter c_h on the grid Ω_h. . . 34

1.4. Reconstruction with the standard Landweber method (A), the Landweber type method (B) and the RESESOP method (C): surface plots of the respective reconstructed parameter c_{k_*} ((a), (c), (e)) and of the deviations from the exact solution c_h ((b), (d), (f)). 36

1.5. Plots of the respective residuals $\|R_k^\delta\|_h = \|F(c_k^\delta) - u^\delta\|_h$ versus the iteration index k for (a) the Landweber method, (b) the RESESOP method with a single search direction and (c) the RESESOP method with two search directions 37

1.6. Plots of the behavior of the respective norm of the residuals and the relative errors during the iterations 38

2.1. Real part of the electromagnetic field (z-component) of a Gaussian beam with frequency $f = 4 \cdot 10^{10}\,\mathrm{Hz}$, beam waist $W_0 = 0.013\,\mathrm{m}$ and a Rayleigh zone of length $2y_0 = 0.146\,\mathrm{m}$ in the x-y-plane (left) and as a three-dimensional plot (right). 47

2.2. Domain Ω with boundary $\partial\Omega$, containing the support of $1 - \tilde{n}^2$. 49

2.3. Real part of the electromagnetic field (z-component) of a Gaussian THz beam with frequency $f = 0.1\,\mathrm{THz}$, beam waist $W_0 = 0.013\,\mathrm{m}$ and a Rayleigh zone of length $2y_0 = 0.146\,\mathrm{m}$, refracted, reflected, and attenuated by a plastic cuboid with complex refractive index $\tilde{n} = 1.5 + i \cdot 0.005$ and quadratic cross-section of the size $4\,\mathrm{cm} \times 4\,\mathrm{cm}$. The THz emitter is situated in the first quadrant outside the domain. 50

2.4. Schematic representation of a THz tomograph 69

2.5. Schematic representation of relevant test objects; (a) objects with unknown outer boundaries, (b) objects with known outer boundaries and an unknown defect inside, (c) objects that consist of different materials 77

2.7. Reconstruction of real (a) and imaginary (b) part of m, obtained with the Landweber method, $f = 2.5 \cdot 10^{10}\,\mathrm{Hz}$ 80

3.2. Numerical reconstructions from the RESESOP experiment at frequency $f = 0.1\,\mathrm{THz}$ 87

3.3. Numerical reconstructions from the RESESOP experiment at frequency $f = 2.5 \cdot 10^{10}\,\mathrm{Hz}$ 89

Abstract

We introduce a sequential subspace optimization (SESOP) method for the iterative solution of nonlinear inverse problems in Hilbert spaces, based on the well-known methods for linear problems. The key idea is to use multiple search directions per iteration. Their length is determined by the nonlinearity and the local character of the forward operator. This choice admits a geometric interpretation after which the method is originally named: The current iterate is projected sequentially onto (intersections of) stripes, which emerge from affine hyperplanes whose respective normal vectors are given by the search directions and contain the solution set of the unperturbed inverse problem. We prove convergence and regularization properties and present a fast method using two search directions, which is evaluated by solving a simple nonlinear problem.

Furthermore, we extend our methods for complex Hilbert spaces and apply it to solve the inverse problem of terahertz tomography, a nonlinear parameter identification problem based on the Helmholtz equation, which consists in the nondestructive testing of dielectric media. The tested object is illuminated by an electromagnetic Gaussian beam and the goal is the reconstruction of the complex refractive index from measurements of the electric field. We conclude with some numerical reconstructions from synthetic data.

Zusammenfassung

In der vorliegenden Arbeit stellen wir eine Erweiterung der sequentiellen Unterraum-Optimierung (SESOP) zur Lösung nichtlinearer inverser Probleme in Hilberträumen vor, welche auf den bereits bekannten Verfahren für lineare Probleme basiert. Dabei handelt es sich um eine iterative Methode, bei der in jedem Schritt mehrere Suchrichtungen verwendet werden. Die Berechnung der Schrittweite berücksichtigt die Nichtlinearität des Vorwärtsoperators und lässt eine anschauliche geometrische Interpretation zu, welche dem Verfahren ursprünglich ihren Namen gab: Die aktuelle Iterierte wird sequentiell auf (den Schnitt von) Streifen projiziert. Diese Streifen gehen aus affinen Hyperebenen hervor und enthalten die Lösungsmenge des inversen Problems bei exakten Daten. Wir zeigen Konvergenz- und Regularisierungseigenschaften des Verfahrens. Insbesondere geben wir ein schnelles Verfahren mit zwei Suchrichtungen an und evaluieren die Methode anhand eines einfachen Beispiels.

Anschließend weiten wir die Methode auf komplexe Hilberträume aus und verwenden diese zur Lösung des inversen Problems der Terahertz-Tomographie. Dabei wird ein nichtleitendes, nichtmagnetisches Objekt mithilfe eines elektromagnetischen Gaußstrahls abgetastet. Das Ziel ist die Rekonstruktion des komplexen Brechungsindex aus Messungen des elektrischen Feldes. Dieses inverse Problem modellieren wir als Parameteridentifikationsproblem mithilfe der Helmholtzgleichung. Schließlich erzeugen wir für verschiedene Objekte synthetische Daten und rekonstruieren daraus den komplexen Brechungsindex.

Introduction

In the wide field of inverse problems, the class of nonlinear inverse problems has seen a great development in recent years. Nonlinear inverse problems are not only of theoretical interest, they arise naturally in science and technology and solutions to these problems constitute a major concern in many fields from engineering and physics to finance. Generally, an inverse problem refers to the determination of a source function x from information about the source's impact y. Mathematically, these problems are modeled by *operator equations* of the form

$$F(x) = y,$$

where $F : \mathcal{D}(F) \subset X \to Y$ is the *forward operator* that maps a function $x \in X$ to the respective data $y \in Y$. The space X is called the *source space* and Y the *data space.*
The *direct problem* consists in the calculation of the data $y \in Y$ from the knowledge of the function $x \in X$ and it usually corresponds to the (physical) model of the underlying process. Conversely, the *inverse problem* is the reconstruction of the source $x \in X$ from the given data $y \in Y$.

Depending on their mathematical nature, inverse problems are assigned to special classes of problems, of which we want to mention two important ones. First of all, we distinguish between linear and nonlinear inverse problems. Inverse problems are called *linear*, if the forward operator F is linear. In that case, we write

$$Fx = y$$

to emphasize this property. If F is nonlinear, the respective inverse problem is called *nonlinear.* This distinction is essential, as a solution of an inverse problem is strongly dependent on the (non-) linearity of the forward operator, which we will discuss in some more detail in this work.
Second, the properties of the underlying source and data spaces give rise to a further classification. The most prominent spaces in inverse problems are Hilbert and Banach spaces, of which a Hilbert space setting allows a greater variety of tools that are helpful for the recovery of a solution x.
In this work, the focus lies on nonlinear inverse problems in Hilbert spaces.

In applications, the data y are usually subject to *noise* of a certain *noise level* δ, such that it is necessary to develop solution techniques that take into account noisy data y^δ and still yield a useful solution, as a direct inversion of the above operator equation mostly leads to bad results. This effect is due to the *ill-posedness* of such mathematical problems and has been classified by Hadamard for linear forward operators [35]: The (linear) problem is *well-posed*, if the equation $Fx = y$ has a solution for each $y \in Y$, if this solution is unique and if the inverse operator F^{-1} is continuous, such that the solution x depends continuously on the data y. If one of these properties is not fulfilled, the problem is called *ill-posed.*
In the case of nonlinear forward operators, the ill-posedness is defined as a local property, see, e.g., [63]: The (nonlinear) operator equation $F(x) = y$ is *locally ill-posed* in $x^+ \in X$, if in each ball centered at x^+ there is a sequence x_k that does not converge to x^+, whereas the corresponding sequence of images $F(x_k)$ converges to $F(x^+)$.

In order to reconstruct an appropriate approximation x^+ to a solution x of an ill-posed operator

equation $F(x) = y$ from noisy data y^δ, it is essential to develop a suitable, stable *regularizing method*, i.e., an approximation of the inverse mapping by continuous operators, such that the reconstructed source depends continuously on the noise level δ. The choice of a regularization is closely related to the nature of the inverse problem we discussed above. A good understanding of the problem is thus fundamental for the solution.
Taking a closer look at the difference between linear and nonlinear problems and the corresponding definitions of ill-posedness, we see that the character of nonlinear problems has to be regarded locally, whereas it is possible to formulate and prove global statements for linear problems. Generally, information about a nonlinear operator F is given only in a neighborhood of some element $x \in X$, but not on the whole domain $\mathcal{D}(F)$. Regularization algorithms have to take this into account, for example by choosing the initial value in an iterative method close enough to the (estimated) solution, which can be realized by using a priori information.

There is a great range of (regularizing) methods that have been developed for the solution of linear inverse problems both in Hilbert and Banach spaces, see, e.g., [25, 52, 63]. Many of these have been adapted for an application in nonlinear inverse problems. An overview can be found in [43, 63].
Popular regularization methods are for example the Tikhonov regularization [26, 43, 58, 67] or the Landweber iteration, see [39, 42, 44]. The latter one is a standard method in nonlinear inverse problems, which is known to be extremely stable, but comparatively slow. It thus serves as a reasonable reference method for a comparison with the subspace methods we develop in this work.
Further regularization techniques are the method of approximate inverse [53], Newton-type methods such as the iteratively regularized Gauss-Newton method [44] or the inexact Newton method [42, 44, 62], and the conjugate gradient method [38]. In fact, most regularizing techniques for nonlinear problems are iterative methods, see also [22].

When dealing with practical applications, such as medical imaging or nondestructive testing, reconstruction methods are additionally required to be fast. For this reason, it is highly relevant to develop faster algorithms that speed up the solution of an inverse problem and enable an economic evaluation of the respective data.

The *sequential subspace optimization (SESOP)* and *regularizing sequential subspace optimization (RESESOP)* method for the solution of nonlinear inverse problems we present in this work is designed to reduce computation time. It is inspired by the subspace methods that have first been presented in [23, 56] for linear problems in finite-dimensional vector spaces and later generalized to linear inverse problems in Banach spaces [68, 69].
In the development as well as in the analysis of our method, we have to include the local character of the forward operator F. While the Landweber method is based on the method of steepest descent, i.e., the new iterate is sought in the search space that is spanned by the gradient of the *least squares functional*

$$\Psi(x) := \frac{1}{2} \left\| F(x) - y \right\|_Y^2 ,$$

the SESOP method can be regarded as an extension of this method towards larger search spaces. We will see that in both the linear and the nonlinear case the use of the gradient of the least squares functional as a search direction plays an important role, guaranteeing convergence and, in the case of noisy data, regularization.
The underlying idea of sequential subspace optimization is to project onto suitable hyperplanes or stripes, which contain the solution set of the original problem $F(x) = y$. This originates from the fact that in the linear case, the solution set itself is a hyperplane. When only noisy data are available, this is taken into account by regarding stripes instead of hyperplanes. The width of the

stripes is chosen in the order of the noise level δ. The sequential projection onto these stripes yields a regularizing method, which has been studied in [69] for linear problems in Banach spaces. When proceeding to nonlinear problems, we will basically apply two adaptions to the search spaces. First, as the solution space of a nonlinear problem is in general no longer a hyperplane, we move on to using stripes already in the unperturbed case, such that the nonlinearity of the forward operator, measured by the constant c_{tc} in the tangential cone condition

$$\left\|F(x) - F(\tilde{x}) - F'(x)(x - \tilde{x})\right\|_Y \leq c_{\mathrm{tc}} \left\|F(x) - F(\tilde{x})\right\|_Y, \quad 0 \leq c_{\mathrm{tc}} < 1,$$

determines the width of the stripes. Second, the stripes need to be defined in such a way that the local properties of the nonlinear operator F are respected. This is realized by relating the shape of the stripes to the current iterate and the properties of F in and around this iterate. This will be discussed in detail in Chapter 1. We will give a detailed discussion of the underlying ideas and finally prove convergence and regularization results for our proposed algorithms. The methods are evaluated by solving a well-known two-dimensional parameter identification problem and comparing their performance to a standard Landweber method.

Furthermore, we want to apply our method to a more complex inverse problem, which has seen a growing importance in research and industry in the last years: the inverse problem of *terahertz (THz) tomography*, which is a relatively new imaging technique that is, amongst others, applied in the nondestructive testing of plastics and ceramics [14, 30, 33, 73]. The tested object is illuminated by an electromagnetic beam in different positions. The main goal is to reconstruct the object's complex refractive index $\tilde{n}$ from measurements of the beam's electric field $\mathbf{E}$ around the tested object. In recent years, there has been great progress in the generation and detection of THz beams, such that THz radiation has become more and more attractive as a tool in nondestructive testing [79]. So far, the mathematical methods used in THz tomography are mainly inspired by existing imaging methods such as computed tomography or ultrasound tomography [28, 29, 61, 74, 77, 78]. The second part of this thesis deals with the mathematical modeling of the direct problem arising in THz tomography and the solution of the respective inverse problem.

Various further tomographic techniques allow the testing and imaging of objects with different physical properties for multiple purposes. The most prominent tomographic imaging technique is the *computed tomography* or X-ray tomography, where the density of the tested object is reconstructed from measurements of the intensity of the transmitted rays [57]. Due to the high frequency of X-rays, the resolution of the reconstructed image is very high, such that even small defects or structures can be detected. Consequently, this method is well established in medical imaging, for example in tumor diagnostics, despite the ionizing effect of X-radiation.
Another commonly used imaging technique is ultrasonic tomography [20]. In this case, ultrasonic radiation is used to gain information about the refractive index and inner boundaries of an object by measuring the reflected and refracted wave. The relatively long wavelength of the sound waves limits the resolution of this imaging technique. Yet, it is often applied in medical testing, as ultrasound does not affect the structure of human tissue.
Other examples are electrical impedance tomography [10, 15] or magnetic particle imaging [46].
Finally, THz tomography allows the use of different types of measured data (intensities, time-of-flight measurements) to reconstruct dielectric properties of non-magnetic materials. For the testing, THz radiation can be generated for example as a continuous wave or in the form of THz pulses.

The knowledge of the complex refractive index of an object allows several conclusions about the state of the object [30, 55, 79]. First of all, defects such as cracks, holes, or inclusions of air and other impurities can be identified, as their complex refractive index differs from the surrounding medium. For these purposes, it is usually sufficient to reconstruct only the refractive index, i.e., the real part of the complex refractive index, to obtain the relevant information. However, in the nondestructive testing of plastics and ceramics, we are confronted with the problem that it is hard to distinguish between the refractive indices of different plastics. The imaginary part, which is proportional to the respective absorption coefficient, thus yields information about an additional physical property of the materials in question. The absorption coefficient is hard to determine experimentally, such that a THz tomographic analysis is not only used to identify qualitative, but also quantitative material properties. Also, it is desirable to draw conclusions about the moisture content of an object, which affects in particular the absorption coefficient and, consequently, the imaginary part of the complex refractive index, see [55].

THz radiation is especially suited for the nondestructive testing of plastics and ceramics [30], as these materials are almost opaque for electromagnetic radiation in this frequency range, resulting in a high penetration depth. Consequently, THz tomography is not restricted to the testing of thin objects and is suited to obtain depth information. Due to the relatively long wavelength of THz radiation in comparison to X-radiation, the wave character of the electromagnetic THz radiation is more prominent and needs to be taken into account in the modeling. On the other hand, in contrast to microwave radiation or ultrasound, THz beams have a preferred direction of propagation and a finite beam width. The intensity peaks around the axis given by the direction of propagation. We are thus dealing with a beam geometry which combines certain characteristics of rays and spherical waves. We will discuss the geometry of THz beams in more detail in Section 2.2. This phenomenon clearly distinguishes the physical modeling of THz tomographic imaging from X-ray and ultrasound tomography as we are dealing with transmission and absorption (X-ray tomography) as well as refraction and reflection at boundaries (ultrasound imaging). For this reason, the application of reconstruction techniques that are suited for either X-ray or ultrasound tomography neglects one of these aspects, leaving some room for improvements, e.g., in the resolution.

The second part of this thesis complements the work of Tepe et al. [51, 71], who addressed the inverse problem of THz tomography within the project *Entwicklung und Evaluierung der Potenziale von Terahertz-Tomographie-Systemen* (IGF-457 ZN), a joint project together with the Plastics Center in Würzburg (SKZ) and financed by the AiF (Allianz Industrie und Forschung). An *adapted algebraic reconstruction technique (ART)* has been developed, which takes into account the laws of geometric optics and absorption losses. The forward problem is based on the Radon transform over refracted ray paths and can be interpreted as a model that is based on the ray character of THz beams. The results have been published in [71].
We now aim at an approach which mainly focuses on the wave character of THz radiation, such that the inverse problem in THz tomography that is derived in this work is to be related to the wide field of scattering problems (see for example [7, 19, 20, 47, 48, 75]). The radiation that has been used in the tomograph at the SKZ emits continuous wave THz radiation with a frequency range of 0.07-0.11 THz, such that we are dealing with frequencies at the limits of microwave and THz radiation. This supports a scattering theoretical approach.

Our underlying physical model is derived from Maxwell's equations, which represent the most general model for the mathematical description of the propagation of electromagnetic radiation in time and space. The specification of the respective physical conditions allows us to derive a simpler and yet sufficient model to describe a THz beam in vacuum as well as in the presence of objects with certain physical properties. In our setting, where we are dealing with plastic or ceramic objects that are neither magnetic nor conductive, the dielectric permittivity inside the area of interest can be regarded as almost everywhere constant, such that Maxwell's equations can be combined to obtain the wave equation. We use a continuous wave THz source emitting a time-harmonic electric field $\mathbf{E}$ with a fixed wave number k_0. Consequently, the wave equation simplifies to the Helmholtz equation

$$\Delta\mathbf{E}(\mathbf{x}) + k_0^2\tilde{n}^2(\mathbf{x})\mathbf{E}(\mathbf{x}) = 0,$$

where the complex refractive index $\tilde{n}$ appears as a parameter in this partial differential equation. Together with the superposition principle and the analytically given incident field, which is described as a Gaussian beam, we obtain an inhomogeneous Helmholtz equation as the basis for the direct problem of THz tomography. This demonstrates a major benefit of the model presented in this thesis: The rather complex geometry of the beam is fully taken into account in the calculation of the resulting total field. These physical basics are to be found in Chapter 2, along with a detailed analysis of the full problem and the definition of the observation operator to describe the measuring process. For simplicity we will work with a linear observation operator and restrict ourselves to synthetic data.

The direct problem in THz tomography is thus modeled by a composition of a nonlinear parameter-to-solution operator, mapping the complex refractive index $\tilde{n}$ to the corresponding solution of a boundary value problem based on the Helmholtz equation combined with the superposition principle, and a linear observation operator. The nonlinearity of the forward operator suggests an iterative solution of the corresponding inverse problem, consisting in the reconstruction of the parameter $\tilde{n}$ from measurements of the total electric field. By means of the nonlinear Landweber method, we solve the inverse problem of THz tomography, given synthetic (noisy) data. However, at this point the numerical disadvantage of our model becomes obvious: Each step of the Landweber iteration requires two computationally expensive evaluations of boundary value problems, the direct problem and the adjoint problem. The latter turns out to be again a boundary value problem based on the Helmholtz equation. An application of a faster reconstruction method, such as the sequential subspace optimization, is thus highly desirable.

The inverse problem we are dealing with in THz tomography is a nonlinear inverse problem in complex Hilbert spaces. However, the SESOP methods we introduce in Chapter 1 are designed for applications in real Hilbert spaces and need some further adaption for an application in complex Hilbert spaces. We discuss the necessary adaptions in Chapter 3 and present an algorithm with two search directions that meets these requirements.
In Chapter 2, we solve the inverse problem of THz tomography numerically with the nonlinear Landweber method. We use a low wave number k_0 in the microwave spectrum to illuminate an object with two different inclusions and generate synthetic noisy data for the reconstruction.
Further numerical examples are presented in Chapter 3. For an object with two smaller inclusions than in the previous test we generate noisy synthetic data, first for the frequency 0.1 THz and subsequently again for the microwave frequency we used in the Landweber experiment. For the reconstructions, we use the adapted RESESOP algorithm with two search directions to iteratively solve the respective inverse problem. We compare the results and give some interpretations of our methods.

The thesis is concluded by giving a short overview and discussion of the results and an outlook to future research.

An explanation of the notation and some useful statements from functional analysis are to be found in the appendix.

1. Sequential subspace optimization

There are many ways to find a stable solution of an inverse problem when noisy data are given. Depending on the nature of the problem, a method can be more or less suited for the solution of a specific problem when it comes to the time that is needed for a reconstruction. Based on the sequential subspace optimization (SESOP) methods that are discussed in [56] and [68, 69] we want to present a similar method for nonlinear inverse problems in real Hilbert spaces.
To begin with, we summarize the SESOP methods for linear inverse problems, based on the results presented in [56, 68, 69]. The theoretical findings of this chapter, dealing with the nonlinear case, have been published in [72]:

> A. Wald, T. Schuster. Sequential subspace optimization for nonlinear inverse problems.
> *Journal of Inverse and Ill-posed Problems.* 25(1), pp. 99-117, 2016.
> DOI:10.1515/jiip-2016-0014.

In order to keep the notation as simple as possible, we abstain from denoting the occurring norms and inner products according to their respective domains in this chapter. As usual, norms are denoted by $\|\cdot\|$ and inner products by $\langle \cdot, \cdot \rangle$.

1.1. SESOP for linear inverse problems

Let X,Y be real Hilbert spaces and $A : X \to Y$ a continuous linear operator. The operator $A^* : X^* \to Y^*$ is the adjoint of A. As X and Y are Hilbert spaces, we have $X \cong X^*$ and $Y \cong Y^*$, and we thus identify X and Y with their respective dual spaces.
We consider the operator equation

$$Ax = y \tag{1.1}$$

with the solution set

$$M_{Ax=y} := \{x \in X : Ax = y\}. \tag{1.2}$$

The range of A is defined as

$$\mathcal{R}(A) := \{Ax \,:\, x \in X\} \subseteq Y.$$

If only noisy data y^δ are available, we assume that

$$\left\| y - y^\delta \right\| \leq \delta,$$

where the noise level is denoted by $\delta > 0$.
We want to utilize an iteration of the form

$$x_{n+1} := x_n - \sum_{i \in I_n} t_{n,i} A^* w_{n,i} \tag{1.3}$$

to calculate a solution $x \in X$, where I_n is a finite index set and $w_{n,i} \in Y$ for all $i \in I_n$. The index $n \in \mathbb{N} = \{0, 1, 2, ...\}$ is called *iteration index*. The parameters $t_n := (t_{n,i})_{i \in I_n} \in \mathbb{R}^{|I_n|}$ minimize the function

$$h_n(t) := \frac{1}{2}\left\|x_n - \sum_{i\in I_n} t_i A^* w_{n,i}\right\|^2 + \sum_{i\in I_n} t_i \langle w_{n,i}, y\rangle . \tag{1.4}$$

In [68] it was shown that the minimization of $h_n(t)$ is equivalent to computing the metric projection

$$x_{n+1} = P_{\bigcap_{i\in I_n} H_{n,i}}(x_n)$$

onto the intersection of hyperplanes

$$H_{n,i} := \{x \in X \ : \ \langle A^* w_{n,i}, x\rangle - \langle w_{n,i}, y\rangle = 0\} .$$

Note, that $M_{Ax=y} \subseteq H_{n,i}$ for all $i \in I_n$. This property later motivates the approach for a regularizing sequential subspace optimization method, where we replace the hyperplanes by stripes whose widths are of the order of the noise level δ and which still contain the solution set $M_{Ax=y}$.

At this point, we give a short overview of some basic tools that are needed throughout this chapter.

Definition 1.1. *The metric projection of $x \in X$ onto a nonempty closed convex set $C \subseteq X$ is the unique element $P_C(x) \in C$ such that*

$$\|x - P_C(x)\|^2 = \min_{z\in C} \|x - z\|^2 .$$

(For later convenience, we use the square of the distance.)

The metric projection $P_C(x)$ onto a convex set C satisfies a descent property, which reads

$$\|z - P_C(x)\|^2 \leq \|z - x\|^2 - \|P_C(x) - x\|^2 \tag{1.5}$$

for all $z \in C$. In the special case that C is an (affine) hyperplane of X, the metric projection onto C corresponds to the orthogonal projection and (1.5) becomes an equality, namely an instance of the classical Pythagorean theorem.

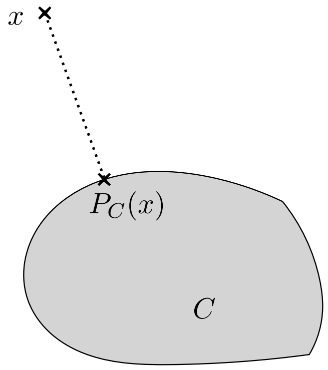

Figure 1.1.: Metric projection of x onto a convex set C.

Definition 1.2. *For $u \in X \setminus \{0\}$ and $\alpha, \xi \in \mathbb{R}$ with $\xi \geq 0$ we define the* hyperplane

$$H(u,\alpha) := \{x \in X \ : \ \langle u, x\rangle = \alpha\} ,$$

the halfspace

$$H_{\leq}(u,\alpha) := \{x \in X \ : \ \langle u, x\rangle \leq \alpha\}$$

and analogously $H_{\geq}(u,\alpha)$, $H_{<}(u,\alpha)$ and $H_{>}(u,\alpha)$. Finally, we define the stripe

$$H(u,\alpha,\xi) := \{x \in X \ : \ |\langle u, x\rangle - \alpha| \leq \xi\} .$$

Obviously we can write $H(u,\alpha,\xi) = H_{\leq}(u,\alpha+\xi) \cap H_{\geq}(u,\alpha-\xi)$ and $H(u,\alpha,0) = H(u,\alpha)$, i.e., the stripe corresponding to u and α with width given by ξ contains the hyperplane $H(u,\alpha)$.

Remark 1.3. *The sets defined in Definition 1.2 are convex, and due to* $u \neq 0$ *they are nonempty. In addition, the hyperplane* $H(u,\alpha)$*, the halfspaces* $H_{\leq}(u,\alpha)$ *and* $H_{\geq}(u,\alpha)$*, and the stripe* $H(u,\alpha,\xi)$ *are closed.*

Definition 1.4. *Let* $H(u,\alpha,\xi) \subseteq X$ *be a stripe in the Hilbert space* X*. We call* $H(u,\alpha+\xi)$ *the* upper bounding hyperplane *and* $H(u,\alpha-\xi)$ *the* lower bounding hyperplane *of the stripe* $H(u,\alpha,\xi)$*.*

In the Hilbert space setting, the metric projection $P_{H(u,\alpha)}(x)$ of $x \in X$ onto a hyperplane $H(u,\alpha)$ corresponds to an orthogonal projection and we have

$$P_{H(u,\alpha)}(x) = x - \frac{\langle u,x\rangle - \alpha}{\|u\|^2} u. \tag{1.6}$$

The element u of X can be normalized, such that ${}^{u}/_{\|u\|}$ is the normal vector of the bounding hyperplanes $H(u,\alpha \pm \xi)$ of the stripe $H(u,\alpha,\xi)$, the parameter ${}^{\alpha}/_{\|u\|}$ is the offset and ${}^{2\xi}/_{\|u\|}$ is the width of the stripe. The normalization may be useful in numerical calculations, if $\|u\|$ is very small.

The following statement yields some helpful tools for the analysis of the sequential subspace methods that are discussed in this work. According to Definition 1.1, the metric (or orthogonal) projection onto a convex set (particularly onto hyperplanes) can be treated as a minimization problem, such that it is reasonable to make use of the tools provided by optimization theory, see, e.g., [59].

Proposition 1.5. *The proof of the following statements is given in [70] for (convex and uniformly smooth) Banach spaces and can be easily translated to the situation in Hilbert spaces.*

(i) Let $H(u_i,\alpha_i)$*,* $i = 1,...,N$*, be hyperplanes with nonempty intersection*

$$H := \bigcap_{i=1}^{N} H(u_i,\alpha_i).$$

The projection of x *onto* H *is given by*

$$P_H(x) = x - \sum_{i=1}^{N} \tilde{t}_i u_i, \tag{1.7}$$

where $\tilde{t} = (\tilde{t}_1,...,\tilde{t}_N) \in \mathbb{R}^N$ *minimizes the convex function*

$$h(t) = \frac{1}{2}\left\| x - \sum_{i=1}^{N} t_i u_i \right\|^2 + \sum_{i=1}^{N} t_i \alpha_i, \; t = (t_1,...,t_N) \in \mathbb{R}^N, \tag{1.8}$$

with partial derivatives

$$\frac{\partial}{\partial t_j} h(t) = -\left\langle u_j, x - \sum_{i=1}^{N} t_i u_i \right\rangle + \alpha_j. \tag{1.9}$$

If the vectors u_i*,* $i = 1,...,N$*, are linearly independent,* h *is strictly convex and* $\tilde{t}$ *is unique.*

(ii) *Let* $H_i := H_{\leq}(u_i, \alpha_i)$, $i = 1, 2$, *be two halfspaces with linearly independent vectors* u_1 *and* u_2. *Then* $\tilde{x}$ *is the projection of* x *onto* $H_1 \cap H_2$ *if and only if it satisfies the Karush-Kuhn-Tucker conditions for* $\min_{z \in H_1 \cap H_2} \|z - x\|^2$, *which read*

$$\begin{aligned} \tilde{x} &= x - t_1 u_1 - t_2 u_2, && \text{for some } t_1, t_2 \geq 0, \\ \alpha_i &\geq \langle u_i, \tilde{x} \rangle, && i = 1, 2, \\ 0 &\geq t_i \left(\alpha_i - \langle u_i, \tilde{x} \rangle \right), && i = 1, 2. \end{aligned} \tag{1.10}$$

(iii) *For* $x \in H_{>}(u, \alpha)$ *the projection of* x *onto* $H_{\leq}(u, \alpha)$ *is given by*

$$P_{H_{\leq}(u,\alpha)}(x) = P_{H(u,\alpha)}(x) = x - t_+ u, \tag{1.11}$$

where

$$t_+ = \frac{\langle u, x \rangle - \alpha}{\|u\|^2} > 0. \tag{1.12}$$

(iv) *The projection of* $x \in X$ *onto a stripe* $H(u, \alpha, \xi)$ *is given by*

$$P_{H(u,\alpha,\xi)}(x) = \begin{cases} P_{H_{\leq}(u,\alpha+\xi)}(x), & \text{if } x \in H_{>}(u, \alpha + \xi), \\ x, & \text{if } x \in H(u, \alpha, \xi), \\ P_{H_{\geq}(u,\alpha-\xi)}(x), & \text{if } x \in H_{<}(u, \alpha - \xi). \end{cases} \tag{1.13}$$

Our goal is to use search directions of the form $A^* w_{n,i}$ in each iteration $n \in \mathbb{N}$ for some finite index set I_n. We set $u_{n,i} := A^* w_{n,i}$ and choose the offset $\alpha_{n,i}$ such that the solution set $M_{Ax=y}$ is contained in each hyperplane $H_{n,i} := H(u_{n,i}, \alpha_{n,i})$. The following algorithm provides a method to compute the metric projection

$$P_{M_{Ax=y}}(x_0)$$

of $x_0 \in X$ onto the solution set $M_{Ax=y}$ in the case of exact data $y \in \mathcal{R}(A)$.

Algorithm 1.6. *Choose an initial value* $x_0 \in X$. *At iteration* $n \in \mathbb{N}$, *choose a finite index set* I_n *and search directions* $A^* w_{n,i}$ *with* $w_{n,i} \in Y$ *and* $i \in I_n$. *Compute the new iterate as*

$$x_{n+1} := P_{H_n}(x_n), \tag{1.14}$$

where

$$H_n := \bigcap_{i \in I_n} H(A^* w_{n,i}, \langle w_{n,i}, y \rangle). \tag{1.15}$$

We have $M_{Ax=y} \subseteq H_n$ as each $z \in M_{Ax=y}$ fulfills

$$\langle A^* w_{n,i}, z \rangle = \langle w_{n,i}, Az \rangle = \langle w_{n,i}, y \rangle$$

for all $i \in I_n$ and $n \in \mathbb{N}$. Due to $x_{n+1} \in H_n$ we thus have

$$\langle w_{n,i}, Ax_{n+1} - y \rangle = \langle A^* w_{n,i}, x_{n+1} - z \rangle = 0 \tag{1.16}$$

for all $z \in M_{Ax=y}$ and for all $i \in I_n$. We define the *search space*

$$U_n := \operatorname{span} \{ u_{n,i} := A^* w_{n,i} \ : \ i \in I_n \}$$

as the linear span of the search directions $u_{n,i}$ used in iteration n.
Note that (1.16) yields $(x_{n+1} - z) \perp U_n$.

As stated in Proposition 1.5, the iterate x_{n+1} can be computed by a minimization of the convex function h. The search directions $A^* w_{n,i}$ spanning the subspace in which a minimizing solution is sought are fixed, so the minimization itself does not require any costly applications of A or its adjoint A^*. The additional cost caused by higher dimensional search spaces is comparatively minor.

For the weak convergence of the sequence of iterates, the current gradient $A^*(Ax_n - y)$ of the functional $\frac{1}{2}\|Ax - y\|^2$ evaluated at x_n needs to be included in the search space to guarantee an estimate of the form

$$\|z - x_{n+1}\|^2 \leq \|z - x_n\|^2 - \frac{\|R_n\|^2}{\|A\|^2} \tag{1.17}$$

for all $z \in M_{Ax=y}$, where $R_n := Ax_n - y$ is the current residual. This is verified by setting, for example, $w_{n,n} := R_n$, $u_{n,n} = A^* w_{n,n}$, and using (1.5), as well as the estimate

$$\|u_{n,n}\| = \|A^* R_n\| \leq \|A\| \cdot \|R_n\| \,.$$

A more detailed analysis of convergence results can be found again in [70].

1.1.1. Regularizing sequential subspace optimization

If only noisy data $y^\delta \in Y$ are given, we modify Algorithm 1.6 to turn it into a regularizing method. We define the two canonical sets of search directions

$$G_n^\delta := \Big\{ A^*(Ax_k^\delta - y^\delta) \;:\; 0 \leq k \leq n \Big\} \tag{1.18}$$

and

$$D_n^\delta := \Big\{ x_k^\delta - x_l^\delta \;: 0 \leq l < k \leq n \Big\} \,. \tag{1.19}$$

The set G_n^δ contains the gradients of the least squares functional evaluated at the iterates x_k^δ, whereas D_n^δ contains the directions given by the differences between two iterates.

The following algorithm takes into account the noise level δ. The underlying idea is to proceed to projections onto stripes instead of hyperplanes, such that the stripes have a finite width of the order of the noise level and the solution set $M_{Ax=y}$ is still contained in the stripes.

Algorithm 1.7. *Choose an initial value $x_0^\delta := x_0$ and fix some constant $\tau > 1$. At iteration $n \in \mathbb{N}$, choose a finite index set I_n^δ and search directions $A^* w_{n,i}^\delta \in G_n^\delta \cup D_n^\delta$ as defined above.*
If the residual R_n^δ satisfies the discrepancy principle

$$\|R_n^\delta\| \leq \tau\delta, \tag{1.20}$$

stop iterating. Otherwise, compute the new iterate as

$$x_{n+1}^\delta := x_n^\delta - \sum_{i \in I_n^\delta} t_{n,i}^\delta A^* w_{n,i}^\delta, \tag{1.21}$$

choosing $t_n^\delta = (t_{n,i}^\delta)_{i \in I_n^\delta}$ such that

$$x_{n+1}^\delta \in H_n^\delta := \bigcap_{i \in I_n^\delta} H\big(A^* w_{n,i}^\delta, \langle w_{n,i}^\delta, y^\delta \rangle, \delta \|w_{n,i}^\delta\|\big) \tag{1.22}$$

and such that an inequality of the form

$$\|z - x_{n+1}^\delta\|^2 \leq \|z - x_n^\delta\|^2 - C\|R_n^\delta\|^2 \tag{1.23}$$

is valid for all $z \in M_{Ax=y}$ and for some constant $C > 0$.

The choice $A^* w_{n,i}^\delta \in G_n^\delta \cup D_n^\delta$ together with the linearity of the operator A can be exploited to obtain a recursion for the computation of the search directions. This is discussed in detail in [69, 70]. An adaption to the case of nonlinear operators is not possible, therefore we content ourselves with the reference at this point.
However, we note that $M_{Ax=y} \subseteq H_n^\delta$, because for $z \in M_{Ax=y}$ we have

$$\left|\langle A^* w_{n,i}^\delta, z\rangle - \langle w_{n,i}^\delta, y^\delta\rangle\right| = \left|\langle w_{n,i}^\delta, y - y^\delta\rangle\right| \leq \delta\|w_{n,i}^\delta\|.$$

Due to (1.23), the sequence $\left\{\|z - x_n^\delta\|\right\}_{n\in\mathbb{N}}$ decreases for a fixed noise level δ. It is proved in [68, 69] that the discrepancy principle yields a finite stopping index $n_* = n_*(\delta) := \min\{n \in \mathbb{N} : \|R_n^\delta\| \leq \tau\delta\}$.

It is possible to prove convergence results and other interesting statements for certain choices of search directions for the RESESOP method in the linear case. Once again, we recommend to consult [68, 69, 70] for further details. We want to emphasize though that gradients as search directions are of special interest already in the case of linear inverse problems. We will see that they are also a good choice in the nonlinear case. Before looking at a suitable method for nonlinear inverse problems, we consider an important special case of Algorithm 1.7.

1.1.2. RESESOP with two search directions

We want to summarize a fast way to compute x_{n+1}^δ according to Algorithm 1.7, using only two search directions, such that (1.22) and (1.23) are valid. This algorithm has been suggested and analyzed by Schöpfer and Schuster in [69] and has been successfully implemented for the numerical solution of an integral equation of the first kind. It is based on the fact that the projection of $x \in X$ onto the intersection of two halfspaces can be computed by at most two projections, if x is already contained in one of them.
As a stopping rule we choose the discrepancy principle. We state that this choice has the important advantage that, as long as the discrepancy principle is not fulfilled, we are in the above described situation: The current iterate is contained in one stripe, but not in the other one, therefore a stepwise projection of the current iterate onto the intersection of the respective stripes is possible, see also Remark 1.9. The following proposition provides the basic results for Algorithms 1.10 and 1.21.

Proposition 1.8. *Let $H_j := H_{\leq}(u_j, \alpha_j)$, $j = 1, 2$, be two halfspaces with $H_1 \cap H_2 \neq \emptyset$. Let $x \in H_>(u_1, \alpha_1) \cap H_2$. The metric projection of x onto $H_1 \cap H_2$ can be computed by at most two metric projections onto (the intersection of) the bounding hyperplanes by the following steps.*

(i) Compute

$$x_1 := P_{H(u_1,\alpha_1)}(x) = x - \frac{\langle u_1, x\rangle - \alpha_1}{\|u_1\|^2} u_1.$$

Then, for all $z \in H_1$, we have

$$\|z - x_1\|^2 \leq \|z - x\|^2 - \left(\frac{\langle u_1, x\rangle - \alpha_1}{\|u_1\|}\right)^2. \tag{1.24}$$

If $x_1 \in H_2$, we are done. Otherwise, go to step (ii).

(ii) Compute

$$x_2 := P_{H_1 \cap H_2}(x_1).$$

Then $x_2 = P_{H_1 \cap H_2}(x)$ *and for all* $z \in H_1 \cap H_2$ *we have*

$$\|z - x_2\|^2 \leq \|z - x\|^2 - \left(\left(\frac{\langle u_1, x \rangle - \alpha_1}{\|u_1\|} \right)^2 + \left(\frac{\langle u_2, x_1 \rangle - \alpha_2}{\gamma \|u_2\|} \right)^2 \right), \tag{1.25}$$

where

$$\gamma := \left(1 - \left(\frac{|\langle u_1, u_2 \rangle|}{\|u_1\| \cdot \|u_2\|} \right)^2 \right)^{\frac{1}{2}} \in (0, 1]. \tag{1.26}$$

Note that if $\langle u_1, u_2 \rangle = \|u_1\| \cdot \|u_2\|$ is valid, step (i) of Proposition 1.8 already yields the metric projection of x onto $H_1 \cap H_2$. Consequently, we have $\gamma \in (0, 1]$. This is quite intuitive when considering these two cases in the illustration in Figure 1.2.

Proof. In our Hilbert space setting, equation (1.24) requires no further proof as it follows directly from estimate (1.5) due to the convexity of H_1. To obtain the descent property (1.25) in step (ii), the statements from Proposition 1.5 are used. Consider the function h, which is associated with the metric projection onto hyperplanes and let $\tilde{t} = (\tilde{t}_1, \tilde{t}_2) \in \mathbb{R}^2$ minimize h. From ${}^{\partial}\!/_{\partial t_j} h(\tilde{t}) = 0$ for $j = 1, 2$ we obtain the system of linear equations

$$\begin{aligned} 0 &= -\left\langle u_1, x_1 - \tilde{t}_1 u_1 - \tilde{t}_2 u_2 \right\rangle + \alpha_1, \\ 0 &= -\left\langle u_2, x_1 - \tilde{t}_1 u_1 - \tilde{t}_2 u_2 \right\rangle + \alpha_2. \end{aligned}$$

According to the first step we have $\langle u_1, x_1 \rangle = \alpha_1$. This yields after some elementary calculations

$$\tilde{t}_1 = \left(\frac{\langle u_1, u_2 \rangle}{\langle u_1, u_2 \rangle^2 - (\|u_1\| \cdot \|u_2\|)^2} \right) \cdot \Big(\langle u_2, x_1 \rangle - \alpha_2 \Big)$$

and

$$\tilde{t}_2 = -\|u_1\|^2 \Big(\langle u_1, u_2 \rangle^2 - (\|u_1\| \cdot \|u_2\|)^2 \Big)^{-1} \cdot \Big(\langle u_2, x_1 \rangle - \alpha_2 \Big).$$

Now we easily obtain the descent property (1.25) by using $\|z - x_2\|^2 \leq \|z - x_1\|^2 - \left\| \tilde{t}_1 u_1 + \tilde{t}_2 u_2 \right\|^2$ (see (1.5)) together with (1.24), and the above expressions for t_1 and t_2. Proposition 1.5 finally yields

$$x_2 = x_1 - \tilde{t}_1 u_1 - \tilde{t}_2 u_2 = P_{H_1 \cap H_2}(x).$$

□

In general, this stepwise projection does not yield the correct metric projection, if the projected point is not included in either of the halfspaces. We have illustrated this for the two-dimensional case in Figure 1.2 for two stripes: The point x_1 is not contained in any of the stripes and the stepwise metric projections, depending on the order of projections, yield the results $y_1^{(1,2)}$, $y_1^{(2,1)}$ that differ from the correct metric projection y_1 of x_1 onto $H_1 \cap H_2$. On the other hand, the successive projection of the point x_2 onto $H_1 \cap H_2$ coincides with the correct metric projection y_2. Note that Proposition 1.8 can easily be applied in the situation of our example in Figure 1.2 just by defining suitable halfspaces, see also Proposition 1.5.

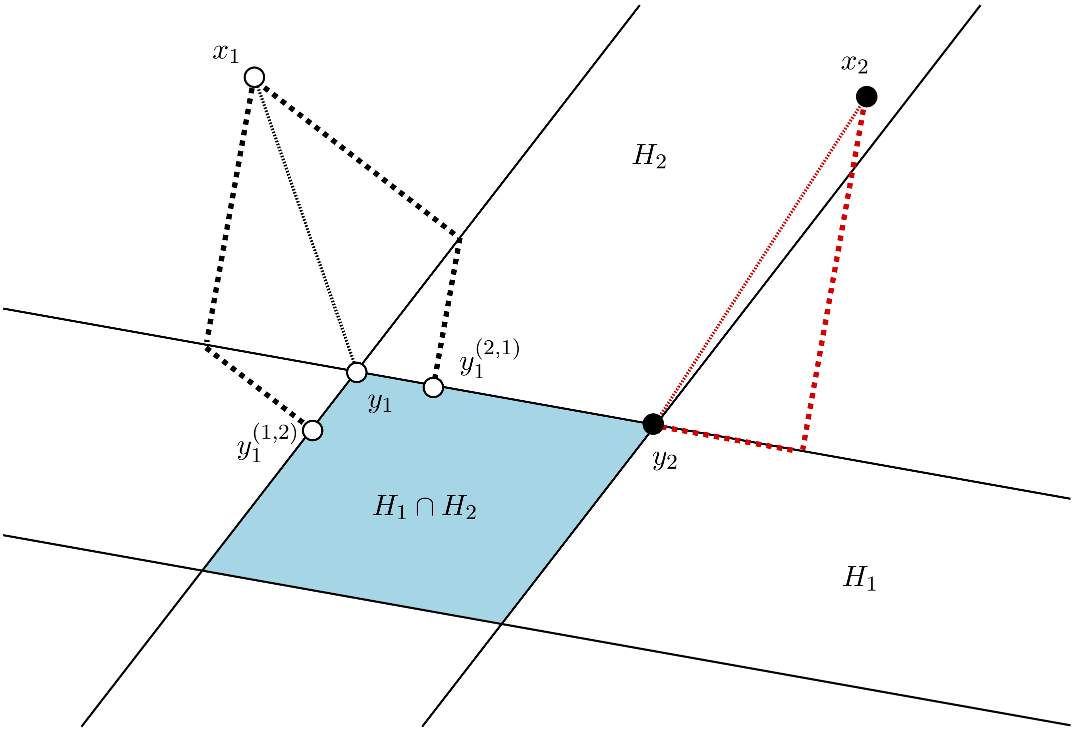

Figure 1.2.: Example for $X = \mathbb{R}^2$: Metric projections $y_1 = P_{H_1 \cap H_2}(x_1)$ and $y_2 = P_{H_1 \cap H_2}(x_2)$ onto the intersection of the two stripes H_1 and H_2, the points $y_1^{(1,2)}$, $y_1^{(2,1)}$ and y_2 are the results of stepwise metric projections as described in Proposition 1.8. Note that $y_1^{(1,2)} \neq y_1 \neq y_1^{(2,1)}$.

Remark 1.9. *The previous statement is essential for our methods and for the choice of the stopping criterion. When projecting an element $x \in X$ onto the intersection of two halfspaces (or stripes) H_1 and H_2 by first calculating $x_1 = P_{H_1}(x)$ and afterwards $x_2 = P_{H_1 \cap H_2}(x_1)$, we might have $x_2 \neq P_{H_1 \cap H_2}(x)$. This can occur if x is contained neither in H_1 nor in H_2. If x is already contained in H_1 or H_2, we have equality. This has been illustrated in [69] and in Figure 1.2 for Hilbert spaces. The reason is that the order of projection plays an important role. If we have for example $x \in H_1$, the order of projections is evident and yields the desired result. This observation is reflected in the stepwise procedure in Algorithms 1.10 and 1.21.*

In the following algorithm, Morozov's discrepancy principle and the choices $I_n = \{n-1, n\}$ and $w_i^\delta := w_{n,i}^\delta := Ax_i^\delta - y^\delta$ for $i \in I_n$ assure that the projections in each step can be calculated uniquely according to Proposition 1.8, which yields a fast regularizing method to compute a solution of (1.1) using noisy data.

Algorithm 1.10. *Fix an initial value $x_0^\delta := x_0 \in X$ and a constant $\tau > 1$ for the discrepancy principle. In Algorithm 1.7, choose the search direction u_0^δ for the first iteration ($n = 0$) and, for all iterations $n \geq 1$, choose the search directions $\{u_n^\delta, u_{n-1}^\delta\}$, where*

$$u_n^\delta := A^* w_n^\delta, \quad w_n^\delta := Ax_n^\delta - y^\delta.$$

Define $H_{-1}^\delta := X$ and, for $n \in \mathbb{N}$, the stripes

$$H_n^\delta := H\big(u_n^\delta, \alpha_n^\delta, \delta \|R_n^\delta\|\big)$$

with

$$\alpha_n^\delta := \langle u_n^\delta, x_n^\delta \rangle - \|R_n^\delta\|^2.$$

As long as $\|R_n^\delta\| > \tau\delta$, *we have*

$$x_n^\delta \in H_>\big(u_n^\delta, \alpha_n^\delta + \delta\|R_n^\delta\|\big) \cap H_{n-1}^\delta, \tag{1.27}$$

and thus calculate the new iterate x_{n+1}^δ *according to the following two steps.*

(i) *Compute*

$$\tilde{x}_{n+1}^\delta := P_{H(u_n^\delta, \alpha_n^\delta + \delta\|R_n^\delta\|)}(x_n^\delta)$$

by

$$\tilde{x}_{n+1}^\delta = x_n^\delta - \frac{\langle u_n^\delta, x_n^\delta\rangle - \big(\alpha_n^\delta + \delta\|R_n^\delta\|\big)}{\|u_n^\delta\|^2} u_n^\delta = x_n^\delta - \frac{\|R_n^\delta\|\,\big(\|R_n^\delta\| - \delta\big)}{\|u_n^\delta\|^2} u_n^\delta.$$

Then, for all $z \in M_{Ax=y}$ *we have*

$$\left\|z - \tilde{x}_{n+1}^\delta\right\|^2 \leq \left\|z - x_n^\delta\right\|^2 - \left(\frac{\|R_n^\delta\|(\|R_n^\delta\| - \delta)}{\|u_n^\delta\|}\right)^2.$$

If $\tilde{x}_{n+1}^\delta \in H_{n-1}^\delta$, *we have* $\tilde{x}_{n+1}^\delta = P_{H_n^\delta \cap H_{n-1}^\delta}(x_n^\delta)$. *In that case, we define* $x_{n+1}^\delta := \tilde{x}_{n+1}^\delta$ *and are done. Otherwise, go to step (ii).*

(ii) *Depending on* $\tilde{x}_{n+1}^\delta \in H_\gtrless(u_{n-1}^\delta, \alpha_{n-1}^\delta \pm \delta\|R_{n-1}^\delta\|)$, *compute*

$$x_{n+1}^\delta := P_{H(u_n^\delta, \alpha_n^\delta + \delta\|R_n^\delta\|) \cap H(u_{n-1}^\delta, \alpha_{n-1}^\delta \pm \delta\|R_{n-1}^\delta\|)}(\tilde{x}_{n+1}^\delta),$$

i.e.,

$$x_{n+1}^\delta = \tilde{x}_{n+1}^\delta - t_{n,n}^\delta u_n^\delta - t_{n,n-1}^\delta u_{n-1}^\delta,$$

such that $(t_{n,n}^\delta, t_{n,n-1}^\delta)$ *minimizes*

$$h_2(t_1, t_2) := \frac{1}{2}\left\|x_n^\delta - t_1 u_n^\delta - t_2 u_{n-1}^\delta\right\|^2 + t_1(\alpha_n^\delta + \delta\|R_n^\delta\|) + t_2(\alpha_{n-1}^\delta \pm \delta\|R_{n-1}^\delta\|).$$

Then we have $x_{n+1}^\delta = P_{H_n^\delta \cap H_{n-1}^\delta}(x_n^\delta)$ *and for all* $z \in M_{Ax=y}$ *we have*

$$\|z - x_{n+1}^\delta\|^2 \leq \|z - x_n^\delta\|^2 - S_n^\delta$$

with

$$S_n^\delta := \left(\frac{\|R_n^\delta\|(\|R_n^\delta\| - \delta)}{\|u_n^\delta\|}\right)^2 + \left(\frac{\big|\langle u_{n-1}^\delta, \tilde{x}_{n+1}^\delta\rangle - (\alpha_{n-1}^\delta \pm \delta\|R_{n-1}^\delta\|)\big|}{\gamma_n\|u_{n-1}^\delta\|}\right)^2$$

and

$$\gamma_n := \left(1 - \left(\frac{\big|\langle u_n^\delta, u_{n-1}^\delta\rangle\big|}{\|u_n^\delta\|\|u_{n-1}^\delta\|}\right)^2\right)^{\frac{1}{2}} \in (0, 1].$$

Remark 1.11. (a) *It is easy to see that* (1.27) *holds as long as* $\|R_n^\delta\| > \tau\delta$. *Indeed, the definition of* α_n^δ *yields*

$$\langle u_n^\delta, x_n^\delta\rangle = \alpha_n^\delta + \|R_n^\delta\|^2 > \alpha_n^\delta + \delta\|R_n^\delta\|,$$

which represents precisely the condition for x_n^δ *to be an element of* $H_>\big(u_n^\delta, \alpha_n^\delta + \delta\|R_n^\delta\|\big)$. *We have* $x_n^\delta \in H_{n-1}^\delta$ *due to the previous iteration.*

(b) *The advantage of this algorithm is that using the current gradient as a search direction assures that the descent property* (1.23) *holds, yielding convergence, while the use of the gradient from the previous step speeds up the descent additionally: the larger the second summand in* S_n^δ, *the greater the descent, see also Remark 1.22 (d).*

(c) *Proposition 1.8 yields explicit expressions for an implementation.*

1.2. SESOP for nonlinear inverse problems

We now want to develop a method for nonlinear inverse problems based on the one we introduced in the previous section. To this end, we consider the operator equation

$$F(x) = y, \tag{1.28}$$

where $F : \mathcal{D}(F) \subseteq X \to Y$ is a nonlinear operator between Hilbert spaces X and Y and $\mathcal{D}(F)$ is its domain. Our aim is to translate the idea of sequential projections onto stripes to the context of nonlinear operators. For that purpose, we have to make sure that the solution set

$$M_{F(x)=y} := \{x \in X \ : \ F(x) = y\} \tag{1.29}$$

is included in any stripe onto which we project in an effort to approach a solution of (1.28). A simple replacement of A^* by the adjoint $F'(x_n)^*$ of the Fréchet derivative $F'(x_n)$ at the current iterate x_n, as might be the first idea given that the current gradient plays an important role in SESOP methods, does generally not ensure that $M_{F(x)=y}$ is included in a hyperplane or stripe of the form $H\big(F'(x_n)^* w_{n,i}, \alpha_{n,i}, \xi_{n,i}\big)$ as defined previously. The reason is obvious: a solution x of the nonlinear operator equation (1.28) is in general not mapped to y by $F'(\tilde{x})$ for some $\tilde{x} \in \mathcal{D}(F)$. Furthermore, the fact that the linearization $F'(x)$ depends on the position $x \in X$ shows that the local character of nonlinear problems will need to be respected when dealing with problems like (1.28). This is strongly reflected in the following assumptions on the properties of F.

Let $F : \mathcal{D}(F) \subseteq X \to Y$ be continuous and Fréchet differentiable in an open ball

$$B_\rho(x_0) := \{x \in X \ : \ \|x - x_0\| < \rho\} \subseteq \mathcal{D}(F)$$

centered at the initial value $x_0 \in \mathcal{D}(F)$ with radius $\rho > 0$ and let the mapping

$$B_\rho(x_0) \ni x \mapsto F'(x) \tag{1.30}$$

from $B_\rho(x_0)$ to the space $L(X, Y)$ of linear operators be continuous.
We assume the existence of a solution $x^+ \in X$ of (1.28) satisfying

$$x^+ \in B_{\frac{\rho}{2}}(x_0). \tag{1.31}$$

Furthermore, we postulate that F fulfills the *tangential cone condition*

$$\big\|F(x) - F(\tilde{x}) - F'(x)(x - \tilde{x})\big\| \leq c_{\mathrm{tc}} \, \|F(x) - F(\tilde{x})\| \tag{1.32}$$

with a nonnegative constant $c_{\mathrm{tc}} < 1$, and the estimate

$$\|F'(x)\| < c_F, \tag{1.33}$$

where $c_F > 0$, for all $x, \tilde{x} \in B_\rho(x_0)$. Moreover, we assume the operator F to be weakly sequentially closed, such that for some weakly convergent sequence $\{x_n\}_{n \in \mathbb{N}}$ with $x_n \rightharpoonup x$ and $F(x_n) \to y$, we have

$$x \in \mathcal{D}(F) \text{ and } F(x) = y.$$

As before, in the case of perturbed data we assume a noise level δ and postulate

$$\big\|y^\delta - y\big\| \leq \delta.$$

Let $\{x_n\}_{n\in\mathbb{N}}$ resp. $\{x_n^\delta\}_{n\in\mathbb{N}}$ be the sequence of iterates generated by an iterative reconstruction method. The residual is defined by

$$R_n := F(x_n) - y$$

for exact data y and by

$$R_n^\delta := F(x_n^\delta) - y^\delta$$

for noisy data y^δ. For later convenience, we define the *current gradient*

$$g_n^\delta := F'(x_n^\delta)^*\big(F(x_n^\delta) - y^\delta\big) \tag{1.34}$$

in iteration $n \in \mathbb{N}$ as the gradient of the least squares functional

$$\Psi(x) := \frac{1}{2}\big\|F(x) - y^\delta\big\|^2$$

evaluated at the current iterate x_n^δ. In the noise-free case, the gradient g_n is defined analogously.

Proposition 1.12. *The validity of the tangential cone condition* (1.32) *implies that the Fréchet derivative F' fulfills $F'(x) = 0$ for some $x \in B_\rho(x_0)$ if and only if F is constant in $B_\rho(x_0)$.*

Proof. Let $F'(x) = 0$ for some $x \in B_\rho(x_0)$. For all $\tilde{x} \in B_\rho(x_0)$ the tangential cone condition yields

$$\|F(x) - F(\tilde{x})\| \leq c_{\mathrm{tc}} \, \|F(x) - F(\tilde{x})\| \, ,$$

which can only be satisfied if $F(\tilde{x}) = F(x)$ in $B_\rho(x_0)$, i.e., F is constant in $B_\rho(x_0)$.
Now let F be constant in $B_\rho(x_0)$. The tangential cone condition now yields

$$\big\|F'(x)(x - \tilde{x})\big\| \leq 0$$

for all $x, \tilde{x} \in B_\rho(x_0)$, implying $F'(x) = 0$ for $x \in B_\rho(x_0)$. ☐

Remark 1.13. *The case that F is constant in $B_\rho(x_0)$ is not interesting in this context. We thus postulate $F'(x) \neq 0$ for all $x \in B_\rho(x_0)$. The estimate* (1.33) *can thus be reformulated more precisely as*

$$0 < \|F'(x)\| < c_F. \tag{1.35}$$

Moreover, if we have $c_{\mathrm{tc}} = 0$ in (1.32)*, the operator F is linear. As we are concerned with the nonlinear case, we will thus occasionally exclude the case $c_{\mathrm{tc}} = 0$ without any further remarks.*

The projection onto hyperplanes in the linear case for exact data is convenient since the solution set itself is an affine subspace in X, spanned by elements of the null space $\mathcal{N}(A)$ of A. When dealing with nonlinear problems, this is no longer true. Our approach is to consider stripes - similar to the ones in the RESESOP scheme for linear operators - already for unperturbed data, using the tangential cone condition.
Due to the local character of nonlinear inverse problems, the stripes will be defined *locally* as well, i.e., they will depend on the point of linearization. We will see that it is sufficient for some assumptions to hold only locally in order to guarantee convergence and regularizing properties.

1.2.1. The case of exact data

We formulate a sequential subspace optimization method for nonlinear operators, based on the tangential cone condition, in the case of exact data.

Algorithm 1.14. *Choose an initial value* $x_0 \in X$. *At iteration* $n \in \mathbb{N}$, *choose a finite index set* I_n *and define*

$$H_{n,i} := H(u_{n,i}, \alpha_{n,i}, \xi_{n,i}) \tag{1.36}$$

with

$$\begin{aligned} u_{n,i} &:= F'(x_i)^* w_{n,i}, \\ \alpha_{n,i} &:= \langle F'(x_i)^* w_{n,i}, x_i \rangle - \langle w_{n,i}, F(x_i) - y \rangle, \\ \xi_{n,i} &:= c_{\mathrm{tc}} \|w_{n,i}\| \cdot \|R_i\|, \end{aligned} \tag{1.37}$$

and $w_{n,i} \in Y$ *for all* $i \in I_n$. *Compute the new iterate as*

$$x_{n+1} = x_n - \sum_{i \in I_n} t_{n,i} F'(x_i)^* w_{n,i}, \tag{1.38}$$

where $t_n := (t_{n,i})_{i \in I_n}$ *are chosen such that*

$$x_{n+1} \in \bigcap_{i \in I_n} H_{n,i}, \tag{1.39}$$

i.e., the new iterate is given by the projection

$$x_{n+1} = P_{\bigcap_{i \in I_n} H_{n,i}}(x_n) = \underset{x \in \bigcap_{i \in I_n} H_{n,i}}{\operatorname{argmin}} \|x_n - x\|.$$

The parameters $u_{n,i}$, $\alpha_{n,i}$ *and* $\xi_{n,i}$ *are chosen to guarantee the validity of a descent property*

$$\|z - x_{n+1}\|^2 \leq \|z - x_n\|^2 - C\big(\|R_n\|, c_{\mathrm{tc}}, c_F\big). \tag{1.40}$$

Definition 1.15. *We call* $u_{n,i}$, $i \in I_n$, *the* search directions *and*

$$U_n := \operatorname{span}\{u_{n,i} \, : \, i \in I_n\} \subseteq X$$

the search space *at iteration* $n \in \mathbb{N}$.

Taking a closer look at the definition of the stripes, we see that we have replaced A^* with the adjoint of the linearization of F in the iterate x_i. The width of the stripe depends on the constant c_{tc} from the cone condition (1.32). The other alterations can be interpreted as a *localization* of the hyperplanes subject to the local properties of F in a neighborhood of the initial value. This becomes clear when we write the stripe $H_{n,i}$ explicitly in the form

$$H_{n,i} := \left\{ x \in X \, : \, \big| \langle F'(x_i)^* w_{n,i}, x_i - x \rangle - \langle w_{n,i}, F(x_i) - y \rangle \big| \leq c_{\mathrm{tc}} \|w_{n,i}\| \|R_i\| \right\},$$

i.e., we have to work with distances $x_i - x$ and $F(x_i) - y$ to the current iterate, respectively the point of linearization, and to the value of F in x_i.

Proposition 1.16. *For any* $n \in \mathbb{N}$, $i \in I_n$, *the solution set* $M_{F(x)=y}$ *is contained in* $H_{n,i}$, *where* $u_{n,i}$, $\alpha_{n,i}$, *and* $\xi_{n,i}$ *are chosen as in* (1.37).

Proof. Let $z \in M_{F(x)=y}$. We then have

$$\langle u_{n,i}, z\rangle - \alpha_{n,i} = \langle w_{n,i}, F'(x_i)^*(z - x_i) + F(x_i) - y\rangle.$$

With $F(z) = y$ we obtain

$$\begin{aligned}\big|\langle w_{n,i}, F'(x_i)(z - x_i) - F(x_i) + F(z)\rangle\big| &\le \|w_{n,i}\| \cdot \|F(x_i) - F(z) - F'(x_i)(x_i - z)\| \\ &\le c_{\mathrm{tc}}\|w_{n,i}\| \cdot \|F(x_i) - y\|,\end{aligned}$$

where we have used the tangential cone condition (1.32) in the second estimate. The definition of the residual $R_i = F(x_i) - y$ now yields $z \in H_{n,i}$. □

1.2.2. The case of noisy data

Of course we want to extend our method to the case of noisy data. To this end, we again have to modify the stripes onto which we project, now incorporating the noise level. The following definition of stripes $H^\delta_{n,i}$ ensures that the solution set is contained in each stripe.

Definition 1.17. *For $n \in \mathbb{N}$, $i \in I_n$, and $w^\delta_{n,i} \in Y$ we define the stripes*

$$H^\delta_{n,i} := H\big(u^\delta_{n,i}, \alpha^\delta_{n,i}, \xi^\delta_{n,i}\big)$$

with

$$\begin{aligned} u^\delta_{n,i} &:= F'(x^\delta_i)^* w^\delta_{n,i}, \\ \alpha^\delta_{n,i} &:= \Big\langle F'(x^\delta_i)^* w^\delta_{n,i}, x^\delta_i\Big\rangle - \Big\langle w^\delta_{n,i}, F(x^\delta_i) - y^\delta\Big\rangle, \\ \xi^\delta_{n,i} &:= \Big(\delta + c_{\mathrm{tc}}(\|R^\delta_i\| + \delta)\Big)\, \|w^\delta_{n,i}\|. \end{aligned} \tag{1.41}$$

We obtain the analogous statement as in the noise-free case.

Proposition 1.18. *For $n \in \mathbb{N}$ and $i \in I^\delta_n$, let $u^\delta_{n,i}$, $\alpha^\delta_{n,i}$, and $\xi^\delta_{n,i}$ be defined as in Definition 1.17. Then the solution set $M_{F(x)=y}$ is contained in each stripe $H^\delta_{n,i}$.*

Proof. We proceed as in the proof of Proposition 1.16 and obtain

$$\begin{aligned}\Big|\Big\langle u^\delta_{n,i}, z\Big\rangle - \alpha^\delta_{n,i}\Big| &= \Big|\Big\langle w^\delta_{n,i}, F'(x^\delta_i)(z - x^\delta_i) + F(x^\delta_i) - F(z) + F(z) - y^\delta\Big\rangle\Big| \\ &\le \Big\|w^\delta_{n,i}\Big\| \cdot \Big(\Big\|F(x^\delta_i) - F(z) - F'(x^\delta_i)(x^\delta_i - z)\Big\| + \Big\|y^\delta - y\Big\|\Big) \\ &\le \Big\|w^\delta_{n,i}\Big\| \cdot \Big(c_{\mathrm{tc}}\|F(x^\delta_i) - y^\delta + y^\delta - F(z)\| + \delta\Big) \\ &\le \Big\|w^\delta_{n,i}\Big\| \cdot \Big(c_{\mathrm{tc}}\Big(\|R^\delta_i\| + \delta\Big) + \delta\Big)\end{aligned}$$

for any $z \in M_{F(x)=y}$. □

For the following algorithm we specify our choice of the function $w^\delta_{n,n}$ as the current residual. This choice guarantees the validity of the descent property, which will be analyzed in the subsequent section.

Algorithm 1.19. *Choose an initial value* $x_0^\delta := x_0$ *and fix some constant* $\tau > 1$. *At iteration* $n \in \mathbb{N}$, *choose a finite index set* I_n^δ *and search directions* $F'(x_i^\delta)^* w_{n,i}^\delta$. *If the residual* $R_n^\delta = F(x_n^\delta) - y^\delta$ *satisfies the discrepancy principle*

$$\|R_n^\delta\| \leq \tau\delta, \tag{1.42}$$

stop iterating. Otherwise, compute the new iterate as

$$x_{n+1}^\delta = x_n^\delta - \sum_{i \in I_n^\delta} t_{n,i}^\delta F'(x_i^\delta)^* w_{n,i}^\delta, \tag{1.43}$$

choosing $t_n^\delta = (t_{n,i}^\delta)_{i \in I_n^\delta}$ *such that*

$$x_{n+1}^\delta \in \bigcap_{i \in I_n^\delta} H(u_{n,i}^\delta, \alpha_{n,i}^\delta, \xi_{n,i}^\delta), \tag{1.44}$$

where $u_{n,i}^\delta$, $\alpha_{n,i}^\delta$, *and* $\xi_{n,i}^\delta$ *are defined as in Definition 1.17, and such that an estimate of the form*

$$\|z - x_{n+1}^\delta\|^2 \leq \|z - x_n^\delta\|^2 - C\big(\|R_n^\delta\|, \delta, c_{\mathrm{tc}}, c_F\big) \tag{1.45}$$

holds for all $z \in M_{F(x)=y}$ *for some constant* $C > 0$, *which depends on the norm of the current residual, the noise level* δ, *the cone condition and the norm of the Fréchet derivative.*

Remark 1.20. *The choice* $n \in I_n$ *and* $F'(x_n^\delta)^* w_{n,n}^\delta = F'(x_n^\delta)^*(F(x_n^\delta) - y^\delta)$ *turns out to be a handy choice. By setting*

$$\tau > \frac{1 + c_{\mathrm{tc}}}{1 - c_{\mathrm{tc}}},$$

which assures that $x_n^\delta \in H_>\big(u_{n,n}^\delta, \alpha_{n,n}^\delta, \xi_{n,n}^\delta\big)$ *and projecting first onto the stripe* $H_{n,n}^\delta$, *we obtain a descent if the other search directions are chosen appropriately. We exploit this property and present a regularizing method, inspired by these findings, and give the respective proof.*

In the following section, we want to introduce a special case of the above algorithm, where the choice of search directions not only provides a fast regularized solution of a nonlinear problem as in (1.28), but also admits a good understanding of the structure of the method. We see that the current gradient as a search direction plays an important role, as it guarantees that a descent property holds.

1.2.3. An algorithm with two search directions

In analogy to Algorithm 1.10 we want to develop a fast method for nonlinear operator equations, where we use only two search directions in each iteration. For linear problems, this method provides a fast algorithm to calculate a regularized solution of (1.1), where in each step the search space is spanned by the gradients g_n^δ and g_{n-1}^δ, see also [69]. In the first step, only the gradient g_0^δ is used, so that the first iteration is similar to a Landweber step.
We will adapt this method for nonlinear inverse problems (1.28) in Hilbert spaces. Later, we show convergence properties for our proposed algorithm. Also we show that, together with the discrepancy principle as a stopping rule, we obtain a regularization method for the solution of (1.28).

The following algorithm is a special case of Algorithm 1.19, where we have chosen $I_0^\delta = \{0\}$ and $I_n^\delta = \{n-1, n\}$ for all $n \geq 1$. For convenience, we skip the first index n in the subscript of the functions and parameters we are dealing with.

Algorithm 1.21. *(RESESOP for nonlinear operators with two search directions) Choose an initial value* $x_0^\delta := x_0 \in X$. *In the first step* ($n = 0$) *choose* u_0^δ *as the search direction. For all* $n \geq 1$, *choose the two search directions* $\{u_n^\delta, u_{n-1}^\delta\}$, *where*

$$\begin{aligned} u_n^\delta &:= F'(x_n^\delta)^* w_n^\delta, \\ w_n^\delta &:= F(x_n^\delta) - y^\delta. \end{aligned} \tag{1.46}$$

Define $H_{-1}^\delta := X$ *and, for* $n \in \mathbb{N}$, *the stripes*

$$H_n^\delta := H(u_n^\delta, \alpha_n^\delta, \xi_n^\delta) \tag{1.47}$$

with

$$\begin{aligned} \alpha_n^\delta &:= \left\langle u_n^\delta, x_n^\delta \right\rangle - \|R_n^\delta\|^2, \\ \xi_n^\delta &:= \|R_n^\delta\| \big(\delta + c_{\mathrm{tc}}(\|R_n^\delta\| + \delta)\big). \end{aligned} \tag{1.48}$$

As a stopping rule choose the discrepancy principle, where

$$\tau > \frac{1 + c_{\mathrm{tc}}}{1 - c_{\mathrm{tc}}} > 1. \tag{1.49}$$

As long as $\|R_n^\delta\| > \tau\delta$, *we have*

$$x_n^\delta \in H_>(u_n^\delta, \alpha_n^\delta + \xi_n^\delta) \cap H_{n-1}^\delta, \tag{1.50}$$

and thus calculate the new iterate x_{n+1}^δ *according to the following two steps.*

(i) Compute

$$\begin{aligned} \tilde{x}_{n+1}^\delta &:= P_{H(u_n^\delta, \alpha_n^\delta + \xi_n^\delta)}(x_n^\delta) \\ &= x_n^\delta - \frac{\langle u_n^\delta, x_n^\delta \rangle - (\alpha_n^\delta + \xi_n^\delta)}{\|u_n^\delta\|^2} u_n^\delta. \end{aligned} \tag{1.51}$$

Then the descent property

$$\left\| z - \tilde{x}_{n+1}^\delta \right\|^2 \leq \left\| z - x_n^\delta \right\|^2 - \left(\frac{\|R_n^\delta\| \left(\|R_n^\delta\| - \delta - c_{\mathrm{tc}}(\|R_n^\delta\| + \delta) \right)}{\|u_n^\delta\|} \right)^2$$

is valid for all $z \in M_{F(x)=y}$.
If $\tilde{x}_{n+1}^\delta \in H_{n-1}^\delta$, *we have* $\tilde{x}_{n+1}^\delta = P_{H_n^\delta \cap H_{n-1}^\delta}(x_n^\delta)$ *and we are done. Otherwise, go to step (ii).*

(ii) First, decide whether $\tilde{x}_{n+1}^\delta \in H_>(u_{n-1}^\delta, \alpha_{n-1}^\delta + \xi_{n-1}^\delta)$ *or* $\tilde{x}_{n+1}^\delta \in H_<(u_{n-1}^\delta, \alpha_{n-1}^\delta - \xi_{n-1}^\delta)$. *Calculate accordingly*

$$x_{n+1}^\delta := P_{H(u_n^\delta, \alpha_n^\delta + \xi_n^\delta) \cap H(u_{n-1}^\delta, \alpha_{n-1}^\delta \pm \xi_{n-1}^\delta)}(\tilde{x}_{n+1}^\delta),$$

i.e., determine $x_{n+1}^\delta = \tilde{x}_{n+1}^\delta - t_{n,n}^\delta u_n^\delta - t_{n,n-1}^\delta u_{n-1}^\delta$ *such that* $\left(t_{n,n}^\delta, t_{n,n-1}^\delta\right)$ *minimizes the function*

$$h_2(t_1, t_2) := \frac{1}{2} \left\| \tilde{x}_{n+1}^\delta - t_1 u_n^\delta - t_2 u_{n-1}^\delta \right\|^2 + t_1 \left(\alpha_n^\delta + \xi_n^\delta \right) + t_2 \left(\alpha_{n-1}^\delta \pm \xi_{n-1}^\delta \right).$$

Then we have $x_{n+1}^\delta = P_{H_n^\delta \cap H_{n-1}^\delta}(x_n^\delta)$ *and for all* $z \in M_{F(x)=y}$ *the descent property*

$$\left\| z - x_{n+1}^\delta \right\|^2 \leq \left\| z - x_n^\delta \right\|^2 - S_n^\delta \tag{1.52}$$

is satisfied, where

$$\begin{aligned} S_n^\delta := &\left(\frac{\|R_n^\delta\| \left(\|R_n^\delta\| - \delta - c_{\mathrm{tc}}(\|R_n^\delta\| + \delta) \right)}{\|u_n^\delta\|} \right)^2 \\ &+ \left(\frac{\left| \langle u_{n-1}^\delta, \tilde{x}_{n+1}^\delta \rangle - (\alpha_{n-1}^\delta \pm \xi_{n-1}^\delta) \right|}{\gamma_n \left\| u_{n-1}^\delta \right\|} \right)^2 \end{aligned}$$

and

$$\gamma_n := \left(1 - \left(\frac{\left| \langle u_n^\delta, u_{n-1}^\delta \rangle \right|}{\|u_n^\delta\| \cdot \left\| u_{n-1}^\delta \right\|} \right)^2 \right)^{\frac{1}{2}} \qquad \in (0, 1].$$

Remark 1.22. *The RESESOP method with two search directions allows a good insight into sequential subspace optimization methods.*

(a) The validity of the statements made in Algorithm 1.21 are a consequence of Proposition 1.8. The explicit forms of the parameters $t_{n,n}^\delta$ *and* $t_{n,n-1}^\delta$ *are directly obtained from the respective proof and are given in the appendix A.2. By projecting first onto the stripe* H_n^δ*, we make sure that a descent property holds to guarantee weak convergence, as we will see in the following section.*

(b) As mentioned before in Remark 1.9, calculating the projection of $x \in X$ *onto the intersection of two halfspaces or stripes by first projecting onto one of them and then projecting onto the intersection does not necessarily lead to the correct result if* x *is not contained in at least one of them. In our algorithm we avoid this problem: By choosing* τ *according to* (1.49)*, we guarantee that in iteration* n *(provided the iteration has not been stopped yet) the iterate* x_n^δ *is an element of* $H_>(u_n^\delta, \alpha_n^\delta + \xi_n^\delta) \cap H_{n-1}^\delta$*, which determines the order of projection that leads to the desired result.*

As x_n^δ *is the projection of* x_{n-1}^δ *onto* $H_{n-1}^\delta \cap H_{n-2}^\delta$*, we have* $x_n^\delta \in H_{n-1}^\delta$*. To see that* (1.50) *is valid as long as* $\|R_n^\delta\| > \tau\delta$*, we note that* (1.49) *implies*

$$\|R_n^\delta\| > \tau\delta > \delta \frac{1 + c_{\mathrm{tc}}}{1 - c_{\mathrm{tc}}}.$$

Because of $0 \leq c_{\mathrm{tc}} < 1$ *we obtain*

$$\|R_n^\delta\| - c_{\mathrm{tc}}\|R_n^\delta\| - \delta c_{\mathrm{tc}} - \delta > 0,$$

yielding

$$\alpha_n^\delta + \xi_n^\delta = \langle u_n^\delta, x_n^\delta \rangle - \|R_n^\delta\| \cdot \Big(\|R_n^\delta\| - c_{\mathrm{tc}}\|R_n^\delta\| - \delta c_{\mathrm{tc}} - \delta \Big) < \langle u_n^\delta, x_n^\delta \rangle.$$

Thus $x_n^\delta \in H_>(u_n^\delta, \alpha_n^\delta + \xi_n^\delta)$ *and we obtain* (1.50)*.*

(c) *The choice* (1.49) *for τ depends strongly on the constant c_{tc} from the tangential cone condition. The smaller c_{tc}, the better the approximation of F by its linearization. Of course $c_{\mathrm{tc}} = 0$ implies the linearity of F. A large value of c_{tc}, on the other hand, demands a bigger tolerance $\tau\delta$ in the data fitting term (the residual), such that the algorithm has to be stopped at a larger value of the residual's norm and the source is possibly reconstructed with a larger error.*

(d) *As already stated in [69, 70], the improvement due to step (ii) might be significant, if the search directions u_n^δ and u_{n-1}^δ fulfill*

$$\frac{|\langle u_n^\delta, u_{n-1}^\delta \rangle|}{\|u_n^\delta\| \cdot \|u_{n-1}^\delta\|} \approx 1,$$

since in that case the coefficient γ_n is quite small and therefore S_n^δ is large. This can be illustrated by looking at the situation where $u_n^\delta \perp u_{n-1}^\delta$: The projection of x_n^δ onto H_n^δ is already contained in H_{n-1}^δ, such that step (ii) will not lead to any further improvement.
This suggests an interesting interpretation: If the new search direction is chosen perpendicular to the previous one, the choice is optimal in view of the steepest possible descent. This motivates the approach of Heber et al. [40].

(e) *Algorithm 1.21 is very useful for an implementation. First of all, the search direction u_{n-1}^δ has already been calculated for the preceding iteration and can be reused. Furthermore, the residual R_n^δ was necessarily calculated to see if the discrepancy principle is fulfilled and can also be reused as we have $w_n^\delta := F(x_n^\delta) - y^\delta = R_n^\delta$. So the only costly computation is the determination of $F'(x_n^\delta)^* R_n^\delta$. In some applications, for example in parameter identification, this corresponds to a numerical evaluation of a (partial) differential equation. The effort is thus comparable to Landweber type iterations, but the algorithm may be faster as discussed in the previous point.*

Proposition 1.23. *Algorithm 1.21 can be transferred to the noise-free case by setting $\delta = 0$ (however, the discrepancy principle has to be replaced by some other stopping criterion, for instance a maximal number of iterations). In particular,* (1.50) *remains valid, and the metric projection onto the intersection of the two stripes is obtained executing the two steps of the algorithm.*

Proof. We have $0 < 1 - c_{\mathrm{tc}} < 1$ and thus

$$\alpha_n + \xi_n = \langle u_n, x_n \rangle - \|R_n\|^2 + c_{\mathrm{tc}}\|R_n\|^2 = \langle u_n, x_n \rangle - (1 - c_{\mathrm{tc}})\|R_n\|^2 < \langle u_n, x_n \rangle.$$

The remainder of the proof follows the same lines as in the treatment of the noisy case. □

1.3. Convergence and regularization properties

At this point, we want to analyze the methods presented in Section 1.2. Using the conditions we postulated at the beginning of Section 1.2, we will show convergence results for the SESOP respective RESESOP algorithms which we adapted to solving nonlinear inverse problems (1.28). For a special choice of search directions in Algorithm 1.19, which includes Algorithm 1.21, we will prove that the method yields a regularized solution of the nonlinear problem with noisy data.

We want to begin with an analysis of the methods in the case of exact data.

Proposition 1.24. *Consider exact data $y \in Y$. Let $\{x_n\}_{n\in\mathbb{N}}$ be the sequence of iterates generated by Algorithm 1.14, where in each step $n \in \mathbb{N}$ of the iteration we let $n \in I_n$ and choose $w_{n,n} := F(x_n)-y$, such that the search direction $u_{n,n} = g_n$ is the current gradient. Then we have*

$$x_n \in H_>(u_{n,n}, \alpha_{n,n} + \xi_{n,n}),$$

where $\alpha_{n,n}$ and $\xi_{n,n}$ are chosen as in Algorithm 1.14. By projecting x_n first onto $H(u_{n,n}, \alpha_{n,n}, \xi_{n,n})$, we obtain

$$\|z - x_{n+1}\|^2 \leq \|z - P_{H(u_{n,n},\alpha_{n,n},\xi_{n,n})}(x_n)\|^2 \leq \|z - x_n\|^2 - \frac{(1-c_{\mathrm{tc}})^2}{\|F'(x_n)\|^2}\|R_n\|^2 \tag{1.53}$$

for $z \in M_{F(x)=y}$.

Proof. The first estimate is due to an adequate choice of the stripes. According to our choice of $w_{n,n} = F(x_n) - y = R_n$ we have

$$\begin{aligned} \alpha_{n,n} &= \langle u_{n,n}, x_n\rangle - \|R_n\|^2, \\ \xi_{n,n} &= c_{\mathrm{tc}}\|R_n\|^2, \end{aligned}$$

and thus $\langle u_{n,n}, x_n\rangle - \alpha_{n,n} = \|R_n\|^2 > \xi_{n,n}$ as $0 < c_{\mathrm{tc}} < 1$. The descent property (i.e., the second estimate) is easily obtained with the help of (1.11), (1.12), (1.13), and the estimate

$$\|F'(x_n)^*(F(x_n) - y)\| \leq \|F'(x_n)\| \cdot \|R_n\|.$$

Note that $\|F'(x_n)\| > 0$, see Proposition 1.12 and the subsequent remark. ☐

Proposition 1.25. *The sequence of iterates $\{x_n\}_{n\in\mathbb{N}}$, generated by Algorithm 1.14, fulfills*

$$x_n \in B_\rho(x_0) \quad \textit{for all } n \in \mathbb{N}$$

and has a subsequence $\{x_{n_k}\}_{k\in\mathbb{N}}$ that converges weakly to a solution of (1.28), *if we choose $n \in I_n$ and $w_{n,n} = F(x_n) - y$ for every iteration $n \in \mathbb{N}$.*

Proof. By assumption (1.31), there exists a solution $x^+ \in B_{\frac{\rho}{2}}(x_0) \subseteq \mathcal{D}(F)$. We use Proposition 1.24 and obtain $x_1 \in B_{\frac{\rho}{2}}(x_0)$ due to

$$\|x^+ - x_1\|^2 \leq \|x^+ - x_0\|^2 \leq \frac{\rho^2}{4}.$$

Thus, by induction, the descent property (1.53) yields $x_n \in B_{\frac{\rho}{2}}(x^+)$. We conclude

$$\|x_n - x_0\| \leq \|x_n - x^+\| + \|x^+ - x_0\| \leq \rho,$$

so that $x_n \in B_\rho(x_0)$ for all $n \in \mathbb{N}$ and the sequence $\{\|x_n - x^+\|\}_{n\in\mathbb{N}}$ is bounded and monotonically decreasing.

We thus have a weakly convergent subsequence $\{x_{n_k}\}_{k\in\mathbb{N}}$ with a limit $\hat{x} := \sigma\text{-}\lim_{k\to\infty} x_{n_k}$ (see Section A.1). It remains to show that $\hat{x} \in M_{F(x)=y}$. For that purpose, we use again the descent property (1.53) and the estimate (1.33), which is valid in $B_\rho(x_0)$, to obtain

$$\|x^+ - x_{n_k}\|^2 - \|x^+ - x_{n_{k+1}}\|^2 \geq \frac{(1-c_{\mathrm{tc}})^2}{\|F'(x_{n_k})\|^2}\|R_{n_k}\|^2 \geq \frac{(1-c_{\mathrm{tc}})^2}{c_F^2}\|R_{n_k}\|^2.$$

Let $K \in \mathbb{N}$ be an arbitrary index. The subsequence $\{x_{n_k}\}_{k\in\mathbb{N}}$ fulfills

$$\begin{aligned}\sum_{k=0}^{K} \|R_{n_k}\|^2 &\leq \left(\frac{c_F}{1-c_{\mathrm{tc}}}\right)^2 \sum_{k=0}^{K} \left(\|x^+ - x_{n_k}\|^2 - \|x^+ - x_{n_{k+1}}\|^2\right) \\ &= \left(\frac{c_F}{1-c_{\mathrm{tc}}}\right)^2 \cdot \left(\|x^+ - x_{n_0}\|^2 - \|x^+ - x_{n_{K+1}}\|^2\right) \\ &\leq \left(\frac{c_F}{1-c_{\mathrm{tc}}}\right)^2 \cdot \|x^+ - x_{n_0}\|^2 \quad < \infty.\end{aligned}$$

This remains true for the limit $K \to \infty$, yielding the absolute convergence of the series $\sum_{k=0}^{\infty}\|R_{n_k}\|^2$. Consequently, the sequence $\{\|R_{n_k}\|\}_{k\in\mathbb{N}}$ has to be a null sequence, i.e., $\|F(x_{n_k})-y\| \to 0$ for $k \to \infty$. As F is continuous and weakly sequentially closed, we have $F(\hat{x}) = \lim_{k\to\infty} F(x_{n_k}) = y$. ☐

Remark 1.26. *If there is a unique solution $x^+ \in B_\rho(x_0)$ of* (1.28)*, we obtain the strong convergence of the sequence from Proposition 1.25, if X is finite-dimensional: As each subsequence of $\{x_n\}_{n\in\mathbb{N}}$ is bounded, it contains a weakly convergent subsequence which, in a finite dimensional Hilbert space, is strongly convergent. Thus, the whole sequence converges strongly to a solution of* (1.28)*, because a sequence converges to a certain point if and only if each subsequence possesses a subsequence converging to this point. In [68], this has been discussed in some more detail for linear problems in Banach spaces.*

Theorem 1.27. *Let $N \geq 1$ be a fixed integer and $n \in I_n$ for each $n \in \mathbb{N}$. We additionally choose*

$$I_n \subseteq \{n-N+1, ..., n\} \cap \mathbb{N}$$

and set

$$w_{n,i} := R_i = F(x_i) - y$$

for each $i \in I_n$. If $x^+ \in B_{\frac{\rho}{2}}(x_0)$ is the unique solution of (1.28) *in $B_\rho(x_0)$, the sequence of iterates $\{x_n\}_{n\in\mathbb{N}}$ generated by Algorithm 1.14 converges strongly to x^+, if the optimization parameters $t_{n,i}$ fulfill*

$$|t_{n,i}| \leq t \tag{1.54}$$

for some $t > 0$ for all $i \in I_n$ and $n \in \mathbb{N}$.

Proof. Inspired by the proof of Theorem 2.3 from [39], we will show that the sequence $\{x_n\}_{n\in\mathbb{N}}$ is a Cauchy sequence. For that purpose, it suffices to verify that $\{a_n\}_{n\in\mathbb{N}}$, given by

$$a_n := x_n - x^+,$$

is a Cauchy sequence.
Since our choices yield $F'(x_n)^* w_{n,n} = g_n$ (i.e., the search direction $u_{n,n}$ in Algorithm 1.14 is the current gradient), we can apply Proposition 1.25. We have seen in the respective proof that $\{\|a_n\|\}_{n\in\mathbb{N}}$ is a bounded monotonically decreasing sequence. So we have

$$\|a_n\| \to \varepsilon \quad \text{as } n \to \infty,$$

for an $\varepsilon \geq 0$. Fix $n \in \mathbb{N}$, let $j \geq n$, and choose the index $l = l(n,j)$ with $n \leq l \leq j$ such that

$$\|R_l\| = \|F(x_l) - y\| \leq \|F(x_m) - y\| = \|R_m\| \quad \text{for all } n \leq m \leq j.$$

We have $\|a_j - a_n\| \leq \|a_j - a_l\| + \|a_l - a_n\|$ and

$$\begin{aligned}\|a_j - a_l\|^2 &= 2\langle a_l - a_j, a_l\rangle + \|a_j\|^2 - \|a_l\|^2,\\ \|a_l - a_n\|^2 &= 2\langle a_l - a_n, a_l\rangle + \|a_n\|^2 - \|a_l\|^2.\end{aligned}$$

When $n \to \infty$, we have $\|a_j\|^2 \to \varepsilon^2$, $\|a_l\|^2 \to \varepsilon^2$ and $\|a_n\|^2 \to \varepsilon^2$. To prove $\|a_j - a_l\| \to 0$ for $n \to \infty$, we have to show that $\langle a_l - a_j, a_l\rangle \to 0$ as n tends to infinity. To this end, we note that for $j > l$ we have

$$\begin{aligned}a_j - a_l &= x_j - x_l\\ &= x_{j-1} - x_l - \sum_{i\in I_{j-1}} t_{j-1,i} F'(x_i)^* w_{j-1,i}\end{aligned}$$

by (1.38). Iterating this, we arrive at

$$a_j - a_l = -\sum_{k=l}^{j-1}\sum_{i\in I_k} t_{k,i} F'(x_i)^* w_{k,i},$$

which is also valid if $j = l$. We thus obtain

$$\begin{aligned}|\langle a_l - a_j, a_l\rangle| &= \left|\left\langle \sum_{k=l}^{j-1}\sum_{i\in I_k} t_{k,i} F'(x_i)^* w_{k,i}, a_l\right\rangle\right|\\ &\leq \sum_{k=l}^{j-1}\sum_{i\in I_k} |t_{k,i}| \left|\left\langle F'(x_i)^* w_{k,i}, a_l\right\rangle\right|\\ &\leq \sum_{k=l}^{j-1}\sum_{i\in I_k} |t_{k,i}|\, \|w_{k,i}\| \left\|F'(x_i)(x_l - x^+)\right\|,\end{aligned}$$

where we have used the Cauchy-Schwarz inequality. We estimate

$$\begin{aligned}\left\|F'(x_i)(x_l - x^+)\right\| &\leq \left\|y - F(x_i) + F'(x_i)(x_i - x^+)\right\|\\ &\quad + \left\|F(x_i) - F(x_l) - F'(x_i)(x_i - x_l)\right\| + \|F(x_l) - y\|\\ &\leq c_{\mathrm{tc}}\|F(x_i) - y\| + c_{\mathrm{tc}}\|F(x_i) - F(x_l)\| + \|F(x_l) - y\|\\ &\leq 2c_{\mathrm{tc}}\|F(x_i) - y\| + (1 + c_{\mathrm{tc}})\|F(x_l) - y\|\\ &\leq (3c_{\mathrm{tc}} + 1)\|F(x_i) - y\|.\end{aligned}$$

Notice that the last inequality is valid due to the choice of l. The choice $w_{k,i} = F(x_i) - y$ and the boundedness assumption (1.54) imposed on the optimization parameters $t_{k,i}$ yield

$$\begin{aligned}|\langle a_l - a_j, a_l\rangle| &\leq (3c_{\mathrm{tc}} + 1)\sum_{k=l}^{j-1}\sum_{i\in I_k} |t_{k,i}|\, \|F(x_i) - y\|^2\\ &\leq (3c_{\mathrm{tc}} + 1)t\sum_{k=l}^{j-1}\sum_{i\in I_k} \|F(x_i) - y\|^2.\end{aligned} \tag{1.55}$$

Note that due to $I_k \subseteq \{k - N + 1, ..., k\}$ for a fixed $N \geq 1$, the sum over $i \in I_k$ is a finite sum with at most N summands. This allows us to use a similar calculation as in the proof of Proposition 1.25. According to (1.53), we have, together with our assumptions on F,

$$\left\|x^+ - x_{i+1}\right\|^2 \leq \left\|x^+ - x_i\right\|^2 - \frac{(1 - c_{\mathrm{tc}})^2}{\|F'(x_i)\|^2}\|R_i\|^2 \leq \left\|x^+ - x_i\right\|^2 - \frac{(1 - c_{\mathrm{tc}})^2}{c_F^2}\|R_i\|^2,$$

such that

$$\left\|x^+ - x_i\right\|^2 - \left\|x^+ - x_{i+1}\right\|^2 \geq \frac{(1-c_{\mathrm{tc}})^2}{c_F^2} \left\|R_i\right\|^2.$$

This yields

$$\sum_{i=0}^{K} \|R_i\|^2 \leq \frac{c_F^2}{(1-c_{\mathrm{tc}})^2}\left(\left\|x^+ - x_0\right\|^2 - \left\|x^+ - x_{K+1}\right\|^2\right) \leq \frac{c_F^2}{(1-c_{\mathrm{tc}})^2}\rho^2$$

for each $K > 0$ and consequently, $\{\|R_i\|\}_{i\in\mathbb{N}}$ is a null sequence. We deduce that the right-hand side of

$$|\langle a_l - a_j, a_l\rangle| \leq (3c_{\mathrm{tc}} + 1)t \sum_{k=l}^{j-1} \sum_{i\in I_k} \|R_i\|^2$$

(see (1.55)) tends to 0 as $n \to \infty$ due to our choice of I_k. As a consequence, the sequence $\{\|a_n\|\}_{n\in\mathbb{N}}$ is a Cauchy sequence and so is the sequence $\{x_n\}_{n\in\mathbb{N}}$, which converges due to the weak sequential closedness of F to the unique solution $x^+ \in B_\rho(x_0)$ as the sequence of residuals tends to 0 for $n \to \infty$. ☐

We now want to deal with the sequences generated by Algorithms 1.19 and 1.21 for noisy data y^δ with noise level

$$\left\|y - y^\delta\right\| \leq \delta.$$

Definition 1.28. *For Algorithms 1.19 and 1.21 presented in Section 1.2 we define the* stopping index

$$n_* := n_*(\delta) := \min\{n \in \mathbb{N} : \|R_n^\delta\| \leq \tau\delta\}$$

as the smallest iteration index at which the discrepancy principle is fulfilled.
(In case $\{n \in \mathbb{N} : \|R_n^\delta\| \leq \tau\delta\} = \emptyset$, we set $n_* := \infty$.)

In Algorithm 1.21, we have postulated that the parameter τ, which is used in the discrepancy principle, satisfies

$$\tau > \frac{1 + c_{\mathrm{tc}}}{1 - c_{\mathrm{tc}}}.$$

This choice has been useful as it allows a simple, stepwise calculation of the desired metric projection, which guarantees the validity of the descent property.
For simplicity, we put $x_n^\delta := x_{n_*}^\delta$ for all $n > n_*$.

Lemma 1.29. *Let τ be chosen according to* (1.49). *If the gradient $g_n^\delta = F'(x_n^\delta)^*(F(x_n^\delta) - y^\delta)$ of the functional $\frac{1}{2}\|F(x) - y^\delta\|^2$ in x_n^δ is included in the search space U_n^δ for $n \in \mathbb{N}$ in Algorithm 1.19 and the current iterate x_n^δ is first projected onto the stripe $H\big(g_n^\delta, \alpha_{n,n}^\delta, \xi_{n,n}^\delta\big)$, the sequence $\big\{\big\|z - x_n^\delta\big\|\big\}_{n\in\mathbb{N}}$ with $z \in B_\rho(x_0) \cap M_{F(x)=y}$ decreases monotonically.*

Proof. As we have seen before, in particular in Remark 1.22 (b), the choice (1.49) of τ yields $x_n^\delta \in H_>(u_{n,n}^\delta, \alpha_{n,n}^\delta + \xi_{n,n}^\delta)$ for $n < n_*$ if we set $w_{n,n}^\delta := R_n^\delta$ in Definition 1.17, such that the current gradient is included in the search space due to $u_{n,n}^\delta = g_n^\delta$.
By projecting x_n^δ first onto the stripe $H(u_{n,n}^\delta, \alpha_{n,n}^\delta, \xi_{n,n}^\delta)$, we use (1.13) and obtain

$$\tilde{x}_{n+1}^\delta := P_{H(u_{n,n}^\delta, \alpha_{n,n}^\delta + \xi_{n,n}^\delta)}(x_n^\delta) = x_n^\delta - \frac{\big\langle u_{n,n}^\delta, x_n^\delta\big\rangle - \big(\alpha_{n,n}^\delta + \xi_{n,n}^\delta\big)}{\|u_{n,n}^\delta\|^2} u_{n,n}^\delta,$$

and with $\|z - x_{n+1}^\delta\|^2 \le \|z - \tilde{x}_{n+1}^\delta\|^2$ the estimate

$$\|z - x_{n+1}^\delta\|^2 \le \|z - x_n^\delta\|^2 - \left(\frac{\|R_n^\delta\| \left(\|R_n^\delta\| - \delta - c_{\mathrm{tc}}(\|R_n^\delta\| + \delta) \right)}{\left\| u_{n,n}^\delta \right\|} \right)^2, \tag{1.56}$$

which is a result of Proposition 1.8 for the choice of the halfspaces in Algorithm 1.19. This proves the monotonicity of the sequence $\left\{ \left\| z - x_n^\delta \right\| \right\}_{n\in\mathbb{N}}$, which is constant for $n \ge n_*$. ☐

Theorem 1.30. *Provided the current gradient g_n^δ is contained in the search space U_n^δ and the parameter τ is chosen such that*

$$\tau > \frac{1 + c_{\mathrm{tc}}}{1 - c_{\mathrm{tc}}},$$

the discrepancy principle yields a finite stopping index $n_* = n_*(\delta)$ in Algorithm 1.19.

Proof. Let us assume that the discrepancy principle is not satisfied for any iteration index $n \in \mathbb{N}$. We then have $\delta < \frac{1}{\tau}\|R_n^\delta\|$ for all $n \in \mathbb{N}$. However, Lemma 1.29 is applicable and equation (1.56) thus yields

$$\begin{aligned}\|z - x_{n+1}^\delta\|^2 &\le \|z - x_n^\delta\|^2 - \left(\frac{\|R_n^\delta\| \left(\|R_n^\delta\| - \delta - c_{\mathrm{tc}}(\|R_n^\delta\| + \delta) \right)}{\|F'(x_n^\delta)^* R_n^\delta\|} \right)^2 \\ &\le \|z - x_n^\delta\|^2 - \left(\frac{\|R_n^\delta\| - \delta - c_{\mathrm{tc}}(\|R_n^\delta\| + \delta)}{\|F'(x_n^\delta)\|} \right)^2 \\ &\le \|z - x_n^\delta\|^2 - \left(\frac{1 - c_{\mathrm{tc}} - \frac{1}{\tau}(1 + c_{\mathrm{tc}})}{c_F} \right)^2 \cdot \|R_n^\delta\|^2,\end{aligned}$$

where we have

$$1 - c_{\mathrm{tc}} - \frac{1}{\tau}(1 + c_{\mathrm{tc}}) > 0$$

according to our choice of τ. By a calculation as in the proof of Proposition 1.25 we find that $\{\|R_n^\delta\|\}_{n\in\mathbb{N}}$ is a null sequence. This is a contradiction to our assumption $\|R_n^\delta\| > \tau\delta$ for all $n \in \mathbb{N}$. Consequently, there must be a finite stopping index n_* fulfilling the discrepancy principle. ☐

We now want to deal with the sequence of iterates generated by Algorithm 1.19 with the choices

$$\begin{aligned}&I_n^\delta \subseteq \{n - N + 1, ..., n\} \cap \mathbb{N}, \\ &n \in I_n^\delta, \\ &w_{n,i}^\delta = R_i^\delta \text{ for all } i \in I_n^\delta\end{aligned} \tag{1.57}$$

for all $n \in \mathbb{N}$, where N is a fixed integer (see also Theorem 1.27) and such that the search directions $u_{n,i}^\delta$, $i \in I_n^\delta$, are linearly independent for each n. In particular, we thus make use of the current gradient (as $n \in I_n^\delta$ and $w_{n,n}^\delta = R_n^\delta$), such that the previous statements apply to the sequence of iterates generated by Algorithm 1.19. Most notably, we know that Algorithm 1.19 terminates after a finite number $n_*(\delta)$ of iterations. It remains to show that the final iterate $x_{n_*(\delta)}^\delta$ is a regularized solution of the nonlinear operator equation (1.28), when only perturbed data y^δ are given.

Theorem 1.31. *Let* $x^+ \in B_{\frac{\rho}{2}}(x_0)$ *be the unique solution of* (1.28) *in* $B_\rho(x_0)$. *Algorithm 1.19 together with the choices* (1.57) *and the discrepancy principle yields a regularized solution* $x^\delta_{n_*}$ *of the nonlinear problem* (1.28), *when only noisy data* y^δ *are given, i.e., we have*

$$x^\delta_{n_*(\delta)} \to x^+ \quad \text{for } \delta \to 0, \tag{1.58}$$

if there is only one solution $x^+ \in B_\rho(x_0)$ *and if* $\lim_{\delta\to 0} \left| t^\delta_{n,i} \right| < t$ *for all* $n \in \mathbb{N}$ *and* $i \in I^\delta_n$ *for some* $t > 0$.

To prove this theorem, we need to show that for a fixed iteration index n, the iterate x^δ_n depends continuously on the data y^δ. For that purpose, we first prove the following lemma.

Lemma 1.32. *Let* $x^\delta_0 = x_0$ *be the initial value of the Algorithms 1.14 and 1.19 with the choices* (1.57), *where we choose* $\delta = 0$ *in Algorithm 1.14. Let* $\{x_n\}_{n\in\mathbb{N}}$ *and* $\{x^\delta_n\}_{n\in\mathbb{N}}$ *be the respective sequences of iterates generated by these algorithms. For a fixed index* $n \in \mathbb{N}$, *the iterate* x^δ_n *depends continuously on the data* y^δ *and we have*

$$x^\delta_n \to x_n \quad \textit{for } \delta \to 0.$$

Proof. We use induction. Let $n \in \mathbb{N}$ be fixed. For $k = 0$ we have $I^\delta_0 = I_0 = \{0\}$ and

$$\begin{aligned} x^\delta_1 &= x_0 - t^\delta_{0,0} F'(x_0)^* \big(F(x_0) - y^\delta\big) \\ &= x_0 - \frac{\langle u^\delta_{0,0}, x_0 \rangle - \big(\alpha^\delta_{0,0} + \xi^\delta_{0,0}\big)}{\left\| u^\delta_{0,0} \right\|^2} F'(x_0)^* \big(F(x_0) - y^\delta\big), \end{aligned}$$

which depends continuously on the data y^δ (see also Definition 1.17) as the norm in Y is continuous and thus $x^\delta_1 \to x_1$ for $\delta \to 0$.
Let us now assume that x^δ_i, $i \le k$, depend continuously on y^δ. For x^δ_{k+1} we have

$$x^\delta_{k+1} = x^\delta_k - \sum_{i\in I_k} t^\delta_{k,i} F'(x^\delta_i)^* \left(F(x^\delta_i) - y^\delta\right).$$

Since F is continuously Fréchet differentiable on $\mathcal{D}(F)$, the inductive hypothesis implies that the search directions $F'(x^\delta_i)^* \left(F(x^\delta_i) - y^\delta\right)$, $i \in I^\delta_k$, depend continuously on y^δ. It remains to show that the same holds for the optimization parameters $t^\delta_{k,i}$. By Proposition 1.5, the corresponding convex function h (see (1.8)) is strictly convex as the search directions $u^\delta_{k,i}$, $i \in I^\delta_k$, are linearly independent. Consequently, the optimization parameters are uniquely determined by a regular linear system of equations, given by (1.9), whose coefficients depend continuously on y^δ, such that we have

$$t^\delta_{k,i} \to t_{k,i}$$

for $\delta \to 0$. This proves the induction step and we have

$$x^\delta_n \to x_n \quad \text{for } \delta \to 0.$$

□

Having this result at disposal we can now prove Theorem 1.31.

Proof. (of Theorem 1.31) We show that

$$\left\|F\big(x^{\delta}_{n_*(\delta)}\big) - y\right\| \to 0 \tag{1.59}$$

if the noise level δ tends to 0. For that purpose, let $\{\delta_j\}_{j\in\mathbb{N}}$, $\delta_j > 0$ for all $j \in \mathbb{N}$, be a null sequence, such that

$$\left\|y^{\delta_j} - y\right\| \leq \delta_j \tag{1.60}$$

for all $j \in \mathbb{N}$. For each noise level δ_j, let $n_*(\delta_j)$ denote the corresponding stopping index.
Proposition 1.25 and Lemma 1.29 yield $x_n^{\delta_j} \in B_\rho(x_0)$ for a fixed index $n \in \mathbb{N}$ and all $j \in \mathbb{N}$. Hence, the sequence $\left\{x^{\delta_j}_{n_*(\delta_j)}\right\}_{j\in\mathbb{N}}$ is bounded and possesses a weakly convergent subsequence. Let us consider the sequence $\{n_*(\delta_j)\}_{j\in\mathbb{N}}$ and assume that $n \in \mathbb{N}$ is a finite accumulation point of this sequence. As in the proof of Theorem 2.4 in [39], we assume without loss of generality that $n_*(\delta_j) = n$ for all $j \in \mathbb{N}$. We thus have

$$\left\|F\big(x_n^{\delta_j}\big) - y^{\delta_j}\right\| \leq \tau\delta_j \tag{1.61}$$

for all $j \in \mathbb{N}$. Since we have fixed the index n, the iterate $x_n^{\delta_j}$ depends continuously on y^{δ_j} according to Lemma 1.32, yielding

$$x_n^{\delta_j} \to x_n \quad \text{and} \quad F\big(x_n^{\delta_j}\big) \to F(x_n)$$

for $j \to \infty$. As a result, we infer $F(x_n) = y$ from (1.61). Since $x_n \in B_\rho(x_0)$ and x^+ is the only solution of (1.28) in $B_\rho(x_0)$, we have

$$\left\|F\left(x^{\delta_j}_{n_*(\delta_j)}\right) - y\right\| \leq \left\|F\left(x^{\delta_j}_{n_*(\delta_j)}\right) - y^{\delta_j}\right\| + \left\|y^{\delta_j} - y\right\| \leq (\tau+1)\delta_j \;\to 0$$

and

$$x^{\delta_j}_{n_*(\delta_j)} \to x^+$$

for $j \to \infty$ due to the weak sequential closedness of F.
Let us now assume $n_*(\delta_j) \to \infty$ for $j \to \infty$. From Theorem 1.27 and its proof we recall that the sequence $\{\|x_n - x^+\|\}_{n\in\mathbb{N}}$ is a bounded and monotonically decreasing sequence with limit 0. Consequently, for every $\varepsilon > 0$ there exists an $N_0 \in \mathbb{N}$ such that

$$\|x_{N_0} - x^+\|^2 < \frac{\varepsilon}{2}.$$

Furthermore, there is a $j_0 \in \mathbb{N}$ such that, due to the continuity of the norm, we have

$$\left|\|x^{\delta_j}_{N_0} - x^+\|^2 - \|x_{N_0} - x^+\|^2\right| < \frac{\varepsilon}{2} \quad \text{for all } j \geq j_0 \tag{1.62}$$

on the one hand and also, according to our assumption,

$$n_*(\delta_j) \geq N_0 \quad \text{for all } j \geq j_0$$

on the other hand. We thus have (using Lemma 1.29)

$$\|x^{\delta_j}_{n_*(\delta_j)} - x^+\|^2 \leq \|x^{\delta_j}_{N_0} - x^+\|^2 \leq \|x_{N_0} - x^+\|^2 + \left|\|x^{\delta_j}_{N_0} - x^+\|^2 - \|x_{N_0} - x^+\|^2\right| < \varepsilon$$

for all $j > j_0$, which completes the proof. □

From these results, we directly deduce the following corollary concerning the special case of Algorithm 1.21.

Corollary 1.33. *Theorem 1.31 is valid for Algorithm 1.21, where the explicit representation of the optimization parameters (see A.2) directly shows the continuous dependence on the data* y^δ*. Also, in each step of Algorithm 1.21, the two search directions are either linearly independent or the algorithm proceeds to the next iteration after executing step (i).*

Proof. We make the choice $N = 2$ in (1.57) and apply Theorem 1.31. Due to (1.50), the projection of x_n^δ onto H_n^δ is also contained in H_{n-1}^δ if the directions u_{n-1}^δ and u_n^δ are linearly dependent. Consequently, at iteration $n \in \mathbb{N}$, the two search directions are either linearly independent or the previous search direction u_{n-1}^δ is not used, i.e., step (ii) is not executed, as $H\big(u_n^\delta, \alpha_n^\delta + \xi_n^\delta\big) \subseteq H_{n-1}^\delta$. □

Remark 1.34. *We conclude our analysis with some final remarks.*

(a) The choice $U_n := \{g_n\}$ *for all* $n \in \mathbb{N}$ *yields a Landweber type method, where the current iterate is projected onto a stripe corresponding to the conventional Landweber direction in each iteration, for which we can apply our results from above. We thus obtain a regulation of the step width. This method has been presented by Maaß and Strehlow in [54] for finite dimensional Banach spaces.*

(b) One of the major obstacles in practice is the determination of the constant c_{tc} *from the tangential cone condition. This parameter obviously influences the algorithms significantly and yet, for many operators, even the existence of* c_{tc} *can not be determined and its value might depend on the point of linearization. In any case, a bad choice either yields a diverging algorithm if* c_{tc} *is chosen too small or useless results if* c_{tc} *is too large, as the discrepancy principle is fulfilled too early. It is thus reasonable to find an adequate value numerically, for example systematically with the help of a grid search. The results may give a hint about the existence and value of* c_{tc} *for a given nonlinear operator.*

1.4. A first numerical example

Finally, we want to evaluate the proposed methods in terms of Algorithm 1.21 by applying it to a well-understood nonlinear problem and compare the performance to a standard Landweber method, see [39, 49]. Additionally, we apply the Landweber type method that is derived from the subspace optimization techniques, see Remark 1.34 (a), and also discuss its performance. The parameter identification problem we are considering has been used many times for similar purposes, first in [17] as a one-dimensional problem and for example in [39, 63] in two dimensions. We begin with a short summary of this inverse problem.

Let $\Omega \subseteq \mathbb{R}^2$ be a bounded domain that is either a parallelepiped (e.g., $\Omega = (0,1) \times (0,1)$) or has a sufficiently smooth boundary. We want to reconstruct the parameter $c \in L^2(\Omega)$ from the knowledge of the (noisy) field u, where

$$\begin{aligned} -\Delta u + cu &= f \qquad \text{in } \Omega, \\ u &= g \quad \text{ on } \partial\Omega, \end{aligned} \tag{1.63}$$

for given functions $f \in L^2(\Omega)$ and $g \in H^{3/2}(\partial\Omega)$ (for a definition of this space, see, e.g., [27, 64]). Let $F : \mathcal{D}(F) \subseteq L^2(\Omega) \to L^2(\Omega)$ be the parameter-to-solution mapping satisfying

$$F(c) = u, \tag{1.64}$$

where u fulfills the elliptic boundary value problem (1.63). As stated in [17, 39], there exists a $\gamma > 0$ such that F is well-defined on

$$\mathcal{D}(F) := \left\{c \in L^2(\Omega) \,:\, \|c - \hat{c}\| \leq \gamma \text{ for a } \hat{c} \in L^2(\Omega) \text{ with } \hat{c} \geq 0 \text{ a.e.}\right\}.$$

We define the operator $L(c) : H^2(\Omega) \cap H_0^1(\Omega) \to L^2(\Omega)$ by

$$L(c)u = -\Delta u + cu. \tag{1.65}$$

Also, F is Fréchet differentiable in $c \in B_\rho(c_0) \subseteq \mathcal{D}(F)$, where $\rho \leq \gamma$, and $c_0 \in \mathcal{D}(F)$. The Fréchet derivative $F'(c)$ in c and its adjoint $F'(c)^*$ are given by

$$F'(c)v = -L(c)^{-1}(v \cdot u) \tag{1.66}$$

and

$$F'(c)^* w = -u \cdot L(c)^{-1} w \tag{1.67}$$

for $v, w \in L^2(\Omega)$, see [39].
In case u has no zeros in Ω, the parameter c is uniquely determined by

$$c = \frac{\Delta u + f}{u},$$

but it does not depend continuously on u. Therefore, the above formula is not useful for the reconstruction of c from noisy data.

1.4.1. Discretization

As in [63], we choose $\Omega = (0,1) \times (0,1)$ and use finite differences for the discretization, see for example [3, 34] for the basics. We define the grid

$$\overline{\Omega}_h := \left\{(x_i, y_j) \in \overline{\Omega} \,:\, x_i = ih, y_j = jh,\, 0 \leq i, j \leq N+1\right\},$$

where $N+1$ is the number of equidistant steps in x- and in y-direction and

$$h := \frac{1}{N+1}$$

is the respective step width. The (discretized) interior Ω_h of $\overline{\Omega}_h$ is thus given by

$$\Omega_h := \{(x_i, y_j) \in \Omega_h \,:\, x_i = ih, y_j = jh,\, 1 \leq i, j \leq N\}.$$

By u_h, c_h, f_h and g_h we denote the respective discretized functions on the grid Ω_h and on the discretized boundary $\partial\Omega_h := \overline{\Omega}_h \setminus \Omega_h$. The Laplace operator Δ is discretized as usually, see for instance [3, 34], by a two-dimensional difference quotient. Let Δ_h denote the discretized Laplace operator. Then we have

$$\begin{aligned}\Delta_h u_h(ih, jh) = \frac{1}{h^2}\Big(&u_h\big((i-1)h, jh\big) + u_h\big(ih, (j-1)h\big)\\ &+ u_h\big((i+1)h, jh\big) + u_h\big(ih, (j+1)h\big) - 4u_h\big(ih, jh\big)\Big)\end{aligned} \tag{1.68}$$

for all $1 \leq i, j \leq N$. The grid points $\big((i-1)h, jh\big)$, $\big(ih, (j-1)h\big)$, $\big((i+1)h, jh\big)$, and $\big(ih, (j+1)h\big)$ are called the *nearest neighbors* of the point $\big(ih, jh\big)$.

At this point, it is important to remark that the boundary values of u_h contribute to the above expression, if the Laplace operator is evaluated in a grid point that has boundary points as nearest neighbors.

We represent the discretized function u_h by a vector with $(N+2)^2$ components,

$$(u_h)_{l(i,j)} = u_h(x_i, y_j), \tag{1.69}$$

where $l(i,j) = i \cdot (N+1) + j$ for $0 \leq i, j \leq N+1$, such that the indices are ordered lexicographically. Analogously, we obtain the vector c_h. This allows us to reformulate the discretized boundary value problem

$$\begin{aligned} -\Delta_h u_h + c_h u_h &= f_h \qquad \text{in } \Omega_h, \\ u_h &= g_h \qquad \text{on } \partial\Omega_h \end{aligned} \tag{1.70}$$

as a linear system of equations

$$M_h(c_h) \cdot u_h = f[g]_h \quad \text{in } \overline{\Omega}_h, \tag{1.71}$$

where $M_h(c_h) \in \mathbb{R}^{(N+2)^2 \times (N+2)^2}$. The information about the boundary values is included in the matrix M_h and in the vector $f[g]_h$.
As the boundary values are given, it is possible to reduce the above system of equations to an $N^2 \times N^2$ system by separating the boundary values into a vector and shifting it to the right-hand side of (1.71). As a result, we obtain the reduced system of equations

$$\tilde{M}_h(c_h) \cdot \tilde{u}_h = \tilde{f}_h \quad \text{in } \Omega_h, \tag{1.72}$$

where $(\tilde{u}_h)_{k(i,j)} = (\tilde{u}_h)_{(i-1)\cdot N + j}$ and $\tilde{M}_h(c_h) \in \mathbb{R}^{N^2 \times N^2}$. In case $g = 0$, we have $\tilde{f}_h = f_h$.

The matrix that corresponds to the discretized Laplace operator $-\Delta_h$ now has a simple block structure: Define the tridiagonal matrix

$$\mathcal{A} := \begin{pmatrix} 4 & -1 & 0 & \cdots & 0 \\ -1 & \ddots & \ddots & \ddots & \vdots \\ 0 & \ddots & \ddots & \ddots & 0 \\ \vdots & \ddots & \ddots & \ddots & -1 \\ 0 & \cdots & 0 & -1 & 4 \end{pmatrix} \in \mathbb{R}^{N \times N}$$

and $\mathcal{B} := -I_N$, where I_N is the N-dimensional unit matrix. Then $-\Delta_h$ has the form

$$-\Delta_h = \begin{pmatrix} \mathcal{A} & \mathcal{B} & & \\ \mathcal{B} & \ddots & \ddots & \\ & \ddots & \ddots & \mathcal{B} \\ & & \mathcal{B} & \mathcal{A} \end{pmatrix} \in \mathbb{R}^{N^2 \times N^2}. \tag{1.73}$$

For the reduced matrix $\tilde{M}_h(c_h)$ we obtain

$$\tilde{M}_h(c_h) = -\Delta_h + \operatorname{diag}(c_h) \in \mathbb{R}^{N^2 \times N^2}. \tag{1.74}$$

The norm on Ω_h is given by the weighted Euklidian norm

$$\left\| (v_l)_{1 \leq l \leq N^2} \right\|_h = h \cdot \left(\sum_{l=1}^{N^2} (v_l)^2 \right)^{1/2} = h \cdot \left(\sum_{i,j=1}^{N} \big(v(ih, jh)\big)^2 \right)^{1/2}, \tag{1.75}$$

which approximates the standard L^2-norm on the equidistant grid Ω_h with step width $h = \frac{1}{N+1}$.

We are interested in the numerical solution of the parameter identification problem that corresponds to (1.63), where the parameter c is reconstructed from the knowledge of the noisy function u^δ, the exact function f and boundary values g, for which we make use of the above discretization.

1.4.2. Reconstructions with Landweber and RESESOP

In order to have a precise representation of the exact solution u and the parameter c of (1.63), we provide u and c analytically, such that f and the boundary values g are uniquely determined by

$$f = -\Delta u + cu, \quad g = u|_{\partial\Omega}. \tag{1.76}$$

Let

$$u : \overline{\Omega} \to \mathbb{R}, \; u(x, y) = 16x(x-1)y(1-y) + 1$$

and

$$c : \overline{\Omega} \to \mathbb{R}, \; c(x, y) = \frac{3}{2}\sin(2\pi x)\sin(3\pi y) + 3\left(\left(x - \frac{1}{2}\right)^2 + \left(y - \frac{1}{2}\right)^2\right) + 2.$$

We have $u_h(ih, jh) = u(ih, jh)$ for all indices $0 \le i, j \le N+1$ and $g_h(ih, jh) = u_h(ih, jh) \equiv 1$ for all $(ih, jh) \in \partial\Omega_h$. In our iterations, we will use the function

$$c_0 : \overline{\Omega} \to \mathbb{R}, \; c_0(x, y) = 3\big((x-0.5)^2 + (y-0.5)^2\big) + 2 + 8x(x-1)y(1-y)$$

as an initial value. This choice allows us to make use of the reduced matrix $\tilde{M}_h$ to determine $\tilde{f}_h$ and to calculate the search directions during the iteration: The initial value c_0 coincides with the exact values of c on the boundary. An iteration that is based on the reduced system of equations, working only on the inner grid points, does not change the boundary values. Consequently, we set

$$\tilde{f}_h := \tilde{M}_h \cdot u_h, \tag{1.77}$$

where $u_h = (u_h)_{l(i,j)}$ for $1 \le i, j \le N$.

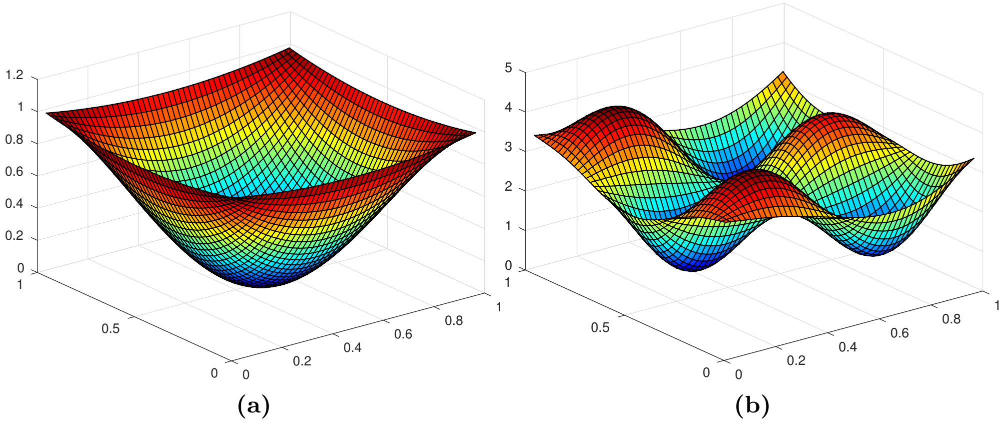

Figure 1.3.: Surface plot of (a) exact function u_h and (b) exact parameter c_h on the grid Ω_h.

For our reconstructions, we use synthetic noisy data u_h^δ, which is obtained by adding a noise vector v to the exact data vector u_h. To this end, we generate a vector with random, equally distributed entries $v_l \in [-1,1]$ for all $l = 1, ..., N^2$ and set

$$u_h^\delta = u_h + \delta \cdot \frac{v}{\|v\|_h}, \tag{1.78}$$

which ensures that $\left\|u_h^\delta - u_h\right\|_h = \delta$.

The reconstructions are performed iteratively by

$$c_{k+1}^\delta = c_k^\delta - d_k^\delta,$$

where k is the iteration index, $\left\{c_k^\delta\right\}_{k\in\mathbb{N}}$ is the sequence of iterates and d_k^δ is calculated according to

(A) the standard Landweber method with a relaxation parameter ω, i.e., $d_k^\delta = \omega \cdot g_k^\delta$,

(B) a Landweber type iteration that is based on the successive projection onto stripes, i.e., Algorithm 1.19 with a single search direction (the current gradient g_k^δ) per iteration and

(C) the RESESOP method 1.21 with two search directions, the current gradient and the gradient from the previous step.

Method	Number of iterations k_*	Execution time	Relative error in reconstruction
(A)	287	123.65s	13.41%
(B)	11	7.1s	12.83%
(C)	8	5.71s	13.13%

Table 1.1.: Some key data to evaluate the performance of the methods (A), (B) and (C) in the case of noisy data u_h^δ

All iterations are stopped by the discrepancy principle, where $\tau > {}^{1+c_{\mathrm{tc}}}/_{1-c_{\mathrm{tc}}}$ is chosen according to Algorithms 1.19 and 1.21. For both methods, we set (see also [39, 54])

$$N = 49, \quad c_{\mathrm{tc}} = 0.01, \quad \tau = 1.005 \cdot \frac{1+c_{\mathrm{tc}}}{1-c_{\mathrm{tc}}}, \quad \delta = 0.005. \tag{1.79}$$

We denote the stopping index by $k = k_*$, which is the first iteration index that fulfills $\|R_{k_*}\|_h \leq \tau\delta$.

The exact function u_h and the exact parameter c_h are plotted in Figure 1.3. In order to compare the methods, we measure the iteration steps until the iteration is stopped, the time that is needed for the reconstruction and the relative error in the resulting solution c_{k_*}. The results are presented in Table 1.1. Plots of the respective residuals are to be found in Figure 1.5.

Remark 1.35. *It is important to remark that the results concerning the three different methods, which are listed in Table 1.1, depend on the available data. Experiments show that the values we have measured to quantify the performance of the proposed methods vary slightly due to the random noise that is added to the exact value of* u_h *in order to obtain noisy data* u_h^δ*. However, the method with two search directions is in all experiments faster than the method with one search direction. The Landweber method is significantly slower than the other methods, as there is no regulation of the step widths in the iterations in contrast to the RESESOP methods.*

Also, we remark that the above methods yield, in the case of exact data, sequences of iterates that converge to the exact solution u_h. We make use of exact data to further test the performance of

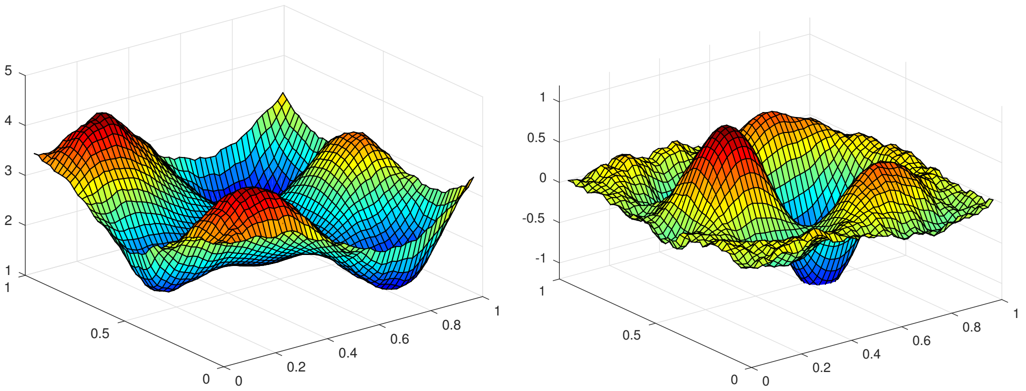

(a) Reconstruction of c_h, method (A) **(b)** Error in reconstruction, method (A)

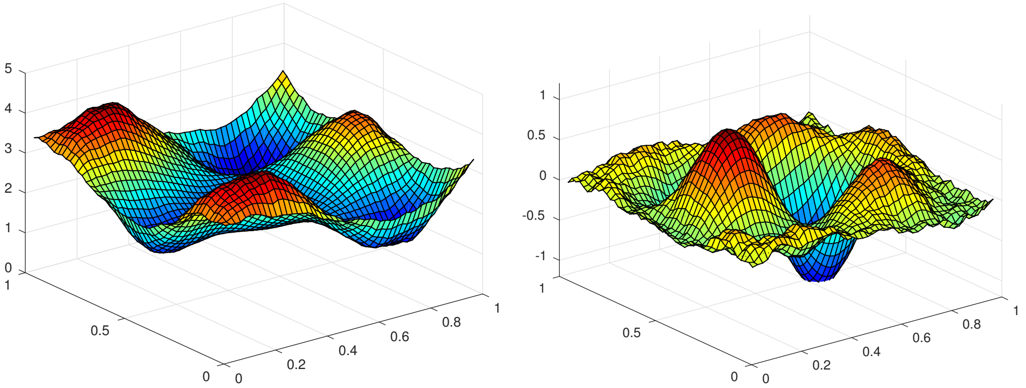

(c) Reconstruction of c_h, method (B) **(d)** Error in reconstruction, method (B)

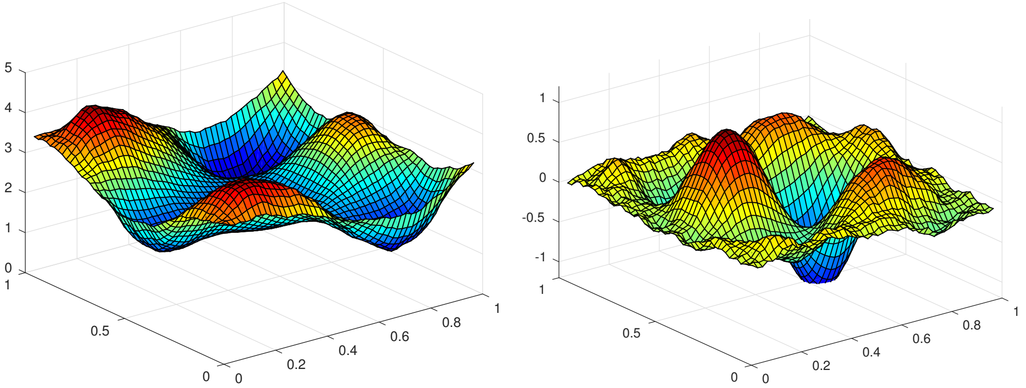

(e) Reconstruction of c_h, method (C) **(f)** Error in reconstruction, method (C)

Figure 1.4.: Reconstruction with the standard Landweber method (A), the Landweber type method (B) and the RESESOP method (C): surface plots of the respective reconstructed parameter c_{k_*} ((a), (c), (e)) and of the deviations from the exact solution c_h ((b), (d), (f)).

the SESOP method with two search directions in comparison to the other two methods. For that purpose, we set $T := 2 \cdot 10^{-4}$ and stop the iteration, when the residual R_k fulfills $\|R_k\|_h \leq T$. We use the same parameters as in the case of noisy data. Again, we measure the total number of iterations k_*, the time that is needed for the iteration and the relative error in the reconstruction.

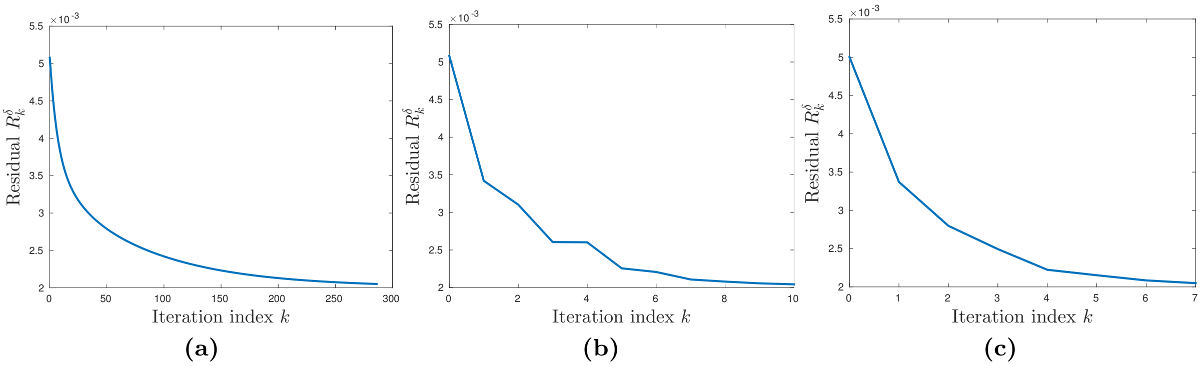

Figure 1.5.: Plots of the respective residuals $\|R_k^\delta\|_h = \|F(c_k^\delta) - u^\delta\|_h$ versus the iteration index k for (a) the Landweber method, (b) the RESESOP method with a single search direction and (c) the RESESOP method with two search directions

The results are summarized in Table 1.2.

The plots of the relative error

$$e_{\text{rel},k} := \frac{\|c_k - c_h\|_h}{\|c_h\|_h}$$

in the reconstruction and the norm of the residual $\|R_k\|_h$ are illustrated in Figure 1.6. Note that these plots indicate that the descent property (1.52) is fulfilled.

Method	Number of iterations k_*	Execution time	Relative error in reconstruction
(A)	742	306.18s	10.65%
(B)	44	21.03s	9.65%
(C)	23	12.03s	8.69%

Table 1.2.: Some key data to evaluate the performance of the methods (A), (B) and (C) in the case of exact data u_h

It is interesting to observe the difference between the two methods that are based on the findings in this chapter, i.e., the methods that are based on the successive projection onto stripes. First of all, method (B) with one search direction takes about twice the time that is required for the iteration with the RESESOP method (C). This is due to the fact that during the reconstruction with the RESESOP method, an iteration may consist of only one projection onto the stripe H_k given by the current gradient, which is the case if this projection is already contained in the stripe that belongs to the previous search direction. Let us denote this case by *Case 1*. The other two cases that may occur in the second step of Algorithm 1.21 are *Case 2*, where the projection is situated above the stripe that corresponds to the previous gradient, and *Case 3*, where the projection is situated below this stripe.
In our experiment, *Case 1* occurred four times, while *Case 2* occurred 17 times and *Case 3* occurred only once. In the case of noisy data, some further tests have suggested that a higher noise level leads to an increase of iterations in which *Case 1* occurs. This is plausible as a higher noise level directly leads to broader stripes. Also, this effect is observed when the constant c_{tc} from the tangential cone condition is chosen larger.

All in all, we have been able to demonstrate that the developed SESOP and RESESOP methods are suitable to solve nonlinear inverse problems. In the case of noisy data, the RESESOP method

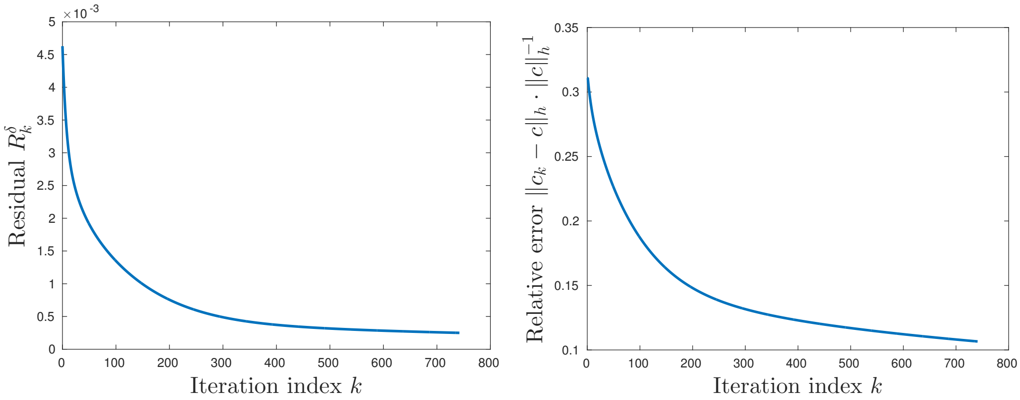

(a) Norm of residuals R_k, method (A) **(b)** Relative error in reconstruction, method (A)

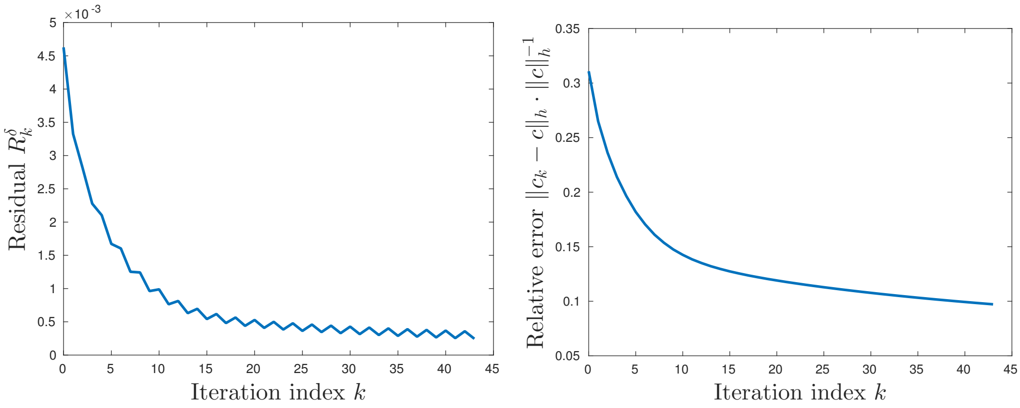

(c) Norm of residuals R_k, method (B) **(d)** Relative error in reconstruction, method (B)

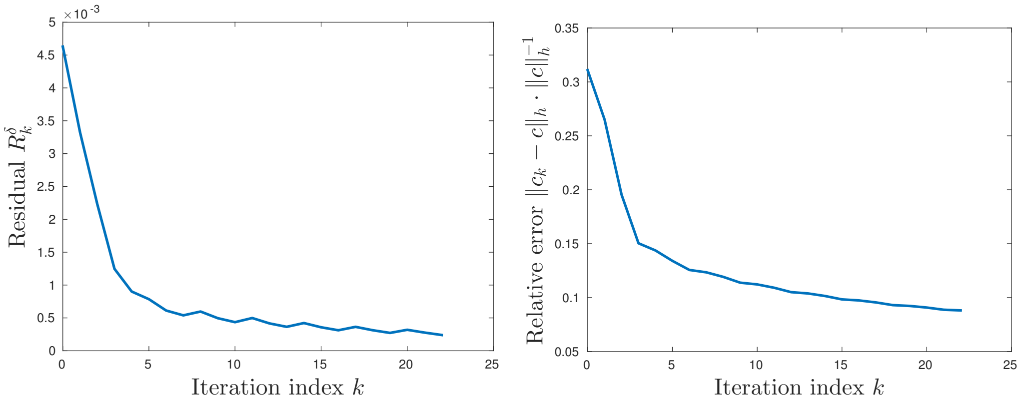

(e) Norm of residuals R_k, method (C) **(f)** Relative error in reconstruction, method (C)

Figure 1.6.: Plots of the behavior of the respective norm of the residuals and the relative errors during the iterations

yields a regularized solution. In both cases, our methods are significantly faster than the standard Landweber method, such that it is desirable to exploit this method for the solution of more complex inverse problems, such as the inverse problem of THz tomography.

1.4.3. A first outlook

The results of this chapter are valid for real Hilbert spaces, which is a suitable setting for many nonlinear inverse problems such as the inverse medium problem [6, 7] or the three inverse problems that Haltmeier et al. have analyzed in [36] regarding their Landweber-Kaczmarz methods for solving systems of ill-posed operator equations [37].
However, the subspace methods we presented so far rely on the total order of the ground field of the Hilbert space we are working in: In order to decide how to project an element of X onto the intersection of hyperplanes, the ground field of the Hilbert space X needs to be totally ordered. This becomes obvious when we look at the SESOP method with two search directions. In the second step, we have to decide whether the iterate $\tilde{x}_{n+1}$ is inside, above or below the stripe that belongs to the former search direction. For this, we need the ground field to be an ordered field.

The performance of our sequential subspace methods for nonlinear inverse problems suggests that an application in the solution of a more complex inverse problem may considerably speed up the reconstruction, which is of major importance in industrial applications. A relatively novel application in imaging is THz tomography, which aims at the reconstruction of dielectric properties (i.e., the complex refractive index) from measurements of the electric field around the tested object. In complement to the work of Tepe et al. [51, 71], we formulate and analyze the inverse problem in THz tomography in the following chapter, where we choose an approach that is motivated by lower-frequency methods such as microwave tomography and scattering problems. In short, the inverse problem we will deal with is a nonlinear parameter identification problem in complex Hilbert spaces, such that we have to refine our (RE)SESOP methods to meet the requirements for an application in complex Hilbert spaces, which is the topic of Chapter 3.

2. Terahertz tomography

The overall goal in terahertz (THz) tomography is the nondestructive testing of objects that consist of dielectric materials, especially plastics. The corresponding physical quantity that contains information about defects such as cracks or impurities is the complex refractive index $\tilde{n}$, which allows conclusions about the dielectric permittivity ϵ and therefore about the refractive index n as well as the absorption coefficient α.
The inverse problem of THz tomography is thus the reconstruction of the complex refractive index from measurements of the electric field of the THz beam, which interacts with the tested object in a way that is described by the model we derive in this chapter.
THz radiation is particularly suited for the testing of plastics and ceramics, as these materials are nearly opaque to electromagnetic waves in this frequency range, leading to a high penetration depth. This property is reflected in the relatively low values of the absorption coefficient.

We will start with an introduction into the fundamental physics that are required for the modeling of the direct problem in THz tomography. Due to its frequency of around 0.1 to 10 THz (or 10^{11} to 10^{13} Hz), THz radiation is located between microwave and infrared radiation in the electromagnetic spectrum. Accordingly, it is sometimes referred to as submillimeter waves. In comparison to X-radiation, which is used in computerized tomography, the frequency of THz radiation is significantly smaller. The propagation of THz beams in the lower frequency range of the THz spectrum through media is thus comparable to the propagation of microwaves rather that X-rays. Physical effects such as refraction or reflection cannot be neglected and need to be taken into account in the modeling. In particular, THz waves are not propagating along straight lines, such that the modeling differs from the modeling in computerized tomography. As we have remarked before, we will focus on radiation with a frequency in the limits of microwave (roughly $3 \cdot 10^8$ to $3 \cdot 10^{11}$Hz) and THz radiation, which motivates our approach from scattering theory.

In the following, we present the physical basics for the modeling and an analysis of the direct problem. In particular, we derive all necessary tools for a numerical solution of the inverse problem with a Landweber iteration and, in the subsequent chapter, with the sequential subspace optimization methods we introduced before.

We remark that we make use of the *analytic representation* of the occurring electromagnetic fields, such that these quantities are regarded as complex valued functions. This is a well-established tool in the theory of electromagnetic waves, which allows a simpler mathematical handling of the fields.

2.1. Propagation of electromagnetic waves

Electromagnetic waves consist of interacting, usually time-dependent electric and magnetic three-dimensional vector fields. The electric field at time t in position $\mathbf{x} \in \mathbb{R}^3$ is denoted by $\mathbf{E}(t, \mathbf{x})$ and the induction field by $\mathbf{B}(t, \mathbf{x})$. The electric field $\mathbf{E}$ is associated with the electric displacement field

D via

$$\mathbf{D}(t,\mathbf{x}) = \epsilon \mathbf{E}(t,\mathbf{x})$$

and the induction field **B** via

$$\mathbf{B}(t,\mathbf{x}) = \mu \mathbf{H}(t,\mathbf{x})$$

with the magnetic field **H**. The parameter $\epsilon(\mathbf{x})$ depends on the position $\mathbf{x}$ and is called the *dielectric permittivity*. It describes the dielectric properties of a medium. Similarly, the *magnetic permeability* $\mu(\mathbf{x})$ describes the magnetic properties. In anisotropic media, both functions are second rank tensors. In isotropic media, both functions are reduced to scalars.

2.1.1. Maxwell's equations

The propagation of electromagnetic waves in space is generally described by Maxwell's equations. They consist of four partial differential equations (Gauss's law for magnetism (2.1), Faraday's law of induction (2.2), Gauss's law (2.3), and Ampère's circuital law (2.4)) and provide, together with the Lorentz force law, the basis of electromagnetism. In the local formulation, they read

$$\nabla \cdot \mathbf{B}(t,\mathbf{x}) = 0, \tag{2.1}$$

$$\nabla \times \mathbf{E}(t,\mathbf{x}) = -\frac{\partial}{\partial t}\mathbf{B}(t,\mathbf{x}), \tag{2.2}$$

$$\nabla \cdot \mathbf{D}(t,\mathbf{x}) = \rho(t,\mathbf{x}), \tag{2.3}$$

$$\nabla \times \mathbf{H}(t,\mathbf{x}) = \frac{\partial}{\partial t}\mathbf{D}(t,\mathbf{x}) + \mathbf{j}(t,\mathbf{x}). \tag{2.4}$$

The quantity ρ in Gauss's law (2.3) is the *electric charge density* and $\mathbf{j}$ in Ampère's circuital law (2.4) is called the *electric current density*. The differential operator $\nabla := \left(\frac{\partial}{\partial x}, \frac{\partial}{\partial y}, \frac{\partial}{\partial z}\right)^T$ is called the *Nabla operator* and is denoted as a vector whose entries are the first partial derivatives with respect to the (cartesian) coordinates. (Note that the above notation has been adopted from physics, where it is common to denote the inner product in $\mathbb{R}^3$ by the dot $\cdot$ and the vector product by $\times$.)

For our purposes, we assume that the media we are dealing with are isotropic and not magnetic, i.e., we have $\mu = \mu_0$, where μ_0 is the permeability of free space, and $\epsilon(\mathbf{x}) = \epsilon_0 \epsilon_r(\mathbf{x})$ is a scalar function, where ϵ_0 is the permittivity of free space and ϵ_r is the relative permittivity. Furthermore we assume that the value of ϵ does not vary strongly, such that we can neglect terms containing $\nabla\epsilon$, i.e., we assume that

$$\nabla \cdot (\epsilon(\mathbf{x})\mathbf{E}(\mathbf{x})) \approx \epsilon(\mathbf{x}) \nabla \cdot \mathbf{E}(\mathbf{x})$$

holds almost everywhere (this corresponds to the limit of geometrical optics, see also [60]). We can thus restrict ourselves to the use of the fields **E** and **B** and obtain

$$\nabla \cdot \mathbf{B}(t,\mathbf{x}) = 0, \tag{2.5}$$

$$\nabla \times \mathbf{E}(t,\mathbf{x}) = -\frac{\partial}{\partial t}\mathbf{B}(t,\mathbf{x}), \tag{2.6}$$

$$\nabla \cdot \mathbf{E}(t,\mathbf{x}) = \frac{1}{\epsilon(\mathbf{x})} \cdot \rho(t,\mathbf{x}), \tag{2.7}$$

$$\nabla \times \mathbf{B}(t,\mathbf{x}) = \epsilon(\mathbf{x})\mu_0 \frac{\partial}{\partial t}\mathbf{E}(t,\mathbf{x}) + \mu_0 \mathbf{j}(t,\mathbf{x}). \tag{2.8}$$

For specific physical settings, we can derive further partial differential equations that describe the propagation of electromagnetic radiation in the respective special situation. One example is the *wave equation*.

2.1.2. The wave equation

Let us assume there are no electric sources, such that we have no charge density and no current density,

$$\rho(t, \mathbf{x}) \equiv 0, \quad \mathbf{j}(t, \mathbf{x}) \equiv 0.$$

We make use of the *Laplace operator* $\Delta := \frac{\partial^2}{\partial x^2} + \frac{\partial^2}{\partial y^2} + \frac{\partial^2}{\partial z^2}$ and apply the curl to equation (2.6). Together with the identity

$$\nabla \times (\nabla \times \mathbf{A}) = \nabla (\nabla \cdot \mathbf{A}) - \Delta \mathbf{A}$$

for three-dimensional vector fields $\mathbf{A}$, Gauss's law (2.7), and Ampère's law (2.8) we obtain the *wave equation*

$$\Delta \mathbf{E}(t, \mathbf{x}) - \epsilon(\mathbf{x}) \mu_0 \frac{\partial^2}{\partial t^2} \mathbf{E}(t, \mathbf{x}) = 0 \tag{2.9}$$

for the electric field $\mathbf{E}$. Analogously, we can derive a wave equation describing the induction field $\mathbf{B}$.

In vacuum, where we have $\epsilon(\mathbf{x}) \equiv \epsilon_0$, the wave equation is

$$\Delta \mathbf{E}(t, \mathbf{x}) - \frac{1}{c^2} \frac{\partial^2}{\partial t^2} \mathbf{E}(t, \mathbf{x}) = 0,$$

where $c = \sqrt{\epsilon_0 \mu_0}^{-1}$ is the speed of light in free space.

Obviously, the wave equation describes the temporal behavior of the electric field $\mathbf{E}$. In the case of time-harmonic waves, we can further simplify the wave equation (2.9), obtaining the time-independent *Helmholtz equation.*

2.1.3. The Helmholtz equation

A time-harmonic wave $\mathbf{E}(t, \mathbf{x})$ can be separated into a factor that depends on the position $\mathbf{x}$ and a factor that is a harmonic function of the time t, i.e., we can apply a separation of variables of the form

$$\mathbf{E}(t, \mathbf{x}) = \mathbf{u}(\mathbf{x}) e^{i\omega t}, \tag{2.10}$$

where ω is the frequency of the wave. The second partial derivative with respect to the time t is

$$\frac{\partial^2}{\partial t^2} \mathbf{E}(t, \mathbf{x}) = -\omega^2 \mathbf{E}(t, \mathbf{x}).$$

Inserting this into the wave equation (2.9), we obtain

$$(\Delta \mathbf{u}(\mathbf{x})) e^{i\omega t} + \omega^2 \epsilon(\mathbf{x}) \mu_0 \mathbf{u}(\mathbf{x}) e^{i\omega t} = 0.$$

We have thus derived the *Helmholtz equation*

$$\Delta \mathbf{u}(\mathbf{x}) + \tilde{k}^2 \mathbf{u}(\mathbf{x}) = 0 \tag{2.11}$$

with the wave number $\tilde{k}$, which fulfills

$$\tilde{k}^2(\mathbf{x}) = \omega^2 \epsilon(\mathbf{x}) \mu_0. \tag{2.12}$$

Remark 2.1. *A very simple solution of the Helmholtz equation* (2.11) *is the planar wave*

$$\mathbf{u}(\mathbf{x}) = \mathbf{a} e^{i\tilde{k}\mathbf{k} \cdot \mathbf{x}}, \tag{2.13}$$

where $\mathbf{a}$ *is a constant amplitude and* $\mathbf{k}$ *is the normalized wave vector.*

2.1.4. Absorbing, isotropic media and the complex refractive index

As already mentioned at the beginning of this chapter, the materials we are dealing with are absorbing. A wave propagating through an absorbing medium loses energy, which corresponds to a loss in intensity. This loss is taken into account by using a complex electric permittivity $\tilde{\epsilon}(\mathbf{x}) = \epsilon_1(\mathbf{x}) + i\epsilon_2(\mathbf{x})$. We write

$$\tilde{k} = k_0\tilde{n},$$

where k_0 is the wave number of the radiation in vacuum and $\tilde{n}$ is the complex refractive index. We have

$$\tilde{n}(\mathbf{x}) = \left(\frac{\epsilon_1(\mathbf{x}) + i\epsilon_2(\mathbf{x})}{\epsilon_0}\right)^{1/2} = n(\mathbf{x}) + i\kappa(\mathbf{x}).$$

The real part n is the *refractive index*, i.e., the ratio of the propagation speed c_0 in vacuum and the propagation speed c inside the medium. The imaginary part κ is called the *extinction coefficient* and is linked to the *absorption coefficient* α via

$$\kappa = \frac{k_0 c_0}{4\pi}\alpha \tag{2.14}$$

(see [21], Chapter 8.2).

Remark 2.2. *By setting $\tilde{k} = k_0\tilde{n}$ in the planar wave in Remark 2.1, we obtain*

$$\mathbf{u}(\mathbf{x}) = \mathbf{a}e^{ik_0(n+i\kappa)\mathbf{k}\cdot\mathbf{x}} = \mathbf{a}e^{ink_0\mathbf{k}\cdot\mathbf{x}} \cdot e^{-k_0\kappa\mathbf{k}\cdot\mathbf{x}}.$$

The imaginary part κ of the complex refractive index is contained in the term $e^{-k_0\kappa\mathbf{k}\cdot\mathbf{x}}$, which is monotonically decreasing in the direction of the wave vector $\mathbf{k}$ and causes the attenuation of the amplitude.

Depending on the type of data that is to be used in THz tomography, the THz beam is either a short electromagnetic pulse or a time-harmonic wave. Pulses allow conclusions on the run-time of the radiation through the tested medium, whereas the testing with a time-harmonic wave is mostly used to measure transmittivities or intensities of the electromagnetic field. In this work, we will restrict ourselves to the use of time-harmonic fields. Consequently, the propagation of THz radiation through plastics or ceramics can be described by the Helmholtz equation

$$\Delta\mathbf{u} + k_0^2\tilde{n}^2\mathbf{u} = 0. \tag{2.15}$$

It is well suited for our purposes, as the complex refractive index appears in a coefficient of this linear partial differential equation. The inverse problem in THz tomography belongs therefore to the class of *parameter identification problems.*

The Helmholtz equation (2.15) is an adequate choice for the modeling of the propagation of THz radiation, describing reflection and refraction of the waves on interfaces as well as the absorption of the beam when it travels through the medium. Another important principle that we use for the model is the superposition principle, which allows us to neglect source terms in our calculations.

2.1.5. The superposition principle

The shape or geometry of an electromagnetic wave that propagates through space is determined by the properties of the incident wave, which can be interpreted as the source, and the scattered field, which results in the interaction of the wave with the obstacles. According to the *superposition principle*, the total electromagnetic field $\mathbf{u}_\mathrm{t}$ is a superposition of the incident field $\mathbf{u}_\mathrm{i}$ and the scattered field $\mathbf{u}_\mathrm{sc}$. This means that the total field can be expressed as the sum

$$\mathbf{u}_\mathrm{t} = \mathbf{u}_\mathrm{i} + \mathbf{u}_\mathrm{sc}. \tag{2.16}$$

This is a very important statement, as it allows us to treat our problem as described in this chapter: Assuming the incident field is given, there is no additional source of electromagnetic radiation, yielding $\rho = 0$ and $\mathbf{j} = 0$ in Maxwell's equations. As we are using time-harmonic waves, the total field is described by the Helmholtz equation (2.15).
However, the superposition principle applies only approximately when the medium is a weak absorber, which is the case for the objects we are interested in.

2.1.6. The inhomogeneous Helmholtz equation for the scattered field

The total field $\mathbf{u}_\mathrm{t}$ and consequently each of its components u fulfill the homogeneous Helmholtz equation (2.15). Applying the superposition principle, we obtain

$$\Delta(\mathbf{u}_\mathrm{i} + \mathbf{u}_\mathrm{sc}) + \tilde{k}^2 \left(\mathbf{u}_\mathrm{i} + \mathbf{u}_\mathrm{sc}\right) = 0.$$

We replace $\tilde{k}$ by its representation $\tilde{k} = k_0 \tilde{n}$ and use that the incident wave $\mathbf{u}_\mathrm{i}$ (approximately) solves the Helmholtz equation in vacuum,

$$\Delta \mathbf{u}_\mathrm{i} + k_0^2 \mathbf{u}_\mathrm{i} = 0.$$

A reformulation of the above equation yields

$$\begin{aligned} 0 &= \Delta \mathbf{u}_\mathrm{i} + k_0^2 \mathbf{u}_\mathrm{i} + k_0^2 \left(\tilde{n}^2 - 1\right) \mathbf{u}_\mathrm{i} + \Delta \mathbf{u}_\mathrm{sc} + k_0^2 \tilde{n}^2 \mathbf{u}_\mathrm{sc} \\ &= k_0^2 \left(\tilde{n}^2 - 1\right) \mathbf{u}_\mathrm{i} + \Delta \mathbf{u}_\mathrm{sc} + k_0^2 \tilde{n}^2 \mathbf{u}_\mathrm{sc}. \end{aligned}$$

In other words, the scattered field $\mathbf{u}_\mathrm{sc}$ is determined by the inhomogeneous Helmholtz equation

$$\Delta \mathbf{u}_\mathrm{sc} + k_0^2 \tilde{n}^2 \mathbf{u}_\mathrm{sc} = k_0^2 \left(1 - \tilde{n}^2\right) \mathbf{u}_\mathrm{i}. \tag{2.17}$$

Note that the right-hand side of (2.17) contains the spacial factor $1 - \tilde{n}^2$, which vanishes in vacuum and is nearly zero in air. In the context of THz tomographic testing, this function is zero outside the object and can therefore be interpreted mathematically as a function with compact support. Also, the well-known incident field $\mathbf{u}_\mathrm{i}$ now only appears on the right-hand side as an inhomogeneity, whereas the left-hand side only depends on the unknown scattered field $\mathbf{u}_\mathrm{sc}$.

This mathematical description makes it easy to take into account the rather complex geometry of the incident field. The THz beams used in THz tomography combine certain elements of ray and wave character. This is reflected in their description as a Gaussian beam.

2.2. Gaussian beams

The incident field used in THz tomography, the THz beam, usually has a preferred direction of propagation and a certain spacial width. We use this information to find a mathematical description of a THz beam. This section is mainly based on Section 4.5 from [66].

In vacuum, the beam propagates according to the Helmholtz equation (2.11), where we have $\tilde{k} = k_0$. Let us assume that the direction of propagation is the y-axis, such that each component u of the electric field $\mathbf{u}$ is given by

$$u(\mathbf{x}) = a(\mathbf{x})e^{ik_0 y}$$

with an amplitude $a(\mathbf{x})$. Our assumption motivates the following approximation: The change in the amplitude of the electric field in the direction of propagation is small compared to orders of the wave length, such that we can neglect the second partial derivative of a with respect to y, i.e., we assume that

$$\frac{\partial^2}{\partial y^2} a(\mathbf{x}) \approx 0.$$

This yields

$$\begin{aligned}
\frac{\partial^2}{\partial y^2} u(\mathbf{x}) &= \left(-k_0^2 a(\mathbf{x}) + 2ik_0 \frac{\partial}{\partial y} a(\mathbf{x}) + \frac{\partial^2}{\partial y^2} a(\mathbf{x})\right) e^{ik_0 y} \\
&\approx \left(-k_0^2 a(\mathbf{x}) + 2ik_0 \frac{\partial}{\partial y} a(\mathbf{x})\right) e^{ik_0 y} \\
&= -k_0^2 u(\mathbf{x}) + 2ik_0 \frac{\partial}{\partial y} u(\mathbf{x}) + 2k_0^2 u(\mathbf{x}) \\
&= 2ik_0 \frac{\partial}{\partial y} u(\mathbf{x}) + k_0^2 u(\mathbf{x}),
\end{aligned}$$

where we have used

$$\left(\frac{\partial}{\partial y} a(\mathbf{x})\right) e^{ik_0 y} = \frac{\partial}{\partial y} u(\mathbf{x}) - ik_0 u(\mathbf{x}).$$

Inserting this into the original Helmholtz equation (2.11), we obtain the *paraxial Helmholtz equation*

$$\left(\frac{\partial^2}{\partial x^2} + 2ik_0 \frac{\partial}{\partial y} + \frac{\partial^2}{\partial z^2} + 2k_0^2\right) u(\mathbf{x}) = 0. \tag{2.18}$$

The amplitude $a(\mathbf{x})$ consequently fulfills

$$\left(\frac{\partial^2}{\partial x^2} + 2ik_0 \frac{\partial}{\partial y} + \frac{\partial^2}{\partial z^2}\right) a(\mathbf{x}) = 0.$$

In cylindric coordinates, the above equation transforms to

$$\left(\frac{\partial^2}{\partial r^2} + \frac{1}{r}\frac{\partial}{\partial r} + 2ik_0 \frac{\partial}{\partial y}\right) a(r, y) = 0, \tag{2.19}$$

where $r = \sqrt{x^2 + z^2}$ is the radial component.

A solution of the paraxial Helmholtz equation (2.18) is obtained when the spacial variable $R := (x^2 + y^2 + z^2)^{1/2}$ of a spherical wave

$$u(r, y) = a\frac{1}{R} e^{ik_0 R}$$

with a constant amplitude $a \in \mathbb{C}$ is kept close to the optical axis, i.e., the y-axis. Using the approximation

$$R = y\sqrt{1 + \frac{r^2}{y^2}} \approx y + \frac{r^2}{2y}$$

for $|x| \ll |y|$ and $|z| \ll |y|$, we obtain an asymptotic solution

$$u_{\mathrm{P}}(\mathbf{x}) := a\frac{1}{y}e^{ik_0 y}e^{ik_0\frac{r^2}{2y}}$$

of the paraxial Helmholtz equation, which is invariant under translation of y. By shifting $y \to y - s$ for some $s \in \mathbb{C}$, we obtain additional solutions, of which the solution for $s := iy_0$, $y_0 \in \mathbb{R}$, is of special interest (the detailed derivation is to be found in [66]). This solution is called the Gaussian solution or *Gaussian beam.* The most prominent representation of a Gaussian beam centered in $y = 0$ is

$$u_{\mathrm{G}}(\mathbf{x}) = a_0\frac{W_0}{W(y)}\exp\left(-\frac{r^2}{W^2(y)}\right)\exp\left(i\frac{k_0 y - \phi(y) + k_0 r^2}{2R(y)}\right), \tag{2.20}$$

where we have the original amplitude a_0 at the origin, the *beam waist* $W_0 = W(0)$, the *Gouy phase* $\phi(y) = \arctan\left({}^{y}\!/\!{}_{y_0}\right)$ and $y_0 \in \mathbb{R}$. The factor

$$R(y) = y\left(1 + \frac{y_0^2}{y^2}\right)$$

defines the radius of curvature of the wavefronts. The function

$$W(y) = W_0\sqrt{1 + \frac{y^2}{y_0^2}}$$

is called the *spot size parameter* and represents the radius at which the field's amplitude a falls to e^{-1} of its value $a(0, y, 0)$ on the y-axis. For increasing values of y, the value of $W(y)$ increases, which demonstrates that the beam is widening when it propagates away from the focal plane $y = 0$. When $y \gg y_0$, the wavefronts of the Gaussian beam can be interpreted as the wavefronts of a spherical wave. For $y = 0$, the curvature of the wavefronts is zero and the area $-y_0 \leq y \leq y_0$, where the wavefronts are almost planar, is called the *Rayleigh zone.* Inside this zone, the Gaussian beam can be regarded as a planar wave with a finite width.

Note that u_{G} is continuously differentiable in $\mathbb{R}^3$.

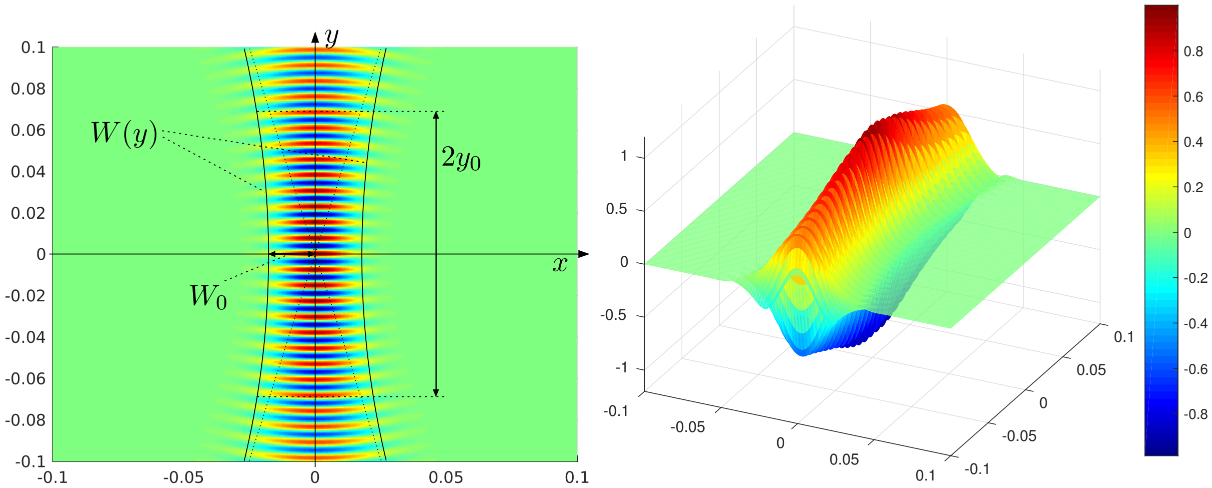

Figure 2.1.: Real part of the electromagnetic field (z-component) of a Gaussian beam with frequency $f = 4 \cdot 10^{10}$ Hz, beam waist $W_0 = 0.013$ m and a Rayleigh zone of length $2y_0 = 0.146$ m in the x-y-plane (left) and as a three-dimensional plot (right).

According to our assumption (2.10), the time-dependent electromagnetic Gaussian beam can be written as

$$E_z(t,\mathbf{x}) = u_{\mathrm{G}}(\mathbf{x}) \cdot e^{i\omega t}.$$

For further reading and a derivation of the above description of Gaussian beams, there is a wide range in literature, for example [66].

2.3. Boundary values for the Helmholtz equation

In the previous sections, we have derived a physical model for the propagation of THz radiation through a medium. In order to find a unique solution of the Helmholtz equation (2.11) or rather the inhomogeneous Helmholtz equation (2.17), we have to establish suitable boundary conditions. As long as the radiation is not absorbed or reflected at some finite boundary, we have to consider the whole space $\mathbb{R}^3$ or $\mathbb{R}^2$, depending on the setting, as a domain for the solution. In that case, the standard boundary condition that applies is the *Sommerfeld radiation condition*

$$\lim_{\varrho \to \infty} \varrho \left(\frac{\partial \mathbf{u}}{\partial \varrho} - ik_0 \mathbf{u} \right) = 0 \tag{2.21}$$

in $\mathbb{R}^3$ and

$$\lim_{\varrho \to \infty} \sqrt{\varrho} \left(\frac{\partial \mathbf{u}}{\partial \varrho} - ik_0 \mathbf{u} \right) = 0 \tag{2.22}$$

in $\mathbb{R}^2$, where we have used $\varrho = |\mathbf{x}|$.

The Helmholtz equation together with the Sommerfeld radiation condition is a well-known and established mathematical model for *scattering problems*. This boundary value problem has not only been applied in the scattering theory of electromagnetic waves. It is also fundamental in the scattering theory of acoustic waves (in particular ultrasound) and has been an important topic of research. The existence and uniqueness of a solution of the scattering problem (2.11), (2.21) is discussed in [20] and can be shown also for the two-dimensional case [6]. The proofs make use of the fundamental solution of the Helmholtz equation, which is why the proof in the two-dimensional case has to be modified due to the more complex shape of the fundamental solution in two dimensions.

For numerical purposes, the Sommerfeld radiation condition is of course not very useful, as the domains on which we need to calculate a solution of the Helmholtz equation are usually bounded. Our goal is to find boundary conditions that can be applied on the boundary of a bounded domain and approximate the Sommerfeld radiation condition well enough for our purposes.

One method to realize the radiation condition when dealing with bounded domains is the method of perfectly matched layers (see, e.g., [9], [80]). The basic idea is to add an additional layer around the domain and calculate the solution inside this layer such that there is no reflection of the field into the domain at the inner boundary.

Another option are the *Robin boundary conditions* or *first order scattering boundary conditions*

$$\frac{\partial \mathbf{u}}{\partial \mathbf{n}} - ik_0 \mathbf{u} = 0. \tag{2.23}$$

These boundary conditions approximate the Sommerfeld radiation condition and have been developed to minimize the back scattering of outgoing waves by the boundary of the domain. They

represent a condition on the normal derivative $\partial\mathbf{u}/\partial\mathbf{n}$ of the field $\mathbf{u}$. In the literature ([7], [64]) they are sometimes referred to as *generalized Neumann conditions*.
Both types of boundary conditions have been studied regarding their numerical implementation. A comparison can be found in the COMSOL blog [31].

Inspired by the work of Bao and Li, who analyzed the inverse medium problem [7, 8], which consists in the reconstruction of the refractive index n from the knowledge of the boundary data of the electric field influenced by the tested object, and in view of a solution of the inverse problem of THz tomography, the Robin boundary conditions turn out to be particularly useful. Their advantage concerns the calculation of the adjoint of the forward operator, as we will see in the following section. To avoid too strong back reflections from the boundary, which occur when the angle of incidence of the wave onto the boundary approaches $\pi/2$, we will choose the domain accordingly, i.e., large enough, such that the beam's angle of incidence with the boundary does not differ significantly from zero.

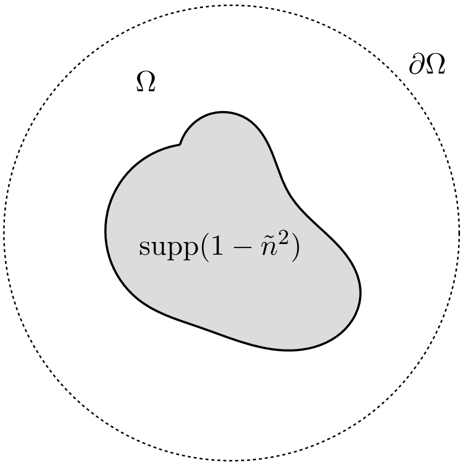

Figure 2.2.: Domain Ω with boundary $\partial\Omega$, containing the support of $1-\tilde{n}^2$.

Summing up the results of this chapter so far, the first part of the direct problem in THz tomography is given by the following boundary value problem. On a finite domain Ω with C^1-boundary $\partial\Omega$ we want to solve the scattering problem

$$\begin{aligned} \Delta\mathbf{u}_{\mathrm{sc}} + k_0^2\tilde{n}^2\mathbf{u}_{\mathrm{sc}} &= k_0^2(1-\tilde{n}^2)\mathbf{u}_{\mathrm{i}} && \text{in } \Omega, \\ \frac{\partial\mathbf{u}_{\mathrm{sc}}}{\partial\mathbf{n}} - ik_0\mathbf{u}_{\mathrm{sc}} &= 0 && \text{on } \partial\Omega, \\ \mathbf{u}_{\mathrm{sc}} + \mathbf{u}_{\mathrm{i}} &= \mathbf{u}_{\mathrm{t}} && \text{in } \overline{\Omega} \end{aligned} \tag{2.24}$$

for a known complex refractive index $\tilde{n}$. By $\frac{\partial}{\partial\mathbf{n}}$ we denote the partial directional derivative in the direction of the outward normal vector $\mathbf{n}$ of the boundary, which exists as we require the boundary to be a C^1-boundary. As the incident field $\mathbf{u}_{\mathrm{i}}$ and the total field $\mathbf{u}_{\mathrm{t}}$ fulfill the boundary condition, the scattered field $\mathbf{u}_{\mathrm{sc}}$ fulfills them automatically by the superposition principle.

2.4. An analysis of the inverse problem of THz tomography

The aim of this section is to establish the well-definedness of the scattering map S and the definition of the observation operator. We give a full description of the forward operator and analyze its

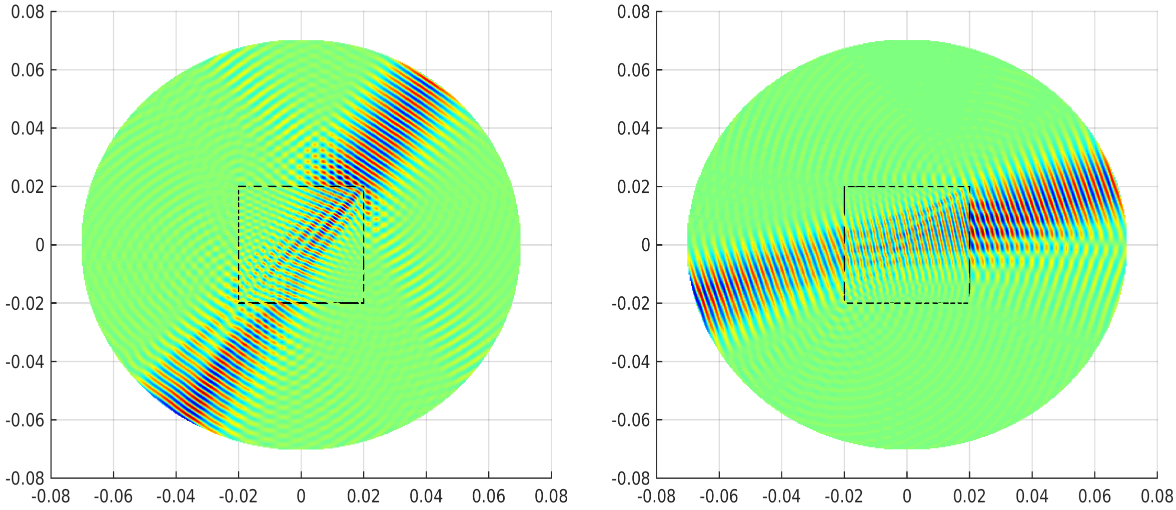

Figure 2.3.: Real part of the electromagnetic field (z-component) of a Gaussian THz beam with frequency $f = 0.1\,\mathrm{THz}$, beam waist $W_0 = 0.013\,\mathrm{m}$ and a Rayleigh zone of length $2y_0 = 0.146\,\mathrm{m}$, refracted, reflected, and attenuated by a plastic cuboid with complex refractive index $\tilde{n} = 1.5 + i \cdot 0.005$ and quadratic cross-section of the size $4\,\mathrm{cm} \times 4\,\mathrm{cm}$. The THz emitter is situated in the first quadrant outside the domain.

properties, also in view of a numerical solution of the inverse problem. This includes a derivation of the Fréchet derivative and the adjoint operator, which play an important role in regularization techniques (e.g., the Landweber iteration and particularly in the SESOP and RESESOP methods we want to apply later).

The parameter identification problem analyzed by Bao, Chen, and Ma in [6] using the Sommerfeld radiation condition and by Bao and Li in [7] together with Robin boundary conditions is called the *inverse medium problem*, in which the refractive index of an object is reconstructed from the boundary data. The scattering, penetrable object is illuminated by a one-parameter family of time-harmonic electromagnetic plane incident waves, where the parameter refers to the spatial frequency of the wave. The scattering object is considered a pure scatterer, i.e., the absorption is neglected. Consequently, the refractive index n is real-valued. The mathematical description of the inverse medium problem is also based on the Helmholtz equation and the superposition principle.
The inverse problem of THz tomography can likewise be interpreted as an inverse medium problem. However, the goal of THz tomography is the reconstruction of the full complex refractive index from (discrete) boundary measurements of the electric field, which is the result of a superposition of an incident Gaussian beam and the respective scattered, refracted, and attenuated beam. For an analysis of the forward operator of our parameter identification problem, we will use similar methods as in [7]. A more general description of the procedure can be found in [65].

So far, we have described how to obtain the total electric field from the knowledge of the complex refractive index given on a domain Ω. The complex refractive index $\tilde{n}$ can be defined as a piecewise continuous complex function on Ω. The jumps in $\tilde{n}$ occur at the boundaries between different materials, for example at the outer surface of the object. We assume that within one material, the value of $\tilde{n}$ changes continuously or is constant. Gradients in the complex refractive index can occur for example if the material has a certain moisture content. Porous materials such as sponges or foams often show this phenomenon. Objects that consist of one single material may have inclusions of air or impurities that have a different complex refractive index. Not only the classification of inclusions is of interest, but also the detection of the resulting inner interfaces. Their knowledge alone can be exploited in the adapted algebraic reconstruction technique that has been developed for THz tomography by Tepe et al., see [71].

In this work, we want to discuss a method to reconstruct the complex refractive index from discrete measurements of the total electric field on the boundary of the bounded domain Ω. We want to restrict ourselves to the two-dimensional case, i.e., we only consider objects that fulfill

$$\tilde{n}(\mathbf{x}) = \tilde{n}(x, y, z) = \tilde{n}(x, y, 0)$$

for all $z \in \mathbb{R}$ and thus neglect the change in $\tilde{n}$ in z-direction.

Regarding our scattering problem (2.24), we note that instead of $\tilde{n}$, we are dealing with its square, which is accordingly a piecewise continuous function on Ω and fulfills $\tilde{n}^2(\mathbf{x}) = 1$ outside the object. This motivates the following definition:

Definition 2.3. *Let $D \subseteq \Omega$ be the domain on which the complex refractive index $\tilde{n}$ is different from 1, i.e.,*

$$D := \operatorname{supp}(1 - \tilde{n}^2). \tag{2.25}$$

Furthermore, we define the complex valued function

$$m : \ \Omega \to \mathbb{C}, \ m(\mathbf{x}) := 1 - \tilde{n}^2(\mathbf{x}). \tag{2.26}$$

In Definition 2.3, the *support*

$$\operatorname{supp}(f) := \Omega \setminus \bigcup \left\{ U \subseteq \Omega \ : \ U \text{ open}, \ f|_U = 0 \text{ a.e.} \right\}$$

of a function $f : V \to \mathbb{C}$ (or $f : V \to \mathbb{R}$) is defined as the complement of the union of all open subsets of Ω, on which $f = 0$ almost everywhere. Hence, the support of f is closed.

The function m describes the same physical properties of the respective object as $\tilde{n}$. For this reason, it is specially suited for our modeling and later for the reconstruction. Since the support of $m : \Omega \to \mathbb{C}$ is bounded, the Heine-Borel theorem yields that m has a compact support.

Remark 2.4. *As $\tilde{n}$ is a bounded function on Ω, the function $m = 1 - \tilde{n}^2$ is also bounded. For our purposes, we use that m is square-integrable over Ω, such that*

$$m \in L^2_{\text{comp}}(\Omega) := \left\{ f \in L^2(\Omega) \ : \ \operatorname{supp}(f) \subseteq \Omega \right\}.$$

This allows us to work in a Hilbert space setting, where

$$m \in L^\infty(\Omega) \cap L^2_{\text{comp}}(\Omega) \subseteq L^2(\Omega).$$

The receivers used in a tomographic measurement setup detect only the z-component $E_z(\mathbf{x})$ of the THz beam's electric field $\mathbf{E}(\mathbf{x}) = (E_x(\mathbf{x}), E_y(\mathbf{x}), E_z(\mathbf{x}))^T$. As already stated, we are interested in reconstructing cross-sections of the tested object that are embedded in the x-y-plane. We treat our problem accordingly as a two-dimensional problem and aim at the reconstruction of a complex valued, bounded function supported in $\Omega \subseteq \mathbb{R}^2$ from discrete measurements of the corresponding scalar field, the z-component of the electric field, on the boundary of Ω. The underlying boundary value problem (2.24) holds for each component of the electric field. Together with the following definition, we can reduce the direct problem of THz tomography (in our setting) to a scalar two-dimensional boundary value problem.

Definition 2.5. *We define the z-component $E_z(\mathbf{x})$ in the x-y-plane by the scalar field u_t, i.e.,*

$$u_\mathrm{t}(x,y) := E_z(x,y,0) \qquad \text{for all } (x,y) \in \Omega \subseteq \mathbb{R}^2, \tag{2.27}$$

which is, according to the superposition principle, the sum

$$u_\mathrm{t}(x,y) = u_\mathrm{i}(x,y) + u_\mathrm{sc}(x,y)$$

of the z-components of the electric field of the incoming wave, denoted by u_i, and the scattered wave, denoted by u_sc.

Before taking a closer look at the measuring process and its mathematical modeling, we first want to establish the existence and uniqueness of the total electric field u_t, which is given by (2.24).

2.4.1. Existence and uniqueness of a weak solution of the Helmholtz equation using scattering boundary conditions

From now on, we will consider the complex refractive index m as an element of $L^\infty(\Omega) \cap L^2_\mathrm{comp}(\Omega) \subseteq L^2(\Omega)$, where the bounded domain Ω has a C^1-boundary $\partial\Omega$.

We want to establish the existence and uniqueness of a weak solution of the scattering problem we derived in the previous sections, given by the boundary value problem

$$u_\mathrm{sc} + u_\mathrm{i} = u_\mathrm{t} \qquad \text{in } \overline{\Omega}, \tag{2.28}$$

$$\Delta u_\mathrm{sc} + k_0^2(1-m)u_\mathrm{sc} = k_0^2 m u_\mathrm{i} \qquad \text{in } \Omega, \tag{2.29}$$

$$\frac{\partial u_\mathrm{sc}}{\partial \mathbf{n}} - ik_0 u_\mathrm{sc} = 0 \qquad \text{on } \partial\Omega. \tag{2.30}$$

The partial derivative $\frac{\partial}{\partial \mathbf{n}}$ is the directional derivative along the outside normal vector $\mathbf{n}$ of the boundary of the domain Ω. The boundary condition is well-defined due to our choice of Ω.

A useful setting for the analysis of boundary value problems are the Sobolev spaces $W^{k,p}(\Omega)$, which are subspaces of L^p-spaces and whose elements have a k-th weak derivative. The definition of Sobolev spaces, weak differentiability and some important properties can be found in the appendix, see B.2.1. We make use of the *variational formulation* of our boundary value problem (2.29), (2.30) in order to prove the existence and uniqueness of a *weak solution.* These methods are well-established and discussed in many standard references, see, e.g., [3, 12, 27, 50]. In the context of boundary value problems, a shorter overview of this theory together with a great variety of typical problems is presented in [64]. As we are working in an L^2 setting (i.e., in Hilbert spaces), we will only use the Sobolev spaces $H^k(\Omega) := W^{k,2}(\Omega)$, which are Hilbert spaces as well.

The techniques and proofs we present are inspired by the methods discussed in [65] and specifically in [7].

Before we establish the variational formulation of the boundary value problem given by the equations (2.29) and (2.30) for the existence and uniqueness proofs, we need some definitions to be able to work in an appropriate setting.
We define the standard inner products

$$(u,v) := \int_\Omega u\overline{v}\,\mathrm{d}\mathbf{x}$$

on $L^2(\Omega)$, and

$$\langle u, v \rangle := \int_{\partial\Omega} u\overline{v} \,\mathrm{d}s_{\mathbf{x}}$$

on $L^2(\partial\Omega)$. Note that the integral $\int_{\partial\Omega} u\overline{v} \,\mathrm{d}s_{\mathbf{x}}$ is to be understood in the context of *traces*, which makes sense if $\partial\Omega$ is at least of class C^1 (for reference, see, e.g., [27], chapters 5.4 and 5.5). We define the *trace operator*, which is discussed in detail in, e.g., [3, 5, 12, 27]. Some more statements are also to be found in the appendix in Section B.13.

Definition 2.6. *The operator*

$$\gamma : \ H^1(\Omega) \to L^2(\partial\Omega), \ u \mapsto u|_{\partial\Omega} \tag{2.31}$$

is called the trace operator*.*

Remark 2.7. *(a) The trace operator is a bounded, linear operator if $\partial\Omega$ is of class C^1. In that case, we have*

$$\|\gamma u\|_{L^2(\partial\Omega)} \leq c \|u\|_{H^1(\Omega)},$$

where the constant c depends on Ω, see, e.g., [3, 27].

(b) The above estimate will play a role in the proof of the existence of a weak solution, i.e., in the proof of Theorem 2.12.

At this point, we define the parameter-to-solution operator S, which plays an integral part in the direct and inverse problem of THz tomography.

Definition 2.8. *Let $u_\mathrm{i} \in H^1(\Omega)$ and $m \in L^\infty(\Omega) \cap L^2_{\mathrm{comp}}(\Omega)$. We define the mapping*

$$S : \mathcal{D}(S) \subseteq L^\infty(\Omega) \cap L^2_{\mathrm{comp}}(\Omega) \to H^1(\Omega), \ m \mapsto S(m) := u_\mathrm{t},$$

as the operator, that maps a function $m \in L^\infty(\Omega) \cap L^2_{\mathrm{comp}}(\Omega)$ to the field $u_\mathrm{t} \in H^1(\Omega)$, such that $u_\mathrm{t} = u_\mathrm{i} + u_\mathrm{sc}$ and u_sc is the solution of the boundary value problem (2.29), (2.30)*.*

Remark 2.9. *(a) In our setting, $u_\mathrm{i} \in H^1(\Omega)$ represents the incident field as defined in Section 2.1 and $m \in \mathcal{D}(S)$ the complex refractive index, see Definition 2.3. As u_i solves the paraxial Helmholtz equation and is continuously differentiable, the statement $u_\mathrm{i} \in H^1(\Omega)$ is valid. However, for most of our statements, we only use $u_\mathrm{i} \in L^2(\Omega)$.*

(b) By proving the existence and uniqueness of a weak solution of (2.29), (2.30)*, we obtain the well-definedness of the operator S.*

(c) The operator S can be interpreted as a mapping from $\big(\mathcal{D}(S)\big) \times H^1(\Omega)$ to $H^1(\Omega)$, when the incident field $u_\mathrm{i} \in H^1(\Omega)$ is considered as a variable, as it is done in [7]. In that case, S is linear with respect to u_i and nonlinear with respect to m. To emphasize this statement, we write

$$S(m, u_\mathrm{i}) = S(m)u_\mathrm{i}.$$

The linear operator $S(m)$ is bounded and, by consequence, continuous as an operator from $H^1(\Omega)$ to $H^1(\Omega)$, see [7]. In our case, the incident field is not changed during the measuring process apart from the shifts due to the change in the position of the emitter and receivers. We will thus focus on the nonlinear mapping S as defined before.

(d) In the proof of the existence and uniqueness of u_sc, the superposition principle (2.28) *does not play a role.*

Let the wave number $k_0 > 0$ be a fixed positive real number. To establish the variational formulation of the boundary value problem given by the equations (2.29) and (2.30), we multiply both sides of (2.29) with (the complex conjugate of) a test function $v \in H^1(\Omega)$ and integrate over the domain Ω, obtaining

$$\int_\Omega \Delta u_{\mathrm{sc}} \cdot \overline{v} \, \mathrm{d}\mathbf{x} + \int_\Omega k_0^2(1-m)u_{\mathrm{sc}} \cdot \overline{v} \, \mathrm{d}\mathbf{x} = \int_\Omega k_0^2 m u_{\mathrm{i}} \cdot \overline{v} \, \mathrm{d}\mathbf{x}.$$

Partial integration of the first term on the left-hand side yields

$$\int_{\partial\Omega} \frac{\partial u_{\mathrm{sc}}}{\partial \mathbf{n}} \cdot \overline{v} \, \mathrm{d}s_{\mathbf{x}} - \int_\Omega \nabla u_{\mathrm{sc}} \cdot \nabla \overline{v} \, \mathrm{d}\mathbf{x} + \int_\Omega k_0^2(1-m)u_{\mathrm{sc}} \cdot \overline{v} \, \mathrm{d}\mathbf{x} = \int_\Omega k_0^2 m u_{\mathrm{i}} \cdot \overline{v} \, \mathrm{d}\mathbf{x}.$$

We insert the boundary condition (2.30) into the first term and obtain

$$ik_0 \int_{\partial\Omega} u_{\mathrm{sc}} \cdot \overline{v} \, \mathrm{d}s_{\mathbf{x}} - \int_\Omega \nabla u_{\mathrm{sc}} \cdot \nabla \overline{v} \, \mathrm{d}\mathbf{x} + k_0^2 \int_\Omega (1-m)u_{\mathrm{sc}} \cdot \overline{v} \, \mathrm{d}\mathbf{x} = k_0^2 \int_\Omega m u_{\mathrm{i}} \cdot \overline{v} \, \mathrm{d}\mathbf{x}. \tag{2.32}$$

Accordingly, we define the sesquilinear form

$$a : H^1(\Omega) \times H^1(\Omega) \to \mathbb{C}$$

by

$$a(u,v) := (\nabla u, \nabla v) - k_0^2 \left((1-m)u, v\right) - ik_0 \langle u, v \rangle, \tag{2.33}$$

and the linear functional $b : H^1(\Omega) \to \mathbb{C}$ by

$$b(v) := -k_0^2 (m u_{\mathrm{i}}, v), \tag{2.34}$$

where $(\cdot,\cdot)$ and $\langle \cdot,\cdot \rangle$ are the L^2 inner products as defined earlier. However, for the sake of a better understanding, we will label the occurring norms and inner products in some proofs in this chapter. In the following, we show that there is a unique $u \in H^1(\Omega)$, such that

$$a(u,v) = b(v) \tag{2.35}$$

for all $v \in H^1(\Omega)$.

Important tools in the analysis of variational problems such as (2.35) are the Lax-Milgram lemma (B.3), the Riesz representation theorem (B.5), and the Fredholm alternative (B.6). First of all, we want to prove that there is at most one solution of our boundary value problem. In contrast to the inverse medium problem, we are now dealing with a complex valued coefficient function. The proof has to be adapted accordingly.

Lemma 2.10. *For some $m \in \mathcal{D}(S)$ with real part $m_{\mathrm{r}} := \mathrm{Re}(m)$ and imaginary part $m_{\mathrm{i}} := \mathrm{Im}(m) \leq 0$ there is at most one solution to the variational scattering problem* (2.35).

Proof. We consider the variational problem (2.35) for $v = u$, such that $a(u,u) = b(u)$. Due to the linearity of the elliptic partial differential equation it suffices to show that $u = 0$ in case there is no incident field, i.e., $u_{\mathrm{i}} = 0$. We then have

$$a(u,u) = \int_\Omega \nabla u \cdot \nabla \overline{u} \, \mathrm{d}\mathbf{x} - k_0^2 \int_\Omega (1-m)u \cdot \overline{u} \, \mathrm{d}\mathbf{x} - ik_0 \int_{\partial\Omega} u \cdot \overline{u} \, \mathrm{d}s_{\mathbf{x}} = 0.$$

We represent the complex refractive index $m = m_{\mathrm{r}} + i m_{\mathrm{i}}$ by its real and imaginary part and obtain

$$ik_0^2 \int_\Omega m_{\mathrm{i}} u \cdot \overline{u} \, \mathrm{d}\mathbf{x} = ik_0 \int_{\partial\Omega} u \cdot \overline{u} \, \mathrm{d}s_{\mathbf{x}}$$

for the imaginary part of the previous equation. We thus have

$$\|u\|^2_{L^2(\partial\Omega)} = k_0 \int_\Omega m_\mathrm{i} |u|^2 \,\mathrm{d}\mathbf{x} \leq 0,$$

as $m_\mathrm{i}(\mathbf{x}) \leq 0$ for all $\mathbf{x} \in \Omega$. We thus have $u|_{\partial\Omega} = 0$, such that our boundary condition now reads $\frac{\partial u}{\partial \mathbf{n}} = 0$ (Neumann boundary conditions). Hence, it remains to show that there is at most one solution of the Neumann boundary value problem

$$\begin{aligned} \Delta u + k_0^2(1-m)u &= 0 \qquad \text{in } \Omega, \\ \frac{\partial u}{\partial \mathbf{n}} &= 0 \qquad \text{on } \partial\Omega. \end{aligned} \tag{2.36}$$

Corollary 8.2 from [32] yields $u = 0$ in (2.36) on Ω and consequently, we have $u = 0$ on $\overline{\Omega}$. □

Remark 2.11. *The condition* $m_\mathrm{i} \leq 0$ *holds naturally due to* $m = 1-(n+i\kappa)^2 = 1-n^2+\kappa^2-i\cdot 2n\kappa$ *and* $n \geq 1$, $\kappa \geq 0$. *More precisely, it suffices that* $m_\mathrm{i} \leq 0$ *almost everywhere in* Ω.

Having established the uniqueness of a solution of the variational problem (2.35), we now have to prove its existence. In the following, we will always assume that the complex refractive index m fulfills

$$\operatorname{Im}(m) \leq 0,$$

such that we can apply Lemma 2.10.
Throughout this section, let $c_j > 0$, $j \in \mathbb{N}$, be positive constants.

Theorem 2.12. *Let* Ω *be a bounded domain with* C^1*-boundary* $\partial\Omega$, $k_0 \in \mathbb{R}^+$ *a nonnegative constant and* $u_\mathrm{i} \in H^1(\Omega)$ *the incident field. If* $m \in \mathcal{D}(S)$, *the variational problem* (2.35), *respectively the boundary value problem*

$$\begin{aligned} \Delta u + k_0^2(1-m)u &= k_0^2 m u_\mathrm{i} \qquad \text{in } \Omega, \\ \frac{\partial u}{\partial \mathbf{n}} - ik_0 u &= 0 \qquad \text{on } \partial\Omega, \end{aligned}$$

possesses a unique weak solution $u \in H^1(\Omega)$, *which fulfills*

$$\|u\|_{H^1(\Omega)} \leq C_1 \|m\|_{L^\infty(\Omega)} \|u_\mathrm{i}\|_{L^2(\Omega)} \tag{2.37}$$

for some constant $C_1 = C_1(k_0, \Omega) > 0$.

Proof. We split the sesquilinear form a into two sesquilinear forms $a_1, a_2 : H^1(\Omega) \times H^1(\Omega) \to \mathbb{C}$, where

$$a_1(v_1, v_2) = (\nabla v_1, \nabla v_2)_{L^2(\Omega)} - ik_0 \langle v_1, v_2 \rangle_{L^2(\partial\Omega)},$$

and

$$a_2(v_1, v_2) = -\big((1-m)v_1, v_2\big)_{L^2(\Omega)},$$

such that

$$a = a_1 + k_0^2 a_2.$$

Note that a_2 can be defined on $L^2(\Omega) \times L^2(\Omega)$ as well.
We first show that a_1 is bounded and coercive. From

$$\begin{aligned} |a_1(v_1, v_2)| &= \left| (\nabla v_1, \nabla v_2)_{L^2(\Omega)} - ik_0 \langle v_1, v_2 \rangle_{L^2(\partial\Omega)} \right| \\ &\leq |v_1|_{H^1(\Omega)} \cdot |v_2|_{H^1(\Omega)} + k_0 \|v_1\|_{L^2(\partial\Omega)} \cdot \|v_2\|_{L^2(\partial\Omega)} \\ &\leq \|v_1\|_{H^1(\Omega)} \cdot \|v_2\|_{H^1(\Omega)} + c_1 k_0 \|v_1\|_{H^1(\Omega)} \cdot \|v_2\|_{H^1(\Omega)} \\ &\leq c_2 k_0 \|v_1\|_{H^1(\Omega)} \cdot \|v_2\|_{H^1(\Omega)} \end{aligned}$$

we obtain the boundedness of a_1. We have used the semi-norm $|\cdot|_{H^1(\Omega)}$ on $H^1(\Omega)$, given by

$$|v|^2_{H^1(\Omega)} = \int_\Omega \nabla v \cdot \nabla \overline{v} \, \mathrm{d}\mathbf{x}$$

and satisfying $|v|_{H^1(\Omega)} \leq \|v\|_{H^1(\Omega)}$, and the trace theorem (for reference, see, e.g., [3, 27] and also B.13). The constant $c_2 > 0$ depends only on Ω.
The coercivity of a_1 is obtained by estimating

$$\begin{aligned}
\left|\big(a_1(v,v)\big)\right| &= \left| |v|^2_{H^1(\Omega)} - ik_0 \|v\|^2_{L^2(\partial\Omega)} \right| \\
&= \left(|v|^4_{H^1(\Omega)} + k_0^2 \|v\|^4_{L^2(\partial\Omega)} \right)^{1/2} \\
&\geq c_3 \left(|v|^2_{H^1(\Omega)} + k_0 \|v\|^2_{L^2(\partial\Omega)} \right) \\
&\geq c_4 k_0 \left(|v|^2_{H^1(\Omega)} + \|v\|^2_{L^2(\partial\Omega)} \right) \\
&\geq c_5 k_0 \|v\|^2_{H^1(\Omega)},
\end{aligned}$$

using the equivalence of the Euklidian norm and the ℓ^1-norm on $\mathbb{R}^2$,

$$\left\| \left(|v|^2_{H^1(\Omega)}, k_0 \|v\|^2_{L^2(\partial\Omega)} \right)^T \right\|_2 \geq c_3 \left\| \left(|v|^2_{H^1(\Omega)}, k_0 \|v\|^2_{L^2(\partial\Omega)} \right)^T \right\|_1,$$

and an estimate that can be found in [5], p. 214, which is another norm equivalence result. The constant c_5 depends only on Ω (also [5], p. 214).
In the following, we denote by

$$\Phi \,:\, H^1(\Omega) \to (H^1(\Omega))^*, \; v \mapsto (v, \cdot)_{H^1(\Omega)}$$

the isometric Riesz isomorphism (see, e.g., [12] and [76], Theorem V.3.6). The Lax-Milgram lemma yields the existence of an isomorphism $T : H^1(\Omega) \to H^1(\Omega)$ with $\|T\|_{H^1(\Omega)\to H^1(\Omega)} \leq c_2 k_0$ and $\|T^{-1}\|_{H^1(\Omega)\to H^1(\Omega)} \leq (c_5 k_0)^{-1}$, which satisfies

$$a_1(u,v) = (Tu, v)_{H^1(\Omega)}$$

for all $u, v \in H^1(\Omega)$ (this operator is associated to a_1, see [12, 64]). Now consider the mapping

$$\mathcal{B} \,:\, L^2(\Omega) \to (H^1(\Omega))^*, \; p \mapsto a_2(p, \cdot),$$

which is well-defined and for $p \in L^2(\Omega)$, the mapping $a_2(p,\cdot)$ is antilinear. For $w \in H^1(\Omega)$, we write $\mathcal{B}p[w] = a_2(p,w)$. For all $p \in L^2(\Omega)$ and $v \in H^1(\Omega)$, we have

$$\begin{aligned}
|a_2(p,v)| = \left| \big((1-m)p, v \big)_{L^2(\Omega)} \right| &\leq \|1-m\|_{L^\infty(\Omega)} \|p\|_{L^2(\Omega)} \|v\|_{L^2(\Omega)} \\
&\leq \|1-m\|_{L^\infty(\Omega)} \|p\|_{L^2(\Omega)} \|v\|_{H^1(\Omega)}.
\end{aligned}$$

Consequently, $a_2(p,\cdot)$ is continuous and we have $\|a_2(p,\cdot)\|_{(H^1(\Omega))^*} \leq \|1-m\|_{L^\infty(\Omega)} \|p\|_{L^2(\Omega)}$. This estimate also yields the boundedness of the linear mapping $\mathcal{B}$ with

$$\|\mathcal{B}\|_{L^2(\Omega)\to(H^1(\Omega))^*} \leq \|1-m\|_{L^\infty(\Omega)}.$$

We now define the linear operator

$$\tilde{\mathcal{A}} := T^{-1}\Phi^{-1}\mathcal{B} \,:\, L^2(\Omega) \to H^1(\Omega).$$

Consider the operator

$$\mathcal{A} : L^2(\Omega) \to H^1(\Omega) \hookrightarrow L^2(\Omega),\ p \mapsto \tilde{\mathcal{A}}p.$$

Since $H^1(\Omega)$ is compactly embedded in $L^2(\Omega)$, the operator $\mathcal{A} : L^2(\Omega) \to L^2(\Omega)$ is compact as a composition of a compact and a bounded linear operator. Note that $\mathcal{A}(L^2(\Omega)) \subseteq H^1(\Omega)$. We obtain for every $p \in L^2(\Omega)$ the estimate

$$\begin{aligned}\|\mathcal{A}p\|_{H^1(\Omega)} = \|\tilde{\mathcal{A}}p\|_{H^1(\Omega)} &\leq \|T^{-1}\|_{H^1(\Omega)\to H^1(\Omega)} \cdot \|\Phi^{-1}\mathcal{B}p\|_{H^1(\Omega)} \\ &\leq (c_5k_0)^{-1}\|\mathcal{B}p\|_{(H^1(\Omega))^*} \leq (c_5k_0)^{-1}\|1-m\|_{L^\infty(\Omega)}\|p\|_{L^2(\Omega)}\end{aligned}$$

and we compute

$$\begin{aligned}a_1(\mathcal{A}p, w) = a_1\big(\tilde{\mathcal{A}}p, w\big) = a_1\big(T^{-1}\Phi^{-1}\mathcal{B}p, w\big) &= \big(\Phi^{-1}\mathcal{B}p, w\big)_{H^1(\Omega)} \\ &= \big(\Phi(\Phi^{-1}\mathcal{B}p)\big)[w] = \mathcal{B}p[w] = a_2(p, w).\end{aligned}$$

Furthermore, the operator $\mathcal{A}$ is unique: Let $\mathcal{C} : L^2(\Omega) \to L^2(\Omega)$ be another bounded linear operator with $\mathcal{C}(L^2(\Omega)) \subseteq H^1(\Omega)$ and $a_1(\mathcal{C}p, w) = a_2(p, w)$ for every $p \in L^2(\Omega)$ and $w \in H^1(\Omega)$. This yields

$$\Phi T\mathcal{C}p = (T\mathcal{C}p, \cdot)_{H^1(\Omega)} = a_1(\mathcal{C}p, \cdot) = a_2(p, \cdot) = \mathcal{B}p,$$

and consequently

$$\mathcal{C}p = T^{-1}\Phi^{-1}\mathcal{B}p = \tilde{\mathcal{A}}p = \mathcal{A}p.$$

By $I : L^2(\Omega) \to L^2(\Omega)$, we denote the identity mapping in $L^2(\Omega)$. In the next step, we show that for every $k_0 > 0$ the operator $I + k_0^2\mathcal{A}$ is injective.
Let $p \in \mathcal{N}\big(I + k_0^2\mathcal{A}\big) \subseteq L^2(\Omega)$. Then we have $p = -k_0^2\mathcal{A}p \in H^1(\Omega)$ and thus

$$\begin{aligned}a_1(p, p) + k_0^2a_2(p, p) &= a_1\big(-k_0^2\mathcal{A}p, p\big) + k_0^2a_2(p, p) \\ &= -k_0^2a_1\big(\mathcal{A}p, p\big) + k_0^2a_2(p, p) \\ &= -k_0^2a_2(p, p) + k_0^2a_2(p, p) = 0.\end{aligned}$$

Our uniqueness result, Lemma 2.10, now yields $p = 0$. Hence, the operator $I + k_0^2\mathcal{A}$ is injective.
Consider now the (antilinear) functional $b \in (H^1(\Omega))^*$ and let $u \in H^1(\Omega)$. Using the definitions of a_1, a_2 and the operator $\mathcal{A}$, we see that our original variational problem of finding $u \in H^1(\Omega)$ which satisfies

$$a_1(u, v) + k_0^2a_2(u, v) = b(v)$$

for all $v \in H^1(\Omega)$ is equivalent to finding $u \in H^1(\Omega)$, such that

$$b(v) = a_1\big(u + k_0^2\mathcal{A}u, v\big) = \big(T\big(u + k_0^2\mathcal{A}\big), v\big)_{H^1(\Omega)}$$

for all $v \in H^1(\Omega)$. This yields $\Phi\big(T\big(I+k_0^2\mathcal{A}\big)u\big) = b$ and we finally obtain $u = \big(I+k_0^2\mathcal{A}\big)^{-1}T^{-1}\Phi^{-1}(b)$, such that our variational problem has at least one solution $u \in H^1(\Omega)$. Now put

$$\tilde{u} := T^{-1}\Phi^{-1}(b)$$

and we see that

$$b(v) = \big(\Phi T\tilde{u}\big)[v] = (T\tilde{u}, v) = a_1(\tilde{u}, v)$$

for all $v \in H^1(\Omega)$. Since $\mathcal{A}$ is compact and $I + k_0^2\mathcal{A}$ is injective, the Fredholm alternative is applicable and yields the existence of a unique $u \in H^1(\Omega)$, such that

$$\big(I + k_0^2\mathcal{A}\big)u = \tilde{u}, \tag{2.38}$$

and the boundedness of the inverse of $I + k_0^2\mathcal{A}$, i.e.,

$$\left\| \left(I + k_0^2\mathcal{A}\right)^{-1} \right\|_{H^1(\Omega)\to H^1(\Omega)} \leq c_6, \tag{2.39}$$

where $c_6 = c_6(k_0)$ depends on the wave number k_0. We estimate

$$\begin{aligned} \|u\|_{H^1(\Omega)} &\leq \left\|I + k_0^2\mathcal{A}\right\|_{H^1(\Omega)}^{-1} \|\tilde{u}\|_{H^1(\Omega)} \\ &\leq c_6 \left\|T^{-1}\right\|_{H^1(\Omega)\to H^1(\Omega)} \left\|\Phi^{-1}b\right\|_{H^1(\Omega)} \\ &\leq c_6 (c_5 k_0)^{-1} \left\|\Phi^{-1}b\right\|_{H^1(\Omega)} \end{aligned}$$

and together with the boundedness of b, which we derive from

$$\begin{aligned} \|b\|_{(H^1(\Omega))^*} = \sup_{\|v\|_{H^1(\Omega)}=1} |b(v)| &= \sup_{\|v\|_{H^1(\Omega)}=1} |k_0^2(mu_{\mathrm{i}}, v)| \\ &\leq \sup_{\|v\|_{H^1(\Omega)}=1} k_0^2 \|m\|_{L^\infty(\Omega)} \|u_{\mathrm{i}}\|_{L^2(\Omega)} \|v\|_{L^2(\Omega)} \\ &\leq \sup_{\|v\|_{H^1(\Omega)}=1} k_0^2 \|m\|_{L^\infty(\Omega)} \|u_{\mathrm{i}}\|_{L^2(\Omega)} \|v\|_{H^1(\Omega)} \\ &\leq k_0^2 \|m\|_{L^\infty(\Omega)} \|u_{\mathrm{i}}\|_{L^2(\Omega)}, \end{aligned}$$

we finally arrive at

$$\|u\|_{H^1(\Omega)} \leq c_6 (c_5 k_0)^{-1} \cdot k_0^2 \|m\|_{L^\infty(\Omega)} \|u_{\mathrm{i}}\|_{L^2(\Omega)} = C_1 \|m\|_{L^\infty(\Omega)} \|u_{\mathrm{i}}\|_{L^2(\Omega)}, \tag{2.40}$$

where c_5 is independent of k_0, whereas $C_1 = C_1(k_0, \Omega) := c_5^{-1} c_6 \cdot k_0$. ☐

Lemma 2.13. *If k_0 is sufficiently small, we obtain the more explicit estimate*

$$\|u\|_{H^1(\Omega)} \leq \tilde{C}_1 k_0 \|m\|_{L^\infty(\Omega)} \|u_{\mathrm{i}}\|_{L^2(\Omega)}, \tag{2.41}$$

where $\tilde{C}_1 = \tilde{C}_1(\Omega)$, for the weak solution $u \in H^1(\Omega)$, replacing the estimate (2.37) *from Theorem 2.12.*

Proof. In the proof of Theorem 2.12 we have derived the operator equation (2.38). At this point, if k_0 is small enough, we conclude that the operator $\mathcal{A}_{k_0} := I + k_0^2\mathcal{A} = I - (ik_0)^2\mathcal{A}$ has a uniformly bounded inverse: Define $\mathcal{T}_{k_0} := -{k_0}^2\mathcal{A}$, such that $\|\mathcal{T}_{k_0}\|_{H^1(\Omega)\to H^1(\Omega)} = {k_0}^2 \|\mathcal{A}\|_{H^1(\Omega)\to H^1(\Omega)}$. Let $q \in (0,1)$. Consequently, if $k_0 < \sqrt{q\|\mathcal{A}\|^{-1}}$, we have $\|\mathcal{T}_{k_0}\|_{H^1(\Omega)\to H^1(\Omega)} < q < 1$, and the operator $\mathcal{A}_{k_0}$ is invertible with inverse

$$\mathcal{A}_{k_0}^{-1} = \sum_{j=0}^{\infty} \mathcal{T}_{k_0}^j,$$

which is a Neumann series (for reference, see, e.g., [76]). According to

$$\left\|\mathcal{A}_{k_0}^{-1}\right\|_{H^1(\Omega)\to H^1(\Omega)} \leq \sum_{j=0}^{\infty} \|\mathcal{T}_{k_0}\|_{H^1(\Omega)\to H^1(\Omega)}^j < \sum_{j=0}^{\infty} q^j = \frac{1}{1-q},$$

the inverse is uniformly bounded.
We thus have

$$\|u\|_{H^1(\Omega)} \leq (1-q)^{-1} \|\tilde{u}\|_{H^1(\Omega)}, \tag{2.42}$$

where $1-q$ is independent of k_0.
We now continue as in the proof of Theorem 2.12, keeping in mind the new bound of $(I+k_0^2\mathcal{A})$, and obtain

$$\|u\|_{H^1(\Omega)} \le \tilde{C}_1 k_0 \|m\|_{L^\infty(\Omega)} \|u_{\mathrm{i}}\|_{L^2(\Omega)}$$

by setting $\tilde{C}_1 = \tilde{C}_1(\Omega) := (1-q)^{-1} c_5$. □

We specify the domain of the scattering operator S by

$$\mathcal{D}(S) \subseteq \left\{ m \in L^\infty(\Omega) \cap L^2_{\mathrm{comp}}(\Omega) \;:\; \|m\|_{L^\infty(\Omega)} \le M,\, \mathrm{Im}(m) \le 0 \right\}$$

for some $M>0$ and conclude our analysis by proving a continuity result for S on Ω.

Lemma 2.14. *Let $m_1, m_2 \in \mathcal{D}(S)$. Then we have*

$$\|S(m_1) - S(m_2)\|_{H^1(\Omega)} \le C_2 \|m_1 - m_2\|_{L^\infty(\Omega)} \|u_{\mathrm{i}}\|_{L^2(\Omega)}, \tag{2.43}$$

where $C_2 = C_2(k_0, \Omega, M) > 0$ and $u_{\mathrm{i}} \in H^1(\Omega)$ is the incident field, i.e., S is Lipschitz-continuous.

Proof. We set $u_{(1)} := S(m_1) - u_{\mathrm{i}}$ and $u_{(2)} := S(m_2) - u_{\mathrm{i}}$, such that

$$\Delta u_{(j)} + k_0^2 (1 - m_j) u_{(j)} = k_0^2 m_j u_{\mathrm{i}}, \quad j = 1, 2. \tag{2.44}$$

From Theorem 2.12 we deduce that

$$\left\|u_{(j)}\right\|_{H^1(\Omega)} \le C_1 \|m_j\|_{L^\infty(\Omega)} \|u_{\mathrm{i}}\|_{L^2(\Omega)}. \tag{2.45}$$

By subtracting equation (2.44) for $j=2$ from the one for $j=1$ and by setting $w := u_{(1)} - u_{(2)}$ we obtain

$$\Delta w + k_0^2 (1 - m_1) w = k_0^2 (m_1 - m_2) \left(u_{\mathrm{i}} + u_{(2)}\right). \tag{2.46}$$

Note that w satisfies the Robin boundary condition of our scattering problem, such that we can apply Theorem 2.12. We thus have

$$\|w\|_{H^1(\Omega)} \le C_1 \|m_1 - m_2\|_{L^\infty(\Omega)} \left\|u_{\mathrm{i}} + u_{(2)}\right\|_{L^2(\Omega)}.$$

Combining this estimate with $\left\|u_{(2)}\right\|_{L^2(\Omega)} \le \left\|u_{(2)}\right\|_{H^1(\Omega)}$ and (2.45) for $j=2$ yields

$$\begin{aligned}
\|S(m_1) - S(m_2)\|_{H^1(\Omega)} &= \left\|u_{(1)} - u_{(2)}\right\|_{H^1(\Omega)} \\
&\le C_1 \|m_1 - m_2\|_{L^\infty(\Omega)} \left\|u_{\mathrm{i}} + u_{(2)}\right\|_{L^2(\Omega)} \\
&\le C_1 \|m_1 - m_2\|_{L^\infty(\Omega)} \left(\|u_{\mathrm{i}}\|_{L^2(\Omega)} + \left\|u_{(2)}\right\|_{L^2(\Omega)}\right) \\
&\le C_2 \|m_1 - m_2\|_{L^\infty(\Omega)} \|u_{\mathrm{i}}\|_{L^2(\Omega)},
\end{aligned}$$

where $C_2 = C_2(k_0, \Omega, M) := C_1(1 + C_1 M)$. □

Before we move on to the linearized scattering problem, we want to summarize our previous results. We have considered the scattering map S, which is a nonlinear operator that maps $m \in \mathcal{D}(S)$ to the electric field (or rather its z-component) $u \in H^1(\Omega)$. This mapping is well-defined and S is continuous as an operator from $\mathcal{D}(S)$ to $H^1(\Omega)$.

2.4.2. The linearized scattering problem

The following considerations are to be understood in the weak sense, even though we formulate the occurring boundary value problems in the classical sense.

The mathematical model of the direct problem in THz tomography is described by the scattering map S, which we discussed in the previous section, and some observation operator that maps the electric field u to the measured values in the data space. Due to the nonlinearity of the parameter-to-solution mapping S, the corresponding inverse problem belongs to the class of nonlinear inverse problems (in Hilbert spaces). These are usually solved iteratively, for example with a Landweber iteration. For these methods, the knowledge of the linearization of the forward operator is essential. In the proof of the continuity result for the scattering map S, we have deduced a boundary value problem which gives rise to the following definition.

Definition 2.15. *For some fixed $m \in \mathcal{D}(S)$ and the respective solution $u_{\mathrm{t}} := S(m)$ of the scattering problem* (2.28)-(2.30)*, let $T_m : L^\infty(\Omega) \cap L^2_{\mathrm{comp}}(\Omega) \to H^1(\Omega)$ be the operator that maps some $h \in L^\infty(\Omega) \cap L^2_{\mathrm{comp}}(\Omega)$ to the solution of the boundary value problem*

$$\Delta w + k_0^2(1-m)w = k_0^2 h \cdot u_{\mathrm{t}} \qquad \textit{in } \Omega, \tag{2.47}$$

$$\frac{\partial w}{\partial \mathbf{n}} - ik_0 w = 0 \qquad \textit{on } \partial\Omega. \tag{2.48}$$

Let us for now assume that S is Gâteaux differentiable in an open neighborhood around $m \in \mathcal{D}(S)$. The Gâteaux differentiability in m yields the existence of the limit

$$\lim_{\alpha \to 0} \frac{\big(S(m+\alpha h) - S(m)\big)}{\alpha}. \tag{2.49}$$

The boundary value problem (2.47), (2.48) is obtained from the original scattering problem (2.28)-(2.30) by considering, for some $m \in \mathcal{D}(S)$, the perturbed boundary value problem

$$\Delta u_{\mathrm{sc,h}} + k_0^2\big(1-(m+\alpha h)\big)u_{\mathrm{sc,h}} = k_0^2(m+\alpha h)u_{\mathrm{i}} \qquad \text{in } \Omega,$$

$$\frac{\partial u_{\mathrm{sc,h}}}{\partial \mathbf{n}} - ik_0 u_{\mathrm{sc,h}} = 0 \qquad \text{on } \partial\Omega,$$

where $u_{\mathrm{sc,h}} := S(m+\alpha h) - u_{\mathrm{i}}$. As before, we define $u_{\mathrm{sc}} := S(m) - u_{\mathrm{i}}$ and note that both fields u_{sc} and $u_{\mathrm{sc,h}}$ fulfill the Robin boundary condition (2.30).
Note that $u_{\mathrm{sc}}, u_{\mathrm{sc,h}} \in H^1(\Omega)$, which follows from our analysis of the scattering map S. We subtract the Helmholtz equation for u_{sc} from the one for $u_{\mathrm{sc,h}}$ and obtain

$$\Delta\big(u_{\mathrm{sc,h}} - u_{\mathrm{sc}}\big) + k_0^2(1-m)\big(u_{\mathrm{sc,h}} - u_{\mathrm{sc}}\big) = k_0^2(u_{\mathrm{sc,h}} + u_{\mathrm{i}})\alpha h,$$

which can be reformulated as

$$\Delta\big(S(m+\alpha h) - S(m)\big) + k_0^2(1-m)\big(S(m+\alpha h) - S(m)\big) = k_0^2\big(S(m+\alpha h)\big)\alpha h.$$

We divide this expression by α and consider the weak formulation (2.35) of this partial differential equation,

$$\int_\Omega \nabla u_\alpha \cdot \nabla \overline{v} \,\mathrm{d}\mathbf{x} - k_0^2 \int_\Omega (1-m)u_\alpha \cdot \overline{v} \,\mathrm{d}\mathbf{x} - ik_0 \int_{\partial\Omega} u_\alpha \cdot \overline{v} \,\mathrm{d}s_{\mathbf{x}} = -k_0^2 \int_\Omega m u_{\mathrm{i}} \cdot \overline{v} \,\mathrm{d}\mathbf{x}, \tag{2.50}$$

where we have replaced u by

$$u_\alpha := \frac{\big(S(m+\alpha h) - S(m)\big)}{\alpha}.$$

We have postulated the existence of the limit $\lim_{\alpha\to 0} u_\alpha$ and assume $|\alpha| \le \overline{\alpha}$ for some $\overline{\alpha} > 0$. Note that due to our previous findings, we estimate

$$\|\nabla u_\alpha\|_{L^2(\Omega)} = |u_\alpha|_{H^1(\Omega)} \le \|u_\alpha\|_{H^1(\Omega)} \le c(k_0, \overline{\alpha}, \Omega, \|m\|_{L^\infty(\Omega)}) \|h\|_{L^\infty(\Omega)} \|u_{\mathrm{i}}\|_{L^2(\Omega)}.$$

As a consequence,

$$\sup_{|\alpha|\le\overline{\alpha}} \big(\nabla u_\alpha \cdot \nabla \overline{v}\big) \in L^1(\Omega).$$

Obviously, our previous analysis also yields

$$\sup_{|\alpha|\le\overline{\alpha}} \big((1-m)u_\alpha \cdot \overline{v}\big) \in L^1(\Omega), \quad \sup_{|\alpha|\le\overline{\alpha}} \big(u_\alpha \cdot \overline{v}\big) \in L^1(\partial\Omega), \quad \sup_{|\alpha|\le\overline{\alpha}} \big(m u_{\mathrm{i}} \cdot \overline{v}\big) \in L^1(\Omega).$$

We let α tend to zero in (2.50). The dominated convergence theorem (see, e.g., [24]) now allows us to interchange limit and integration. Additionally, the continuity of the operator $\nabla : H^1(\Omega) \to L^2(\Omega)$, which follows from $\|\nabla u\|_{L^2(\Omega)} = |u|_{H^1(\Omega)} \le \|u\|_{H^1(\Omega)}$, allows a further interchange of limit and differentiation. We thus have derived a variational formulation of

$$\Delta \lim_{\alpha\to 0} \frac{\big(S(m+\alpha h) - S(m)\big)}{\alpha} + k_0^2(1-m) \lim_{\alpha\to 0} \frac{\big(S(m+\alpha h) - S(m)\big)}{\alpha} = k_0^2 \lim_{\alpha\to 0} \big(S(m+\alpha h)\big) h$$

with Robin boundary conditions. Since S is continuous, the right-hand side converges to $k_0^2 S(m) h$ for $\alpha \to 0$. Now define

$$w := \lim_{\alpha\to 0} u_\alpha = \lim_{\alpha\to 0} \frac{\big(S(m+\alpha h) - S(m)\big)}{\alpha},$$

which fulfills the inhomogeneous Helmholtz equation (2.47) from the definition of the linear operator T_m. This yields a candidate for the Fréchet derivative of the scattering map S in m. We will further investigate the linear mapping T_m, prove that S is Fréchet differentiable and show that its Fréchet derivative coincides with the operator T_m.

Remark 2.16. *(a) In the following, we will restrict ourselves to formulating the occurring boundary value problems in the classical formulation, but consider only the weak solutions. The statements are therefore to be understood in the weak sense.*

(b) Note that the linear operator T_m depends on the complex refractive index, i.e., m is not a variable in Definition 2.15, but rather a parameter. In fact, m corresponds to the point in which the nonlinear operator S is linearized, as the calculation above shows.

(c) The superposition principle does no longer play a role in the linearized scattering problem.

Similar techniques as applied in the previous section allow us to prove the existence of a weak solution $w \in H^1(\Omega)$ of the boundary value problem (2.47), (2.48), such that T_m is well-defined on $L^\infty(\Omega) \cap L^2_{\mathrm{comp}}(\Omega)$. Also, we can deduce that T_m is bounded and therefore continuous. We will skip the proof as it is similar to the proof of Theorem 2.12 and the subsequent statements.

Lemma 2.17. *Let $m \in \mathcal{D}(S)$ and $u_{\mathrm{i}} \in H^1(\Omega)$ be fixed. The operator*

$$T_m : L^\infty(\Omega) \cap L^2_{\mathrm{comp}}(\Omega) \to H^1(\Omega), \ T_m(h) := w,$$

where w is the unique solution of (2.47), (2.48), is linear and bounded. For $h \in L^\infty(\Omega) \cap L^2_{\mathrm{comp}}(\Omega)$, we have

$$\|T_m h\|_{H^1(\Omega)} \le C_3 \|h\|_{L^\infty(\Omega)} \cdot \|u_{\mathrm{i}}\|_{L^2(\Omega)}, \tag{2.51}$$

where $C_3 := C_1(1 + C_1 M)$ is a constant that depends on k_0, M, and the domain Ω.

Let us now consider the mapping $\tilde{T} : \mathcal{D}(S) \to L\big(\mathcal{D}(S), H^1(\Omega)\big)$, where $m \mapsto \tilde{T}(m) := T_m$. This operator maps a bounded, compactly supported function m to the respective linear operator T_m. We can formulate a continuity result for this mapping.

Lemma 2.18. *Let $m_1, m_2 \in \mathcal{D}(S)$, $h \in L^\infty(\Omega) \cap L^2_{\text{comp}}(\Omega)$, and $u_{\text{i}} \in H^1(\Omega)$. The mapping $\tilde{T}$ fulfills*

$$\left\|\tilde{T}(m_1)h - \tilde{T}(m_2)h\right\|_{H^1(\Omega)} \leq C_4 \left\|m_1 - m_2\right\|_{L^\infty(\Omega)} \cdot \left\|h\right\|_{L^\infty(\Omega)} \cdot \left\|u_{\text{i}}\right\|_{L^2(\Omega)}, \tag{2.52}$$

where $C_4 = C_4\big(k_0, M, \Omega\big)$.

Proof. For $w_j := \tilde{T}(m_j)h = T_{m_j}h$, $j = 1, 2$, we have

$$\Delta w_j + k_0^2(1 - m_j)w_j = k_0^2 h \cdot S(m_j).$$

By subtracting these two equations from each other, we obtain

$$\Delta(w_1 - w_2) + k_0^2(1 - m_1)(w_1 - w_2) = k_0^2 h\big(S(m_1) - S(m_2)\big) + k_0^2(m_1 - m_2)w_2.$$

Using the previously applied methods again, we obtain

$$\left\|w_1 - w_2\right\|_{H^1(\Omega)} \leq k_0 \Big(\left\|h\right\|_{L^\infty(\Omega)} \cdot \left\|S(m_1) - S(m_2)\right\|_{H^1(\Omega)} + \left\|m_1 - m_2\right\|_{L^\infty(\Omega)} \cdot \left\|w_2\right\|_{H^1(\Omega)}\Big)$$

Finally, we use Lemma 2.14 and Lemma 2.17 to further estimate

$$\left\|w_1 - w_2\right\|_{H^1(\Omega)} \leq k_0(C_2 + C_3) \left\|h\right\|_{L^\infty(\Omega)} \cdot \left\|m_1 - m_2\right\|_{L^\infty(\Omega)} \cdot \left\|u_{\text{i}}\right\|_{L^2(\Omega)}$$

and set $C_4 := k_0(C_2 + C_3)$. ☐

Theorem 2.19. *The operator S from Definition 2.8 is Fréchet differentiable with respect to $m \in \mathcal{D}(S)$. The Fréchet derivative in $m \in \mathcal{D}(S)$ is the linear parameter-to-solution operator*

$$S'(m) : L^\infty(\Omega) \cap L^2_{\text{comp}}(\Omega) \to H^1(\Omega), \; h \mapsto S'(m)h = w, \tag{2.53}$$

where $w \in H^1(\Omega)$ solves the linearized boundary value problem

$$\Delta w + k_0^2(1 - m)w = k_0^2 u_{\text{t}} \cdot h \qquad \text{in } \Omega, \tag{2.54}$$

$$\frac{\partial w}{\partial \mathbf{n}} - ik_0 w = 0 \qquad \text{on } \partial\Omega. \tag{2.55}$$

The function $u_{\text{t}} := S(m)$ is the solution of the scattering problem (2.28)-(2.30).
We thus have $S'(m)h = T_m h$ for all $h \in L^\infty(\Omega) \cap L^2_{\text{comp}}(\Omega)$ and $S'(m)$ is continuous.

Proof. If there is a positive constant $C_5 = C_5(k_0, M, \Omega)$, such that the estimate

$$\|S(m + h) - S(m) - T_m h\|_{H^1(\Omega)} \leq C_5 \|h\|^2_{L^\infty(\Omega)} \cdot \|u_{\text{i}}\|_{L^2(\Omega)} \tag{2.56}$$

holds for $m, m + h \in \mathcal{D}(S)$, we are done.
Define the functions

$$\begin{aligned} u_{\text{sc}} &:= S(m) - u_{\text{i}}, \\ u_{\text{sc,h}} &:= S(m + h) - u_{\text{i}}, \\ w &:= T_m h, \end{aligned}$$

which fulfill the Robin boundary condition and

$$\begin{aligned}\Delta u_{\mathrm{sc}} + k_0^2\big(1-m\big)u_{\mathrm{sc}} &= k_0^2 m u_{\mathrm{i}},\\ \Delta u_{\mathrm{sc,h}} + k_0^2\big(1-(m+h)\big)u_{\mathrm{sc,h}} &= k_0^2\big(m+h\big)u_{\mathrm{i}},\\ \Delta w + k_0^2\big(1-m\big)w &= k_0^2 h\big(u_{\mathrm{sc}}+u_{\mathrm{i}}\big).\end{aligned}$$

From these equations, we obtain for $v := u_{\mathrm{sc,h}} - u_{\mathrm{sc}} - w = S(m+h) - S(m) - T_m h$ the Helmholtz equation

$$\Delta v + k_0^2(1-m)v = k_0^2 h\big(u_{\mathrm{sc,h}} - u_{\mathrm{sc}}\big),$$

and, noting that v fulfills the Robin boundary condition (2.30), we estimate

$$\begin{aligned}\|v\|_{H^1(\Omega)} &\le C_1\,\|h\|_{L^\infty(\Omega)}\cdot\|u_{\mathrm{sc,h}}-u_{\mathrm{sc}}\|_{L^2(\Omega)}\\ &\le C_1\,\|h\|_{L^\infty(\Omega)}\cdot\|u_{\mathrm{sc,h}}-u_{\mathrm{sc}}\|_{H^1(\Omega)}\\ &\le C_1C_2\,\|h\|^2_{L^\infty(\Omega)}\cdot\|u_{\mathrm{i}}\|_{L^2(\Omega)},\end{aligned}$$

where we have used Lemma 2.14. Resubstituting v again, we finally have shown

$$\|S(m+h)-S(m)-T_m h\|_{H^1(\Omega)} \le C_5\,\|h\|^2_{L^\infty(\Omega)}\cdot\|u_{\mathrm{i}}\|$$

with $C_5 = C_5(k_0, M, \Omega) = C_1C_2 > 0$. The continuity of $S'(m)$ is a direct result of the boundedness of T_m. ☐

Lemma 2.20. *For $m_1, m_2 \in \mathcal{D}(S)$, the operator S fulfills the estimate*

$$\|S(m_1)-S(m_2)-S'(m_1)(m_1-m_2)\|_{L^2(\Omega)} \le C_6\|S(m_1)-S(m_2)\|_{L^2(\Omega)}, \tag{2.57}$$

where $C_6 = C_6\big(k_0, M, \Omega\big)$.

Proof. Let $u_1 := S(m_1) - u_{\mathrm{i}}$, $u_2 := S(m_2) - u_{\mathrm{i}}$ and $w := S'(m_1)(m_1-m_2)$, which fulfill

$$\begin{aligned}\Delta u_1 + k_0^2(1-m_1)u_1 &= k_0^2 m_1 u_{\mathrm{i}},\\ \Delta u_2 + k_0^2(1-m_2)u_2 &= k_0^2 m_2 u_{\mathrm{i}},\\ \Delta w + k_0^2(1-m_1)w &= k_0^2(m_1-m_2)(u_1+u_{\mathrm{i}}).\end{aligned}$$

Additionally, u_1, u_2, w, and consequently $u_1 - u_2 - w$ fulfill the Robin boundary condition. In particular, we have $u_1, u_2, w \in H^1(\Omega) \subseteq L^2(\Omega)$ according to our previous results.
Subtracting the equations for u_2 and w from the one for u_1 yields

$$\Delta(u_1-u_2-w) + k_0^2(1-m_1)(u_1-u_2-w) = k_0^2(m_1-m_2)(u_2-u_1).$$

As before, we now estimate

$$\begin{aligned}\|u_1-u_2-w\|_{L^2(\Omega)} &\le \|u_1-u_2-w\|_{H^1(\Omega)}\\ &\le C_1\|m_1-m_2\|_{L^\infty(\Omega)}\cdot\|u_1-u_2\|_{L^2(\Omega)}\\ &\le C_1\cdot 2M\cdot\|u_1-u_2\|_{H^1(\Omega)},\end{aligned}$$

which is equivalent to (2.57) for $C_6 := 2C_1M$ due to our definitions of u_1, u_2, and w. ☐

Remark 2.21. *For the constant C_6 in the estimate* (2.57) *holds*

$$C_6\big(k_0, M, \Omega\big) < 1 \tag{2.58}$$

for M sufficiently small. Lemma 2.20 then states the validity of the tangential cone condition (1.32) *in the ball $B_\rho(m_1)$, which we postulated for the analysis of the sequential subspace optimization methods in Chapter 1. Assuming the tangential cone condition holds, the choice of c_{tc} in* (1.32) *depends in particular on the wave number k_0 and has to be adapted when working with different frequencies.*

Note that the estimate (2.57) *is valid in $H^1(\Omega)$ as well, according to the proof of Lemma 2.20.*

With Lemma 2.20 we conclude our analysis of the scattering map S. We now proceed to a complete description of the forward operator and its adjoint (which is an important tool for the numerical solution of the inverse problem), most of which is related to the measuring process and, as a consequence, the definition of the observation operator.

In many tomographic methods, the radiation that is used to scan the object is measured on some curve around the object, usually a circle. In these cases, it is suitable to define the domain of interest, i.e., the domain in which a parameter is supposed to be reconstructed, by the positions of the receivers that generate the data.

In THz tomography, the electric field u_{t} is measured by a fixed number of receivers that are arranged on a circle. During the measuring process, the tomograph, consisting of one emitter and the receivers, is rotated around the object with a certain step size, such that the tomograph defines the domain Ω as the interior of the corresponding circle. Consequently, we assume the surfaces of the sensors in the receivers to be a subset of the boundary of Ω, i.e., the data is generated purely on $\partial\Omega$.

The observation operator, which models the measuring process and will be discussed later, is defined as a function on $\partial\Omega$. This means we first have to restrict the total field u_{t} to the boundary, before we apply the observation operator. The restriction of a (weakly differentiable) function u to the boundary of a domain Ω is the well-known trace operator, which we introduced at the beginning of this section in Definition 2.6.

Remark 2.22. *A linear operator T is Fréchet differentiable, if and only if T is continuous, see [76]. Consequently, the trace operator γ is Fréchet differentiable.*

Corollary 2.23. *The composition $\gamma S : \mathcal{D}(S) \to L^2(\partial\Omega)$ is Fréchet-differentiable with Fréchet-derivative $\gamma S'(m)$, which fulfills*

$$\gamma S'(m)h = w|_{\partial\Omega} \tag{2.59}$$

for $h \in L^\infty(\Omega) \cap L^2_{\mathrm{comp}}(\Omega)$ and $w = S'(m)h$.

To complete the forward model of THz tomography, it remains to define the observation operator Q, which maps the restricted field γu_{t} to the data. The forward operator F will be defined as the composition of the scattering map S, the trace operator γ and the observation operator Q. Finally, we aim at solving the nonlinear operator equation

$$F(m) = y.$$

We mentioned before that nonlinear inverse problems are usually solved iteratively. A standard method is the nonlinear Landweber method. In each step of the Landweber iteration, the new iterate is located on a half-line that is spanned by the negative gradient

$$-\,g(m) := -\big(F'(m)\big)^* \left(F(m) - y\right) \tag{2.60}$$

of the least squares functional

$$\Psi(m) := \frac{1}{2}\left\|F(m) - y\right\|^2,$$

evaluated at the current iterate, where $(F'(m))^*$ is the adjoint of the forward operator's linearization in m. As we have seen in Chapter 1, the above gradient also plays an important role in sequential subspace optimization methods. Hence, the knowledge of the adjoint of the linearized operator $F'(m)$ is essential.

For simplicity, we will choose a continuous linear observation operator Q. In that case, we have

$$F : \mathcal{D}(S) \to \mathbb{C}^N,\ F(m) = Q\gamma S(m)$$

for $m \in \mathcal{D}(S)$. As both Q and γ are linear and continuous, the forward operator F is Fréchet differentiable in m and we obtain for the linearized forward operator

$$F'(m) : L^\infty(\Omega) \cap L^2_{\text{comp}}(\Omega) \to \mathbb{C}^N,\ F'(m)h = Q\gamma S'(m)h$$

for $h \in L^\infty(\Omega) \cap L^2_{\text{comp}}(\Omega)$. The adjoint of $F'(m)$ is thus given by

$$\big(F'(m)\big)^* = S'(m)^*\gamma^*Q^* : \mathbb{C}^N \to L^2(\Omega),$$

see [76]. Our choice of the observation operator Q will allow an explicit form of Q^*.

Before moving on to the definition of the observation operator, we calculate the operator $S'(m)^*\gamma^*$. Instead of finding descriptions for both operators separately, we will, as it has been done in [7], consider the composition of the two operators γ and $S'(m)$ to determine the adjoint operator of this composition.

2.4.3. The adjoint linearized problem

While the Fréchet derivative $\gamma S'(m)$ of the composition γS in $m \in \mathcal{D}(S)$ maps a bounded, complex valued function with compact support in Ω to a function on $\partial\Omega$, the adjoint operator $(S'(m))^*\gamma^*$ maps an element of $\big(L^2(\partial\Omega)\big)^* \cong L^2(\partial\Omega)$ to a function $\delta m \in L^2(\Omega)$.

We define the composition of the operators γ and $S'(m)$, $m \in \mathcal{D}(S)$, by

$$\mathcal{T}_m : L^\infty(\Omega) \cap L^2_{\text{comp}}(\Omega) \to L^2(\partial\Omega),\ h \mapsto \gamma S'(m)h.$$

Let $b \in L^2(\partial\Omega)$. We want to find a function $\delta m \in L^2(\Omega)$, such that

$$\mathcal{T}_m^* b = \delta m. \tag{2.61}$$

For that purpose, we will consider the standard L^2 inner product, such that for $\eta \in L^2(\Omega)$ we have

$$(\delta m, \eta)_{L^2(\Omega)\times L^2(\Omega)} = (\mathcal{T}_m^* b, \eta)_{L^2(\Omega)\times L^2(\Omega)} = (b, \mathcal{T}_m\eta)_{L^2(\partial\Omega)\times L^2(\partial\Omega)}.$$

Theorem 2.24. *There exists a $\phi \in H^1(\Omega)$, such that*

$$\mathcal{T}_m^* b = k_0^2 \cdot \overline{S(m)} \cdot \phi, \tag{2.62}$$

where $m \in \mathcal{D}(S)$. The function ϕ is uniquely determined as the solution of the adjoint problem

$$\Delta\phi + k_0^2(1 - \overline{m})\phi = 0 \qquad \text{in } \Omega, \tag{2.63}$$

$$\frac{\partial\phi}{\partial\mathbf{n}} + ik_0\phi = -b \qquad \text{on } \partial\Omega. \tag{2.64}$$

Proof. Let $w := S'(m)h = T_m h$. Consider the inner product $(\cdot,\cdot)_{L^2(\Omega)\times L^2(\Omega)}$ of equation (2.54) with some $\phi \in H^1(\Omega)$,

$$\int_\Omega \Delta w \overline{\phi}\ \mathrm{d}\mathbf{x} + k_0^2 \int_\Omega (1-m) w\overline{\phi}\ \mathrm{d}\mathbf{x} = k_0^2 \int_\Omega h \cdot u_{\mathrm{t}} \overline{\phi}\ \mathrm{d}\mathbf{x}, \tag{2.65}$$

where $u_{\mathrm{t}} := S(m)$ denotes the solution of the direct scattering problem (2.28) - (2.30).
With partial integration, we obtain from the first term

$$\begin{aligned}\int_\Omega \Delta w \overline{\phi}\ \mathrm{d}\mathbf{x} &= \int_{\partial\Omega} \frac{\partial w}{\partial \mathbf{n}} \overline{\phi}\ \mathrm{d}s_{\mathbf{x}} - \int_\Omega \nabla w \nabla \overline{\phi}\ \mathrm{d}\mathbf{x} \\ &= \int_{\partial\Omega} \frac{\partial w}{\partial \mathbf{n}} \overline{\phi}\ \mathrm{d}s_{\mathbf{x}} - \int_{\partial\Omega} w \frac{\partial \overline{\phi}}{\partial \mathbf{n}}\ \mathrm{d}s_{\mathbf{x}} + \int_\Omega w \Delta \overline{\phi}\ \mathrm{d}\mathbf{x}.\end{aligned}$$

By applying the boundary condition (2.48) of the linearized problem, this yields

$$\begin{aligned}\int_\Omega \Delta w \overline{\phi}\ \mathrm{d}\mathbf{x} &= \int_{\partial\Omega} ik_0 w \cdot \overline{\phi}\ \mathrm{d}s_{\mathbf{x}} - \int_{\partial\Omega} w \frac{\partial \overline{\phi}}{\partial \mathbf{n}}\ \mathrm{d}s_{\mathbf{x}} + \int_\Omega w \Delta \overline{\phi}\ \mathrm{d}\mathbf{x} \\ &= \int_{\partial\Omega} w \cdot \left(ik_0 \overline{\phi} - \frac{\partial \overline{\phi}}{\partial \mathbf{n}} \right) \mathrm{d}s_{\mathbf{x}} + \int_\Omega w \Delta \overline{\phi}\ \mathrm{d}\mathbf{x} \\ &= \int_{\partial\Omega} w \cdot \overline{\left(-ik_0 \phi - \frac{\partial \phi}{\partial \mathbf{n}} \right)}\ \mathrm{d}s_{\mathbf{x}} + \int_\Omega w \Delta \overline{\phi}\ \mathrm{d}\mathbf{x}.\end{aligned}$$

The second term of (2.65) is rewritten as

$$k_0^2 \int_\Omega (1-m) w \overline{\phi}\ \mathrm{d}\mathbf{x} = \int_\Omega w \overline{\big(k_0^2 (1-\overline{m})\phi\big)}\ \mathrm{d}\mathbf{x}.$$

By setting $\mathcal{T}_m^* b = k_0^2 \overline{u_{\mathrm{t}}} \phi$, the right-hand side of (2.65) yields

$$\begin{aligned}k_0^2 \int_\Omega h \cdot u_{\mathrm{t}} \overline{\phi}\ \mathrm{d}\mathbf{x} &= \int_\Omega h \cdot \overline{k_0^2 \overline{u_{\mathrm{t}}} \phi}\ \mathrm{d}\mathbf{x} \\ &= \big(h, k_0^2 \overline{u_{\mathrm{t}}} \phi\big)_{L^2(\Omega)\times L^2(\Omega)} \\ &= (h, \mathcal{T}_m^* b)_{L^2(\Omega)\times L^2(\Omega)} \\ &= (\mathcal{T}_m h, b)_{L^2(\partial\Omega)\times L^2(\partial\Omega)} \\ &= (w, b)_{L^2(\partial\Omega)\times L^2(\partial\Omega)} \\ &= \int_{\partial\Omega} w \overline{b}\ \mathrm{d}s_{\mathbf{x}}.\end{aligned}$$

All in all, by merging the above results we obtain

$$\int_\Omega w \cdot \overline{\big(\Delta\phi + k_0^2(1-\overline{m})\phi\big)}\ \mathrm{d}\mathbf{x} = 0$$

and

$$\int_{\partial\Omega} w \cdot \overline{\left(-ik_0 \phi - \frac{\partial \phi}{\partial \mathbf{n}} - b \right)}\ \mathrm{d}s_{\mathbf{x}} = 0.$$

As the solution w of the linearized scattering problem does generally not vanish on either Ω or its boundary $\partial\Omega$, ϕ fulfills the postulated boundary value problem from Theorem 2.24. The existence and uniqueness of ϕ can be derived by similar calculations as in the preceding section. ☐

Remark 2.25. *The above calculations yield the adjoint of the operator* $\mathcal{T}_m = \gamma S'(m)$*. The advantage of this approach is that the calculation of the adjoint of the trace operator is included in the adjoint operator of* $\mathcal{T}_m$*. We are interested in the evaluation of expressions of the form*

$$F'(m)^* z = \mathcal{T}_m^* Q^* z,$$

where Q *is the observation operator and* $z \in \mathbb{C}^N$ *contains information about the data* $y \in Y$*. In the following section, we will discuss the observation operator* Q *and give an explicit representation of its adjoint, such that we can easily obtain an expression of the form* $b = Q^* z$*, where* $b \in L^2(\partial\Omega)$*, and we can apply Theorem 2.24 for the numerical solution of our inverse problem of THz tomography.*

2.4.4. The observation operator in THz tomography

So far, we have discussed the mathematical description of the scattering map S and the trace operator γ. To complete the mathematical description of the direct problem of THz tomography, we have to deal with the measuring process, representing the generation of the data.
The observable is the electric field of the THz radiation. In the previous sections, we have discussed the choice of the domain Ω, which is defined by the arrangement of the measuring devices, i.e., the surfaces of the receivers. We assume they are segments of this circle and choose the boundary $\partial\Omega$ such that the surfaces of the receivers are contained in $\partial\Omega$. The domain Ω is defined as the interior of the circle, such that the closure of the support of the function m, which represents the complex refractive index, is contained in Ω.

Consequently, we first of all assume that the measured data are generated purely on $\partial\Omega$. Second, we assume the observation operator to be linear, as our main purpose in this work is the evaluation of the physical model, which is given by the scattering problem we analyzed in the previous sections. However, we take into account that the receivers have a certain width. We will not model the measuring process as a point evaluation, but rather take into account that each receiver generates a *mean value* of the electric field u_{t} over its surface. This definition allows an easy inclusion of the *sensor characteristic*, which refers to the property that different areas of the receiver register different, characteristic ratios of the field. For example, it is plausible that a receiver does not register the field around its sensor's edges as strongly as in the middle. This effect can be caused by reflections or other influences of the receiver. The generated data can thus be interpreted as weighted means over the sensors' surfaces.

In tomographic measurements, the object is usually illuminated from different positions to increase the number of data points and, by consequence, the information about the tested object. In the case of two-dimensional THz tomography, the tested object is fixed on a pivotable support, which moves along a rail in x-direction and rotates the object around a fixed axis. For the numerical reconstruction of a tested object's complex refractive index, we will assume that instead of the object, the measurement set-up is rotated and shifted around the object.

Remark 2.26. *During one measuring process, the set-up is shifted and rotated stepwise with step size* Δx *in* x*-direction, and* $\Delta\vartheta$ *around the rotation axis. Let* J_1 *be the number of angular positions* ϑ_{j_1}*,* $j_1 = 0, ..., J_1 - 1$*, and* $2J_2 + 1$ *be the number of positions* $d_{j_2} = j_2 \cdot \Delta x$*,* $j_2 = -J_2, ..., J_2$ *on the* x*-axis.*

In an effort to keep the notation as simple as possible, we make the following definition.

Definition 2.27. *The position of the measurement set-up is described by the tuple*

$$(\vartheta_{j_1}, d_{j_2}), \quad \vartheta_{j_1} \in [0, 2\pi], \ d_{j_2} \in [-x_m, x_m], \tag{2.66}$$

where $x_m \geq 0$ is the maximal distance to $x = 0$. The quantities that depend on the $J_1 \cdot (2J_2 + 1)$ different positions are indexed by elements of the set

$$\mathbf{J} := \Big\{ \mathbf{j} := (j_1, j_2) \ : \ j_1 \in \big\{0, ..., J_1 - 1\big\}, \ j_2 \in \big\{ -J_2, ..., J_2 \big\} \Big\}.$$

The rotation and shifting of the emitter-receiver set-up implicates in particular that the incident field depends on the current position $(\vartheta_{j_1}, d_{j_2})$ of the set-up. To keep the notation as simple as possible, we will denote the shifted incident field $u_{\mathrm{i}}(\vartheta_{j_1}, d_{j_2})$ and the resulting scattered field $u_{\mathrm{sc}}(\vartheta_{j_1}, d_{j_2})$ by

$$\begin{aligned} u_{\mathrm{i}}^{\mathbf{j}} &:= u_{\mathrm{i}}(\vartheta_{j_1}, d_{j_2}), \\ u_{\mathrm{sc}}^{\mathbf{j}} &:= u_{\mathrm{sc}}(\vartheta_{j_1}, d_{j_2}). \end{aligned}$$

Both emitter and receivers are not only situated at the boundary of the domain Ω. They rather define Ω, on which the complex refractive index m is supposed to be reconstructed. Thus, the whole domain Ω is shifted during a tomographic measurement and we write $\Omega^{\mathbf{j}}$ to underline the dependence on the position of the set-up.
For each $\mathbf{j} \in \mathbf{J}$ we have $\operatorname{supp}(m) \subseteq \Omega^{\mathbf{j}}$, and consequently

$$\operatorname{supp}(m) \subseteq \bigcap_{\mathbf{j} \in \mathbf{J}} \Omega^{\mathbf{j}}.$$

Accordingly, by

$$S^{\mathbf{j}} \ : \ \mathcal{D}(S^{\mathbf{j}}) \to H^1(\Omega^{\mathbf{j}}) \tag{2.67}$$

we will denote the operator that maps m to the resulting electric field $u_{\mathrm{t}}^{\mathbf{j}} = u_{\mathrm{i}}^{\mathbf{j}} + u_{\mathrm{sc}}^{\mathbf{j}}$ in $\Omega^{\mathbf{j}}$, where $u_{\mathrm{i}}^{\mathbf{j}}$ is the incident field generated by the emitter and $u_{\mathrm{sc}}^{\mathbf{j}}$ solves the boundary value problem

$$\Delta u_{\mathrm{sc}}^{\mathbf{j}} + k_0^2(1 - m) u_{\mathrm{sc}}^{\mathbf{j}} = k_0^2 m u_{\mathrm{i}}^{\mathbf{j}} \qquad \text{in } \Omega^{\mathbf{j}}, \tag{2.68}$$

$$\frac{\partial u_{\mathrm{sc}}^{\mathbf{j}}}{\partial \mathbf{n}} - i k_0 u_{\mathrm{sc}}^{\mathbf{j}} = 0 \qquad \text{on } \partial\Omega^{\mathbf{j}}. \tag{2.69}$$

Furthermore, we define the respective trace operator $\gamma^{\mathbf{j}}$ by

$$\gamma^{\mathbf{j}} \ : \ H^1(\Omega^{\mathbf{j}}) \to L^2(\partial\Omega^{\mathbf{j}}), \ \gamma^{\mathbf{j}} u_{\mathrm{t}}^{\mathbf{j}} = u_{\mathrm{t}}^{\mathbf{j}}|_{\partial\Omega^{\mathbf{j}}}. \tag{2.70}$$

For the definition of the observation operator, which depends likewise on the position of the tomograph, we will introduce the following notation. Furthermore, we assume that the emitter, which generates the incident THz radiation, not only serves as a source, but also as a receiver.

Definition 2.28. *Let $N \in \mathbb{N}$ denote the number of receivers. By*

$$E_\nu^{\mathbf{j}} \subseteq \partial\Omega^{\mathbf{j}}, \quad \nu = 1, ..., N,$$

we denote the surfaces of the N receivers. The sensor characteristic of the receiver $E_\nu^{\mathbf{j}}$ is a real valued function

$$e_\nu^{\mathbf{j}} \ : \ \partial\Omega^{\mathbf{j}} \to \mathbb{R}_+$$

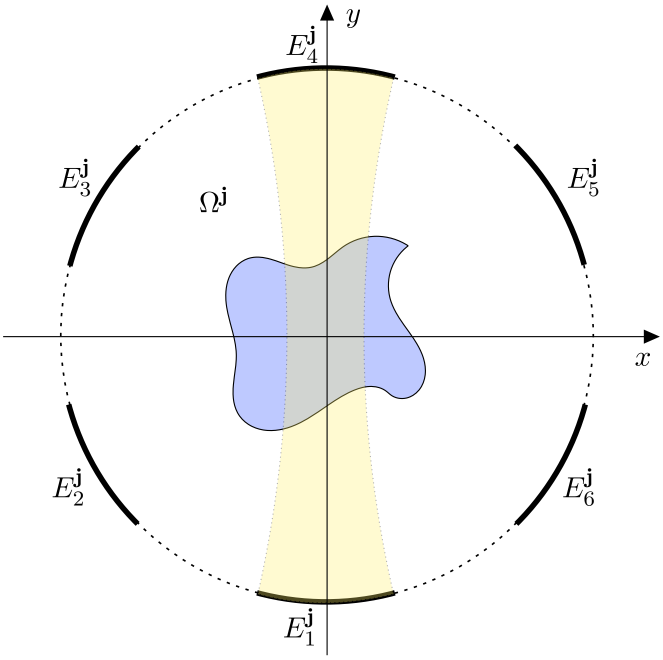

Figure 2.4.: Schematic representation of a THz tomograph with six receivers $E_\nu^{\mathbf{j}}$, $\nu = 1, ..., 6$, where the receiver $E_1^{\mathbf{j}}$ also serves as an emitter.

with

$$\operatorname{supp}(e_\nu^{\mathbf{j}}) \subseteq E_\nu^{\mathbf{j}}$$

and

$$e_\nu^{\mathbf{j}}(\mathbf{x}) \leq 1 \quad \text{for all } x \in \partial\Omega^{\mathbf{j}}.$$

Using this notation, we define the observation operator $Q^{\mathbf{j}}$.

Definition 2.29. *For each $\mathbf{j} \in \mathbf{J}$, the observation operator $Q^{\mathbf{j}}$ maps the (restricted) electric field $\gamma^{\mathbf{j}} w^{\mathbf{j}} \in L^2(\partial\Omega^{\mathbf{j}})$ to the measured values $\left(y_\nu^{\mathbf{j}}\right)_{\nu=1,\dots,N} \in \mathbb{C}^N$ by*

$$\begin{aligned} Q^{\mathbf{j}} \,:\, L^2(\partial\Omega^{\mathbf{j}}) &\rightarrow \mathbb{C}^N, \\ \gamma^{\mathbf{j}} w^{\mathbf{j}} &\mapsto y^{\mathbf{j}} := \left(\int_{\partial\Omega^{\mathbf{j}}} e_\nu^{\mathbf{j}}(\mathbf{x}) \gamma^{\mathbf{j}} w^{\mathbf{j}}(\mathbf{x}) \, \mathrm{d}s_{\mathbf{x}}\right)_{\nu=1,\dots,N}. \end{aligned} \tag{2.71}$$

Remark 2.30. *The observation operator $Q^{\mathbf{j}}$ from Definition 2.29 is a continuous linear operator. Therefore, $Q^{\mathbf{j}}$ is Fréchet differentiable (see, e.g., [76]) with Fréchet derivative*

$$\left(Q^{\mathbf{j}}\right)'(b) \,:\, L^2(\partial\Omega^{\mathbf{j}}) \rightarrow \mathbb{C}^N, q \mapsto \left(Q^{\mathbf{j}}\right)'(b) q = Q^{\mathbf{j}} q = \left(\int_{\partial\Omega^{\mathbf{j}}} e_\nu^{\mathbf{j}}(\mathbf{x}) q(\mathbf{x}) \, \mathrm{d}s_{\mathbf{x}}\right)_{\nu=1,\dots,N} \tag{2.72}$$

in $b \in L^2(\partial\Omega^{\mathbf{j}})$, evaluated at $q \in L^2(\partial\Omega^{\mathbf{j}})$.

Lemma 2.31. *The adjoint of the observation operator*

$$Q^{\mathbf{j}} \;:\; L^2(\partial\Omega^{\mathbf{j}}) \rightarrow \mathbb{C}^N, \; q \mapsto \left(\int_{\partial\Omega^{\mathbf{j}}} e_\nu^{\mathbf{j}}(\mathbf{x}) q(\mathbf{x}) \; \mathrm{d}s_{\mathbf{x}}\right)_{\nu=1,\dots,N}$$

is given by $(Q^{\mathbf{j}})^* : \mathbb{C}^N \to L^2(\partial\Omega^{\mathbf{j}})$*, where*

$$\beta = (\beta_\nu)_{\nu=1,\dots,N} \mapsto (Q^{\mathbf{j}})^*\beta = \sum_{\nu=1}^{N} \beta_\nu e_\nu^{\mathbf{j}}. \tag{2.73}$$

Proof. Let $\beta := (\beta_\nu)_{\nu=1,\dots,N} \in \mathbb{C}^N$ and $(L^2(\partial\Omega))^* \cong L^2(\partial\Omega)$. For $q \in L^2(\partial\Omega^{\mathbf{j}})$ we have

$$\left\langle Q^{\mathbf{j}}q, \beta \right\rangle_{\mathbb{C}^N \times \mathbb{C}^N} = \left\langle q, (Q^{\mathbf{j}})^*\beta \right\rangle_{L^2(\partial\Omega^{\mathbf{j}}) \times L^2(\partial\Omega^{\mathbf{j}})}, \tag{2.74}$$

using $(\mathbb{C}^N)^* \cong \mathbb{C}^N$. From

$$\begin{aligned}
\left\langle Q^{\mathbf{j}}q, \beta \right\rangle_{\mathbb{C}^N \times \mathbb{C}^N} &= \sum_{\nu=1}^{N} (Q^{\mathbf{j}}q) \cdot \overline{\beta_\nu} \\
&= \sum_{\nu=1}^{N} \left(\int_{\partial\Omega^{\mathbf{j}}} e_\nu^{\mathbf{j}}(\mathbf{x}) q(\mathbf{x}) \, \mathrm{d}s_{\mathbf{x}} \right) \cdot \overline{\beta_\nu} \\
&= \int_{\partial\Omega^{\mathbf{j}}} q(\mathbf{x}) \left(\sum_{\nu=1}^{N} \overline{\beta_\nu} e_\nu^{\mathbf{j}}(\mathbf{x}) \right) \, \mathrm{d}s_{\mathbf{x}} \\
&= \int_{\partial\Omega^{\mathbf{j}}} q(\mathbf{x}) \overline{\left(\sum_{\nu=1}^{N} \beta_\nu e_\nu^{\mathbf{j}}(\mathbf{x}) \right)} \, \mathrm{d}s_{\mathbf{x}} \\
&= \left\langle q, \sum_{\nu=1}^{N} \beta_\nu e_\nu^{\mathbf{j}} \right\rangle_{L^2(\partial\Omega^{\mathbf{j}}) \times L^2(\partial\Omega^{\mathbf{j}})}
\end{aligned}$$

we deduce

$$(Q^{\mathbf{j}})^*\beta = \sum_{\nu=1}^{N} \beta_\nu e_\nu^{\mathbf{j}}.$$

□

Remark 2.32. *Possible choices for the sensor characteristic are characteristic functions*

$$e_\nu^{\mathbf{j}} := \chi_{E_\nu^{\mathbf{j}}}$$

for all $\nu = 1, \dots, N$ *and* $\mathbf{j} \in \mathbf{J}$*, which will be our choice in the upcoming numerical experiments. Point evaluations are realized by setting*

$$e_\nu^{\mathbf{j}} := \delta(\mathbf{x} - \mathbf{x}_{E_\nu^{\mathbf{j}}}),$$

where the point $\mathbf{x}_{E_\nu^{\mathbf{j}}}$ *corresponds to the position of the respective receiver (see, e.g., [8]).*

2.5. Terahertz tomography: direct and inverse problem

The previous sections have been dedicated to a thorough analysis of the forward operator. Before proceeding to a numerical experiment, we want to summarize our findings and formulate the direct as well as the inverse problem explicitly, using the same notation as before. For all positions $\mathbf{j} \in \mathbf{J}$ of the tomograph, the forward operator

$$F^{\mathbf{j}} : \mathcal{D}(F^{\mathbf{j}}) \to \mathbb{C}^N, \; F^{\mathbf{j}}(m) = y^{\mathbf{j}} = \left(y_\nu^{\mathbf{j}}\right)_{\nu=1,\dots,N}, \tag{2.75}$$

where $\mathcal{D}(F^{\mathbf{j}}) := \mathcal{D}(S^{\mathbf{j}})$, is the composition

$$F^{\mathbf{j}} = Q^{\mathbf{j}} \circ \gamma^{\mathbf{j}} \circ S^{\mathbf{j}}$$

of the scattering map $S^{\mathbf{j}}$, the trace operator $\gamma^{\mathbf{j}}$, and the observation operator $Q^{\mathbf{j}}$.

Direct Problem 2.33. *Let $m \in \mathcal{D}(F^{\mathbf{j}})$ represent the given complex refractive index with* $\operatorname{supp}(m) \subseteq \Omega^{\mathbf{j}}$ *for all positions $\mathbf{j} \in \mathbf{J}$. The direct problem consists in the determination of the data*

$$y^{\mathbf{j}} := F^{\mathbf{j}}(m) = \left(y_\nu^{\mathbf{j}}\right)_{\nu=1,\dots,N} \tag{2.76}$$

from the knowledge of the complex refractive index m (and the incident field $u_{\mathrm{i}}^{\mathbf{j}}$), where N is the number of receivers of the tomograph, for all $\mathbf{j} \in \mathbf{J}$.

In the context of nondestructive testing, we are mainly interested in the respective inverse problem, which is the reconstruction of the function m, where

$$\operatorname{supp}(m) \subseteq \bigcap_{\mathbf{j} \in \mathbf{J}} \Omega^{\mathbf{j}},$$

from measurements of the total electric field u_{t} on the respective boundary of $\Omega^{\mathbf{j}}$ for different positions $\mathbf{j} \in \mathbf{J}$ of the tomograph (emitter and receivers). In particular, we assume the given data to be perturbed.

Definition 2.34. *We denote noisy data by $y^{\mathbf{j},\delta}$, where δ refers to the* noise level *given by*

$$\left\| y^{\mathbf{j}} - y^{\mathbf{j},\delta} \right\| \leq \delta \tag{2.77}$$

for all $\mathbf{j} \in \mathbf{J}$.

Inverse Problem 2.35. *Given exact data $y^{\mathbf{j}} = \left(y_\nu^{\mathbf{j}}\right)_{\nu=1,\dots,N}$ or noisy data $y^{\mathbf{j},\delta} = \left(y_\nu^{\mathbf{j},\delta}\right)_{\nu=1,\dots,N}$ from the tomograph's N receivers in the positions $\mathbf{j} \in \mathbf{J}$, we want to recover the complex refractive index m such that*

$$F^{\mathbf{j}}(m) = y^{\mathbf{j}}. \tag{2.78}$$

Regarding a numerical solution of the inverse problem, particularly with a Landweber method or via sequential subspace optimization, we are required to evaluate the gradient $g^{\mathbf{j}}$ of the least squares functional

$$\Psi^{\mathbf{j},\delta}(m) := \frac{1}{2} \left\| F^{\mathbf{j}}(m) - y^{\mathbf{j},\delta} \right\|^2, \tag{2.79}$$

which is given by

$$g^{\mathbf{j}}(m) := \left(F^{\mathbf{j}}\right)'(m)^* \left(F^{\mathbf{j}}(m) - y^{\mathbf{j},\delta}\right), \tag{2.80}$$

in the current iterate m_n^δ. We have derived all the tools we need to calculate $g^{\mathbf{j}}(m)$ for some $m \in \mathcal{D}(F^{\mathbf{j}})$. For the adjoint $\left(F^{\mathbf{j}}\right)'(m)^*$ of the linearized forward operator $\left(F^{\mathbf{j}}\right)'(m)$, we first want to state the following lemma.

Lemma 2.36. *The Fréchet derivative of the forward operator* $F^{\mathbf{j}}$ *in* $m \in \mathcal{D}(F^{\mathbf{j}})$ *fulfills*

$$\left[(F^{\mathbf{j}})'(m)\right] h = \left(Q^{\mathbf{j}}\gamma^{\mathbf{j}}(S^{\mathbf{j}})'(m)\right) h \tag{2.81}$$

for all $h \in L^{\infty}(\Omega^{\mathbf{j}}) \cap L^2_{\text{comp}}(\Omega^{\mathbf{j}})$*.*

Proof. We apply the chain rule ([76], Theorem III.5.4(d)) for the Fréchet derivative. Together with the linearity of the observation operator $Q^{\mathbf{j}}$ and the trace operator $\gamma^{\mathbf{j}}$ we obtain

$$\begin{aligned}\left[(F^{\mathbf{j}})'(m)\right] h &= \left[(Q^{\mathbf{j}}\gamma^{\mathbf{j}}S^{\mathbf{j}})'(m)\right] h \\ &= \left[(Q^{\mathbf{j}})'\big(\gamma^{\mathbf{j}}S^{\mathbf{j}}(m)\big) \circ (\gamma^{\mathbf{j}})'\big(S^{\mathbf{j}}(m)\big) \circ (S^{\mathbf{j}})'(m)\right] h \\ &= \left[Q^{\mathbf{j}} \circ \gamma^{\mathbf{j}} \circ (S^{\mathbf{j}})'(m)\right] h\end{aligned}$$

for all $h \in L^{\infty}(\Omega^{\mathbf{j}}) \cap L^2_{\text{comp}}(\Omega^{\mathbf{j}})$. □

Consequently, the adjoint of the linearization of the forward operator in $m \in \mathcal{D}(F^{\mathbf{j}})$ is an operator of the form

$$\left((F^{\mathbf{j}})'(m)\right)^* \;:\; \mathbb{C}^N \to L^2(\Omega^{\mathbf{j}}),\; \beta \mapsto \left[\left((S^{\mathbf{j}})'(m)\right)^* \gamma^* \left(Q^{\mathbf{j}}\right)^*\right] \beta. \tag{2.82}$$

Lemma 2.37. *Let* $\beta = (\beta_\nu) \in \mathbb{C}^N$*,* $N \in \mathbb{N}$*, and* $\delta m^{\mathbf{j}} \in L^2(\Omega^{\mathbf{j}})$ *with*

$$\delta m^{\mathbf{j}} := \left((F^{\mathbf{j}})'(m)\right)^* \beta.$$

Then we have

$$\delta m^{\mathbf{j}} = k_0^2 \overline{S^{\mathbf{j}}(m)} \cdot \phi^{\mathbf{j}}, \tag{2.83}$$

where $\phi^{\mathbf{j}} \in H^1(\Omega^{\mathbf{j}})$ *is the weak solution of the boundary value problem*

$$\begin{aligned}\Delta\phi^{\mathbf{j}} + k_0^2(1-\overline{m})\phi^{\mathbf{j}} &= 0 && \text{in } \Omega^{\mathbf{j}}, \\ \frac{\partial\phi^{\mathbf{j}}}{\partial\mathbf{n}} + ik_0\phi^{\mathbf{j}} &= -\sum_{\nu=1}^{N} e^{\mathbf{j}}_\nu \cdot \beta_\nu && \text{on } \partial\Omega^{\mathbf{j}}.\end{aligned} \tag{2.84}$$

Proof. Theorem 2.24 together with Lemma 2.31 directly yields the desired statement. □

Consider the residual

$$R^{\mathbf{j},\delta}(m) = \left(R^{\mathbf{j},\delta}_\nu(m)\right)_{\nu=1,\dots,N} := \left(F^{\mathbf{j}}(m)_\nu - y^{\mathbf{j},\delta}_\nu\right)_{\nu=1,\dots,N} \tag{2.85}$$

in $m \in \mathcal{D}(F^{\mathbf{j}})$. We obtain the gradient

$$g^{\mathbf{j}}(m) = \left((F^{\mathbf{j}})'(m)\right)^* R^{\mathbf{j},\delta}(m)$$

by solving the partial differential Helmholtz equation

$$\Delta\phi^{\mathbf{j}} + k_0^2(1-\overline{m})\phi^{\mathbf{j}} = 0 \quad \text{in } \Omega^{\mathbf{j}} \tag{2.86}$$

with the Robin boundary condition

$$\frac{\partial \phi^{\mathbf{j}}}{\partial \mathbf{n}} + ik_0\phi^{\mathbf{j}} = -\sum_{\nu=1}^{N} e_\nu^{\mathbf{j}} \cdot \left(R^{\mathbf{j},\delta}\right)_\nu \quad \text{on } \partial\Omega^{\mathbf{j}} \tag{2.87}$$

and setting

$$g^{\mathbf{j}}(m) = k_0^2\overline{S^{\mathbf{j}}(m)} \cdot \phi^{\mathbf{j}}. \tag{2.88}$$

Remark 2.38. *We conclude the theory by some remarks.*

(a) The noise free case is treated analogously by setting $\delta = 0$.

(b) In order to calculate the gradient, two boundary value problems have to be solved: the forward problem $F^{\mathbf{j}}(m)$ to obtain the residual $R^{\mathbf{j},\delta}$, and the adjoint problem. The forward problem basically consists of calculating $S^{\mathbf{j}}(m)$, which should be reused in the evaluation of the adjoint problem (see (2.88)*) to avoid unnecessary numerical cost. However, for this reason the numerical effort to calculate $\big((F^{\mathbf{j}})'(m)\big)^*\beta$ for an arbitrary $\beta \in \mathbb{C}^N$ is comparable to the effort for the calculation of $g^{\mathbf{j}}(m)$.*

The inverse problem of THz tomography is treated as a nonlinear ill-posed problem. The ill-posedness of scattering type problems has been discussed multiple times, see, e.g., [18, 20, 41, 45]. Both Landweber and SESOP methods, in combination with Morozov's discrepancy principle, yield regularization techniques to compensate the instability of a direct inversion of the forward operator.

In preparation of a first numerical example, it is important to discuss our approach in THz tomography. We have mentioned before that we restrict ourselves to the lower frequency range of the THz spectrum in order to complement the research that has been conducted by Tepe et al. in cooperation with the Plastics Center in Würzburg ([51, 71]). Due to the relatively low frequencies of 0.07 - 0.1 THz, the wave character of the THz radiation is more prominent than in the higher frequency range, such that it is convenient to consider a model based on electromagnetic scattering. In the following section, we will discuss the numerical solution of the inverse problem of THz tomography from the knowledge of noisy synthetic data using the Landweber method. However, in our example we use an electromagnetic Gaussian beam with a frequency $f = 2.5 \cdot 10^{10}$, which belongs to the microwave spectrum. The reason is the high numerical cost when evaluating the two boundary value problems in order to obtain the gradient $g^{\mathbf{j}}$ for each position $\mathbf{j} \in \mathbf{J}$ of the tomograph. In a Landweber iteration, each step thus requires $2 \cdot |\mathbf{J}|$ such evaluations per iteration. For higher frequencies, it is thus reasonable to use a faster reconstruction method.
In a further numerical experiment in Chapter 3, we use electromagnetic radiation in the THz range (0.1 THz) for the testing and sequential subspace optimization methods for the reconstruction. However, it is necessary to adapt our SESOP methods for applications in complex Hilbert spaces, which is also done in Chapter 3.

2.6. Numerical reconstructions with the Landweber method

Now we have all ingredients to solve the inverse problem of THz tomography, we will continue with a first numerical test. To begin with, the forward problem is implemented to generate synthetic data with a known noise level δ. These data are used to find a solution of the inverse problem with the nonlinear Landweber method.

The Landweber method is one of the most commonly used methods in inverse problems. In the following, we give a short overview of the nonlinear Landweber method. Consider a nonlinear inverse problem

$$F(x) = y,$$

where $F : \mathcal{D}(F) \subseteq X \to Y$ is a nonlinear, continuous and Fréchet differentiable operator between Hilbert spaces X and Y. We assume that only noisy data y^δ with a noise level δ are given. If F and its Fréchet derivative F' fulfill some additional properties (similar to the ones we postulated for the analysis of the SESOP methods in Section 1.2), the Landweber iteration, together with a suitable stopping criterion, is a regularizing method to reconstruct the source x, see [39, 43, 63] for a detailed analysis. In particular, the discrepancy principle yields a finite stopping index [39]. The nonlinear Landweber iteration is given by

$$x_{n+1}^\delta = x_n^\delta - \omega F'(x_n^\delta)^* \left(F(x_n^\delta) - y^\delta \right), \tag{2.89}$$

where $\omega > 0$ is a relaxation parameter. The discrepancy principle is fulfilled at iteration n_*, when

$$\left\| F\left(x_{n_*}^\delta\right) - y^\delta \right\| \leq \tau\delta < \left\| F\left(x_n^\delta\right) - y^\delta \right\| \tag{2.90}$$

for all $n < n_*$, where $\tau > 1$ is fixed.

In the case of exact data, we set $\delta = 0$ and use the same iteration as for noisy data. An analysis is found in [39].

Instead of (2.89), we write

$$\begin{aligned} x_{n+1}^\delta &= x_n^\delta - \omega F'\left(x_n^\delta\right)^* R_n^\delta \\ &= x_n^\delta - \omega g_n^\delta, \end{aligned} \tag{2.91}$$

where we denote the current residual by

$$R_n^\delta := F\left(x_n^\delta\right) - y^\delta$$

and the current gradient (i.e., the gradient of the least squares functional evaluated at the current iterate x_n^δ) by

$$g_n^\delta := \nabla\Big(\frac{1}{2}\|F(x) - y^\delta\|^2\Big)\Big|_{x=x_n^\delta}.$$

The gradient g_n^δ can be interpreted as a search direction: The new iterate is found in the half-line that is spanned from the current iterate x_n^δ by $-g_n^\delta$.

Obviously, in each step of the Landweber iteration two major evaluations are necessary: first of all the evaluation of the direct problem $F\left(x_n^\delta\right)$, which in turn yields the residual R_n^δ, and subsequently the application of the adjoint of the Fréchet derivative $F'\left(x_n^\delta\right)^*$ in R_n^δ. Regarding the inverse problem of THz tomography, each of these evaluations consists of the solution of a boundary value problem. A standard method to solve boundary value problems is the *Finite Element Method* (FEM), where the solution is calculated on a triangularization of the domain Ω. The triangles, or finite elements, have a maximal element size $h_{\max}$ that depends on the radiation's wave length. A general rule is to choose $h_{\max}$ in the range of a tenth of the wave length to obtain a solution with a sufficient accuracy [1]. A higher frequency of the radiation that is used for testing involves a finer mesh and, consequently, a higher computational cost for the numerical solution of the boundary value problem.

In order to reduce the computational cost, we will restrict ourselves to a purely rotating tomograph, such that we can work with a fixed domain $\Omega \equiv \Omega^{\mathbf{j}}$ for all $\mathbf{j} \in \mathbf{J}$ that is independent of the tomograph's position. We simplify our notation from the previous section by

$$\mathbf{J} = \{j = 1, ..., J\},$$

where J is the total number of (angular) positions $\vartheta^j = (j-1) \cdot h_\vartheta$ of the tomograph, which is rotated in equidistant steps $h_\vartheta := \frac{2\pi}{J}$. The incident field u_{i}^j depends on the angle ϑ^j and is obtained from the initial position (2.20) by the rotation transformation

$$t_{\vartheta^j} : \begin{pmatrix} x \\ y \end{pmatrix} \mapsto \begin{pmatrix} \cos(\vartheta^j) & \sin(\vartheta^j) \\ -\sin(\vartheta^j) & \cos(\vartheta^j) \end{pmatrix} \cdot \begin{pmatrix} x \\ y \end{pmatrix},$$

such that

$$u_{\mathrm{i}}^j(x,y) = u_{\mathrm{i}}^0\left(t_{\vartheta_j}(x,y)\right).$$

The dependence of the forward operator F^j on the position of the tomograph has to be taken into account before we proceed to the implementation. There is a variety of problems where the forward operator depends on an additional parameter, which is not necessarily a position. An alternative is for example the frequency of the respective radiation, see [7], where the spatial frequency of the radiation is varied during the measurements.

In any case, the result is a system of (nonlinear) operator equations

$$F^j(x) = y^j, \quad j = 1, ..., J. \tag{2.92}$$

There are several methods that take into account the dependence of F on some additional discrete parameter. A well-known method is Kaczmarz's method, which has been applied successfully in computerized tomography [57]. The combination of Kaczmarz's method with the Landweber method for the solution of nonlinear inverse problems has been addressed by Haltmeier et al. in [36, 37], a combination with Newton methods is presented by Burger and Kaltenbacher in [13].

In this work, we are dealing with parameter-to-solution operators, whose evaluation is numerically expensive. For this reason, we are interested in a parallel evaluation of the occurring operators. Methods based on the Kaczmarz method are not suited for parallelization, such that we apply a different approach.

For each position $j \in \mathbf{J}$, we obtain one gradient $g^{j,\delta}$ belonging to the respective equation (2.92). As the data $y^{j,\delta}$ from each position $j \in \mathbf{J}$ should contribute in equal measure to the reconstruction of the function x, it is sensible to use the average (or mean) of all available gradients in each Landweber step. We thus define

$$g_n^\delta := \frac{1}{J}\sum_{j=1}^{J} g_n^{j,\delta} = \frac{1}{J}\sum_{j=1}^{J} \left(F^j\right)'(x_n^\delta)^* \left(F^j(x_n^\delta) - y^{j,\delta}\right) \tag{2.93}$$

and obtain a search direction for the Landweber iteration (2.89).

Remark 2.39. *The approach to use the average of the gradients can be interpreted as a numerical integration of the search directions $g_n^{j,\delta}$ over the angle ϑ of rotation. Apart from the factor 2π, the above sum corresponds to the approximation of this integral by the trapezoidal rule, which is specially suited for the numerical integration of trigonometric functions. Solutions of the Helmholtz equations depend on the boundary values. Yet, in many cases, they are combinations of trigonometric functions, which motivates the use of the trapezoidal rule.*

We now return to the inverse problem of THz tomography. The data that are generated by the tomograph during one measurement are assembled in a matrix. We have

$$y^\delta = \left(y^{j,\delta}\right)_{j=1,\ldots,J} = \begin{pmatrix} y_1^{1,\delta} & \cdots & y_1^{J,\delta} \\ \vdots & \ddots & \vdots \\ y_N^{1,\delta} & \cdots & y_N^{J,\delta} \end{pmatrix} \in \mathbb{C}^{N\times J}.$$

It is essential to combine the norm in the data space Y with the procedure of averaging over the search directions corresponding to the tomograph's positions. First, each data point is afflicted by noise with a fixed noise level, ideally independent of the current position. The noise level is not, however, dependent on the number of different positions of the tomograph, such that the norm that is used to determine the noise level should not be influenced by J. Second, the norm in the data space Y is induced by the inner product, which in $\mathbb{C}^N$ is the standard scalar product. We postulate that the noise level fulfills

$$\max_{j=1,\ldots,J} \left\| y^{j,\delta} - y^j \right\|_{\mathbb{C}^N} \leq \delta.$$

For the discrepancy principle, we set

$$\left\| R_n^\delta \right\| = \left\| F(x_n^\delta) - y^\delta \right\| := \max_{j=1,\ldots,J} \left\| F^j(x_n^\delta) - y^{j,\delta} \right\|_{\mathbb{C}^N}, \tag{2.94}$$

in accordance with our averaged Landweber method.

For the generation of synthetic data $y^j = \left(y_\nu^j\right)_{\nu=1,\ldots,N}$, the direct problem has to be solved for a known complex refractive index m. We thus want to calculate

$$y^j = F^j(m) \in \mathbb{C}^N$$

numerically. The operator F^j is evaluated in two steps. The first step is to determine $S^j(m) = u_{\mathrm{t}}^j$, i.e., to solve the scattering problem

$$\begin{aligned} \Delta u_{\mathrm{sc}}^j + k_0^2(1-m)u_{\mathrm{sc}}^j &= k_0^2 m u_{\mathrm{i}}^j && \text{in } \Omega, \\ \frac{\partial u_{\mathrm{sc}}^j}{\partial \mathbf{n}} - ik_0 u_{\mathrm{sc}}^j &= 0 && \text{on } \partial\Omega, \\ u_{\mathrm{sc}}^j + u_{\mathrm{i}}^j = u_{\mathrm{t}}^j &= S^j(m), \end{aligned} \tag{2.95}$$

with the help of the *Finite Element Method (FEM)*, see for example [11, 34] for reference. In this work, we use a FEM solver which is available in Matlab (elliptic partial differential equations are solved with `assempde` in version R2015a; this solver uses linear basis functions). The FEM mesh is generated by a Matlab function and the maximal element size of the triangles is determined by the wave number k_0: In order to get a decent solution, the maximal element size must not be larger than a tenth of the wavelength of the electromagnetic radiation (the Gaussian beam). As a consequence, the effort that is needed to solve two-dimensional problems such as (2.95) grows quadratically with the wave number.

In the course of the measurement, the emitter and the receivers are rotated on a circle around the object. Accordingly, Ω is chosen as a two-dimensional disk and the surfaces E_ν^j of the receivers in position $j \in \mathbf{J}$ are thus parameterized as arcs on $\partial\Omega$. The value that is measured by receiver E_ν^j in position $j \in \mathbf{J}$ is obtained by a numerical integration over E_ν^j of the restriction of the total field

u_t^j to $\partial\Omega$ (i.e., we choose the sensor characteristic $e_\nu^j := \chi_{E_\nu^j}$). This corresponds to the numerical realization of the observation operator Q^j in combination with the trace operator γ^j, see also Definition 2.29. For that purpose, we use the trapezoidal rule. We define an equidistant grid in the respective arc for the numerical integration, where the step size is chosen of the same order as the maximal element size of the FEM mesh. The values on the grid points are obtained by interpolation from the total field on the FEM mesh.
The adjoint problem is solved in a similar way on the same FEM mesh as the forward problem.

Remark 2.40. *The numerical evaluation of the observation operator naturally yields a certain noise level: The numerical integration of* u_t^j *over a sensor* E_ν^j *is realized with the help of the trapezoidal rule. The respective grid points thus have to be located within the triangularized domain. Accordingly, we choose the domain's radius slightly larger (about a half of the maximal element size) than the radius of the circle that contains the receivers, such that we have to accept a certain error in the data and a consideration of exact synthetic data is not possible. The use of finite elements also causes the smoothed outer interfaces of the tested object, which is clearly visible in Figure 2.7. This smoothing becomes less prominent when finer meshes are used, which is necessary when dealing with higher frequencies in the THz range.*

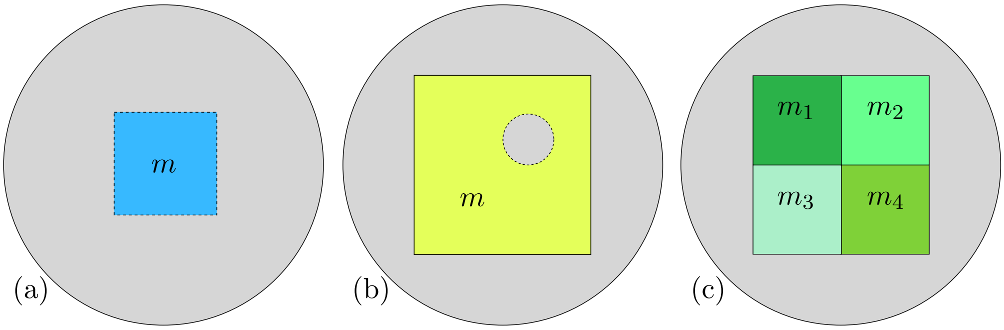

Figure 2.5.: Schematic representation of relevant test objects; (a) objects with unknown outer boundaries, (b) objects with known outer boundaries and an unknown defect inside, (c) objects that consist of different materials

We have remarked before that there are various properties of objects we would like to identify with the help of a THz tomographic examination. In Figure 2.5, a selection of possible test objects is given, representing the identification of (inner or outer) interfaces, defects, and compositions of materials.

As a representative test object for our numerical example, we choose a plastic block with quadratic cross section and known outer boundaries. The object has two inhomogeneities, a hole and an inclusion of some material with a higher refractive index and a higher absorption coefficient. Furthermore, the complex refractive index of the block itself is unknown. For the reconstruction, we use the knowledge of the object's outer interfaces, but assume that no information about the inside of the object is given. By recovering m we want to identify and classify the inclusions and also the material of the block.

Remark 2.41. *There are many parameters (geometry of the receivers, beam parameters such as beam waist or Rayleigh zone) in the forward model and also in the reconstruction algorithm (relaxation parameter) that need to be chosen. For this reason, a lot of testing is necessary to determine reasonable values for these parameters. The costly evaluations of the two boundary value* *problems and the relatively small wave length turn this into a time-consuming process. The following results might thus be improved by researching the parameters extensively.*

The goal of this numerical experiment is to obtain a first impression of the performance of a standard reconstruction technique (the Landweber method) when applying it to the inverse problem of THz tomography. As we have remarked before, the computational cost to numerically calculate the gradient increases quadratically with the reciprocal of the maximal element size of the FEM mesh. As the Landweber method is known to be relatively slow, we choose a low frequency $f = 2.5 \cdot 10^{10}$ Hz for the Gaussian beam that we use in this experiment. The tested object is a plastic block with two inclusions. $\mathrm{Re}(m)$ and $\mathrm{Im}(m)$ of the original block's material is presented in Figure 2.6. The block itself has the complex refractive index

$$m_1 = 1 - (1.5 + i \cdot 0.005)^2 = -1.249975 - i \cdot 0.015.$$

The inclusion in the top right corner is a hole filled with air, such that we can assume that its complex refractive index is identical to $m_2 \equiv 0$. The other inclusion in the middle of the lower half is some unknown material with a higher optical density, we choose

$$m_3 = 1 - (1.8 + i \cdot 0.02)^2 = -2.2396 - i \cdot 0.072.$$

Parameter	**Value**
Frequency f	$2.5 \cdot 10^{10}$ Hz
Beam waist W_0	0.015 m
Rayleigh zone y_0	0.02 m
Number of receivers N	20
Number of positions J	180
Relaxation parameter ω	0.08

Table 2.1.: Parameters of the numerical Landweber experiment

This example includes the localization and identification of unknown inner interfaces and different values of m.

For the reconstruction, we generate perturbed data with a signal-to-noise ratio of 2 %. In order to take into account the interpolation error from the evaluation of the observation operator, see Remark 2.40, we choose the noise δ slightly larger than $\max_{j=1,\dots,J} \|y^j - y^{j,\delta}\|$. The other relevant parameters are listed in Table 2.1.

We work on the domain

$$\Omega := \left\{ \mathbf{x} \in \mathbb{R}^2 \, : \, \|\mathbf{x}\|_2^2 \leq (0.04\mathrm{m})^2 \right\}.$$

As we assume the outer boundaries of the object to be known, we set the starting value as

$$m_0(\mathbf{x}) = (-1 - i \cdot 0.001) \cdot \chi_D(\mathbf{x}),$$

where

$$D := \{ \mathbf{x} \in \Omega \, : \, -0.015\,\mathrm{m} \leq x, y \leq 0.015\,\mathrm{m} \}$$

represents the cross section and ∂D the known outer interfaces of the tested block. The function m of the tested object is plotted in Figure 2.6.

The Landweber iteration is stopped at iteration n_* by the discrepancy principle (2.94). For later convenience, we choose $\tau = 20$. In Table 2.2, the key data of this reconstruction is presented.

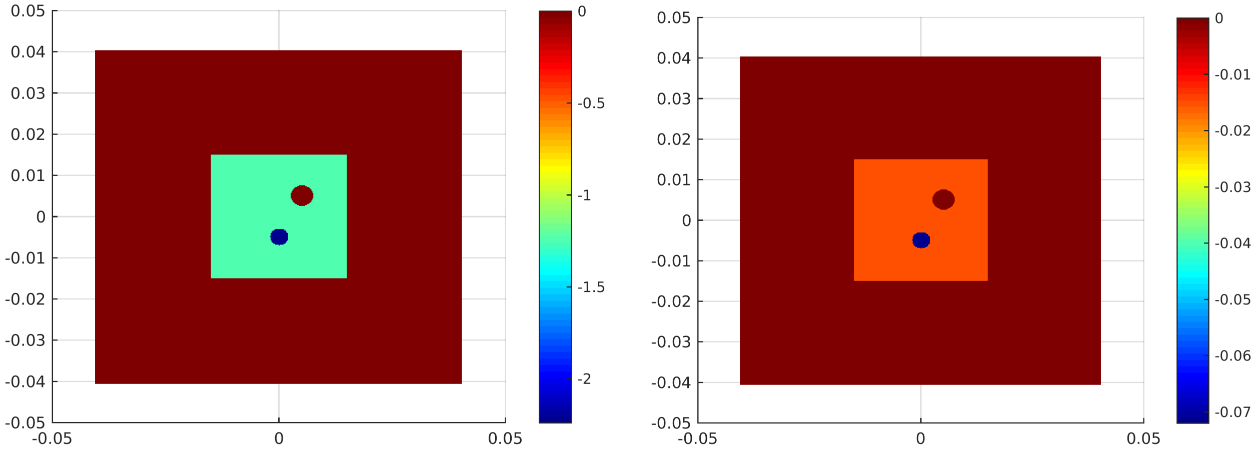

(a) **(b)**

Figure 2.6.: Real (a) and imaginary (b) part of the test object's complex refractive index m.

The approximated solution $m_{n_*}^{\delta}$ is presented in Figure 2.7. We note that the real part of m is reconstructed quite satisfactorily, with a relative error of 9.18 %, while the reconstruction of the imaginary part is rather bad with a relative error of over 100 %. The reason will be discussed in the following chapter. Yet, it is possible to draw qualitative conclusions from the reconstructed imaginary part $\mathrm{Im}(m_{n_*}^{\delta})$: The peaks in the plot of the reconstructed imaginary part indicate the position of the inclusions. It is however not possible to draw any conclusions on the materials of the inclusions, particularly not on the hole filled with air.

Number of iterations n_*	155
Execution time	6 h 38 min 49 s
Relative error in reconstructed real part $\mathrm{Re}(m)$	9.18 %
Relative error in reconstructed real part $\mathrm{Im}(m)$	164.31 %

Table 2.2.: Some key data to evaluate the performance of the nonlinear Landweber method at the identification of the complex refractive index of the tested object using a Gaussian beam with a microwave frequency $f = 2.5 \cdot 10^{10}$ Hz.

This experiment shows that it is possible to draw conclusions on the properties of some dielectric object from synthetic measurements of the resulting electric field on the boundary of the respective domain Ω. The real part of m is well reconstructed, whereas the reconstruction of the imaginary part allows only the localization of defects. The Landweber method as a reconstruction technique has been proven to be a stable regularizing method for our inverse problem. Nevertheless, this method is comparatively slow, keeping in mind that we used a frequency well below the THz range. In fact, it is important to note that an evaluation of our inverse problem with the Landweber method as above takes several days, if not weeks, when the frequency of the used radiation is at least 0.1 THz. Numerical tests with the Landweber method at $f = 0.1$ THz were stopped after three weeks of calculating without reasonable results. A better choice of the occurring parameters, such as the relaxation parameter, might lead to better results, but the reconstruction time will remain roughly in the range of several days.

In order to economically evaluate our model with respect to the parameter choice and particularly for the testing with THz radiation, a faster algorithm is highly desirable. We have seen in Section 1.4 that sequential subspace optimization methods yield promising results regarding their

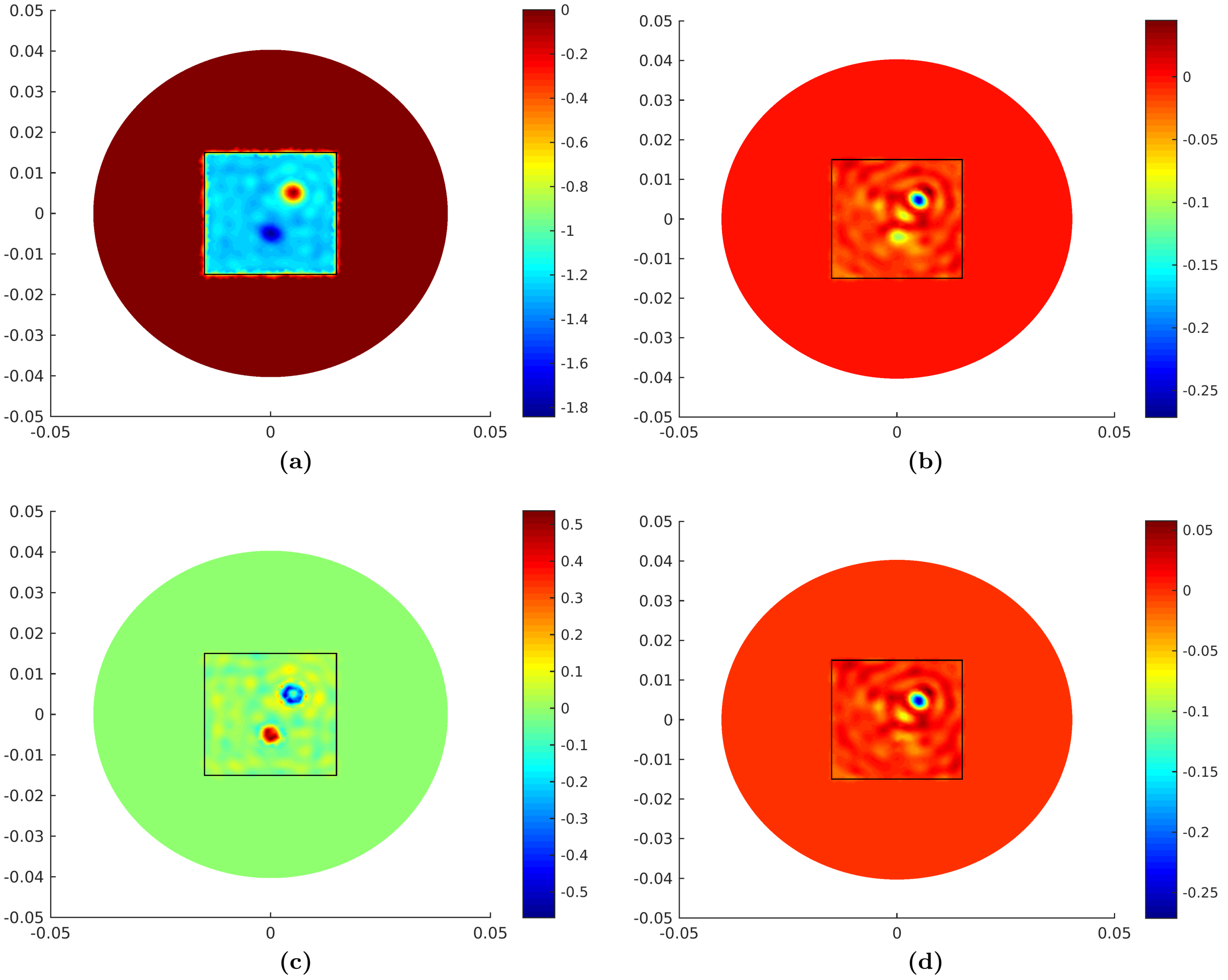

Figure 2.7.: Reconstruction $m^{\delta}_{n_*}$ of real (a) and imaginary (b) part of the complex refractive index m after 155 Landweber steps and the respective error in the reconstruction $m - m^{\delta}_{n_*}$ ((c) real part and (d) imaginary part).

performance in comparison to the Landweber method. We therefore adapt our SESOP methods to solve nonlinear inverse problems in complex Hilbert spaces and give a numerical example for a tomographic testing of a similar object with a Gaussian beam of frequency $f = 0.1\,\mathrm{THz}$.

3. Sequential subspace methods in complex Hilbert spaces and numerical reconstructions of the complex refractive index

In the previous section, we have seen that a reconstruction of m from noisy (discrete) boundary data with a nonlinear Landweber method yields promising results. The time that is needed to perform such a reconstruction is however quite long due to the expensive evaluations of the two boundary value problems per iteration and per position of the tomograph. In addition, the relaxation parameter ω has to be chosen very small to obtain useful results for the imaginary part of m. A thorough evaluation of our model to determine the optimal tomographic setup regarding the minimal number of receivers, their placement, or the optimal beam geometry would be facilitated by using a faster algorithm.
In Section 1.4 we have seen that our sequential subspace optimization methods significantly reduce the computation time to perform reconstructions, such that we will transfer these ideas to develop a method that is suited for the solution of inverse problems in complex Hilbert spaces. The main obstacle at a direct implementation of our subspace methods is the lack of a total order in the ground field $\mathbb{C}$ of the Hilbert spaces we consider. This becomes obvious when looking at Algorithm 1.21 with two search directions: In step (ii) we have to determine whether the intermediate iterate $\tilde{x}_{n+1}^{\delta}$ is situated above, below, or inside the stripe that belongs to the previous gradient. For this, we need the ground field to be ordered.

We begin with a discussion of the necessary adaptions and introduce a method based on Algorithm 1.21. The methods are analyzed and later applied to solve the inverse problem of THz tomography as modeled in the previous chapter.

3.1. Sequential subspace optimization in complex Hilbert spaces

Let X, Y be real Hilbert spaces with ground field $\mathbb{R}$. Define the complex Hilbert spaces X^{c} and Y^{c} as complexifications of X resp. Y with ground field $\mathbb{C}$. Now let $F : X^{\mathrm{c}} \to Y^{\mathrm{c}}$ be a nonlinear operator with domain $\mathcal{D}(F) \subseteq X^{\mathrm{c}}$. We consider the inverse problem

$$F(x) = y \tag{3.1}$$

and assume that noisy data fulfill $\left\|y - y^{\delta}\right\| \leq \delta$. Furthermore, we assume that F is continuous and Fréchet differentiable in a ball $B_{\rho}(x_0) \subseteq \mathcal{D}(F)$ with radius $\rho > 0$ around $x_0 \in X^{\mathrm{c}}$.
For each function $x \in X^{\mathrm{c}}$ and $y \in Y^{\mathrm{c}}$, we have $\mathrm{Re}(x), \mathrm{Im}(x) \in X$ and $\mathrm{Re}(y), \mathrm{Im}(y) \in Y$.

In the following, we will consider only noisy data. The respective methods and statements for noise-free data are obtained by setting $\delta = 0$. We will use the discrepancy principle as a stopping rule. In the noise-free case, it can be replaced by defining a maximal number of iterations. In addition, we restrict ourselves to the use of gradients as search directions.

The inverse problem (3.1) is to be solved iteratively by

$$x_{n+1}^{\delta} = x_n^{\delta} - \sum_{l \in I_n^{\delta}} \left(t_{n,l}^{\mathrm{r},\delta} \cdot \mathrm{Re}\big(g_l^{\delta}\big) + t_{n,l}^{\mathrm{i},\delta} \cdot \mathrm{Im}\big(g_l^{\delta}\big) \right), \tag{3.2}$$

where $t_{n,l}^{\mathrm{r},\delta}$, $t_{n,l}^{\mathrm{i},\delta} \in \mathbb{R}$ are optimization parameters and

$$g_l^{\delta} := F'\big(x_l^{\delta}\big)^* \left(F\big(x_l^{\delta}\big) - y^{\delta} \right) \in X^{\mathrm{c}}$$

with $l \in I_n^{\delta}$ and $I_n^{\delta} \subseteq \{n - N + 1, ..., n\}$ for some fixed $N \geq 1$ are again the gradients of the least squares functional, evaluated at the respective iterates. We define the residual

$$R_n^{\delta} := F\big(x_n^{\delta}\big) - y^{\delta} \in Y^{\mathrm{c}}$$

for each step $n \in \mathbb{N}$.

We split the iterates $x_l^{\delta} \in X^{\mathrm{c}}$, $l = 0, ..., n+1$, into real part $x_l^{\mathrm{r},\delta} \in X$ and imaginary part $x_l^{\mathrm{i},\delta} \in X$ and define the stripes

$$\begin{aligned} H_{n,l}^{\mathrm{r},\delta} &:= H\big(u_{n,l}^{\mathrm{r},\delta}, \alpha_{n,l}^{\mathrm{r},\delta}, \xi_l^{\delta}\big) \subseteq X, \\ H_{n,l}^{\mathrm{i},\delta} &:= H\big(u_{n,l}^{\mathrm{i},\delta}, \alpha_{n,l}^{\mathrm{i},\delta}, \xi_l^{\delta}\big) \subseteq X \end{aligned} \tag{3.3}$$

with their respective offsets

$$\begin{aligned} \alpha_{n,l}^{\mathrm{r},\delta} &:= \left\langle u_{n,l}^{\mathrm{r},\delta}, x_l^{\mathrm{r},\delta} \right\rangle \\ \alpha_{n,l}^{\mathrm{i},\delta} &:= \left\langle u_{n,l}^{\mathrm{i},\delta}, x_l^{\mathrm{i},\delta} \right\rangle \end{aligned} \tag{3.4}$$

and width

$$\xi_l^{\delta} := \big\|R_l^{\delta}\big\| \cdot \big(\delta + c_{\mathrm{tc}}\big(\big\|R_l^{\delta}\big\| + \delta\big)\big) \tag{3.5}$$

for all $l \in I_n^{\delta}$. Here, we choose the search directions as the real and imaginary part of the respective gradients by setting

$$\begin{aligned} u_{n,l}^{\mathrm{r},\delta} &:= \mathrm{Re}\big(g_l^{\delta}\big), \\ u_{n,l}^{\mathrm{i},\delta} &:= \mathrm{Im}\big(g_l^{\delta}\big). \end{aligned} \tag{3.6}$$

In the iteration (3.2), we choose the parameters $t_{n,l}^{\mathrm{r},\delta}$ and $t_{n,l}^{\mathrm{i},\delta}$ such that

$$x_{n+1}^{\mathrm{r},\delta} \in \bigcap_{l \in I_n^{\delta}} H_{n,l}^{\mathrm{r},\delta} \tag{3.7}$$

and

$$x_{n+1}^{\mathrm{i},\delta} \in \bigcap_{l \in I_n^{\delta}} H_{n,l}^{\mathrm{i},\delta}. \tag{3.8}$$

This is again accomplished by calculating the metric projection of $x_{n+1}^{\mathrm{r},\delta}$ and $x_{n+1}^{\mathrm{i},\delta}$ onto the respective above intersection, which is a convex subset of X.

Remark 3.1. *By splitting the iterates and search directions into real and imaginary part we obtain, together with the above definitions, basically the same methods as for real Hilbert spaces. We thus refrain from explicitly formulating the analogues of Algorithms 1.14, 1.19 and discuss a fast method with two search directions in more detail.*

However, it is important to remark that the (complex valued) search directions $u_{n,l}^{\delta}$ are calculated without any separations of real and imaginary parts of the current iterate. Consequently, they are still determined by the full forward model without neglecting any mutual influences. By optimizing the parameters $t_{n,l}^{\mathrm{r},\delta}$ and $t_{n,l}^{\mathrm{i},\delta}$ separately, we even hope to gain accuracy in the reconstructions due to the individual treatment of the iterate's real and imaginary part. This can be an asset if they differ significantly in their (absolute) values.

The following algorithm yields an iterative (regularizing) method to solve nonlinear inverse problems $F(x) = y$ from given (noisy) data y^{δ}.

Algorithm 3.2. *(RESESOP for nonlinear operators on complex Hilbert spaces with two search directions) As in Algorithm 1.21, choose an initial value $x_0^{\delta} := x_0 \in X^{\mathrm{c}}$. In the first step ($n = 0$) take u_0^{δ} and then, for all $n \geq 1$, choose the search directions $\{u_n^{\delta}, u_{n-1}^{\delta}\}$, where*

$$\begin{aligned} u_n^{\delta} &= u_n^{\mathrm{r},\delta} + i \cdot u_n^{\mathrm{i},\delta} := F'\big(x_n^{\delta}\big)^* w_n^{\delta}, \\ w_n^{\delta} &:= F\big(x_n^{\delta}\big) - y^{\delta}. \end{aligned} \tag{3.9}$$

Define $H_{-1}^{\mathrm{r},\delta} := H_{-1}^{\mathrm{i},\delta} := X$ and, for $n \in \mathbb{N}$, the stripes

$$\begin{aligned} H_n^{\mathrm{r},\delta} &:= H\big(u_n^{\mathrm{r},\delta}, \alpha_n^{\mathrm{r},\delta}, \xi_n^{\delta}\big), \\ H_n^{\mathrm{i},\delta} &:= H\big(u_n^{\mathrm{i},\delta}, \alpha_n^{\mathrm{i},\delta}, \xi_n^{\delta}\big) \end{aligned} \tag{3.10}$$

with

$$\begin{aligned} \alpha_n^{\mathrm{r},\delta} &:= \Big\langle u_n^{\mathrm{r},\delta}, x_n^{\mathrm{r},\delta} \Big\rangle - \big\|R_n^{\delta}\big\|^2, \\ \alpha_n^{\mathrm{i},\delta} &:= \Big\langle u_n^{\mathrm{i},\delta}, x_n^{\mathrm{i},\delta} \Big\rangle - \big\|R_n^{\delta}\big\|^2, \\ \xi_n^{\delta} &:= \big\|R_n^{\delta}\big\| \big(\delta + c_{\mathrm{tc}}\big(\big\|R_n^{\delta}\big\| + \delta\big)\big). \end{aligned} \tag{3.11}$$

As a stopping rule choose the discrepancy principle, where

$$\tau > \frac{1 + c_{\mathrm{tc}}}{1 - c_{\mathrm{tc}}}. \tag{3.12}$$

As long as $\big\|R_n^{\delta}\big\| > \tau\delta$, we have

$$x_n^{\mathrm{r},\delta} \in H_>\big(u_n^{\mathrm{r},\delta}, \alpha_n^{\mathrm{r},\delta} + \xi_n^{\delta}\big) \cap H_{n-1}^{\mathrm{r},\delta} \tag{3.13}$$

and

$$x_n^{\mathrm{i},\delta} \in H_>\big(u_n^{\mathrm{i},\delta}, \alpha_n^{\mathrm{i},\delta} + \xi_n^{\delta}\big) \cap H_{n-1}^{\mathrm{i},\delta}, \tag{3.14}$$

and thus calculate the new iterate $x_{n+1}^{\delta} = x_{n+1}^{\mathrm{r},\delta} + i \cdot x_{n+1}^{\mathrm{i},\delta}$ according to the following two steps.

(i) Compute

$$\begin{aligned} \tilde{x}_{n+1}^{\mathrm{r},\delta} &:= P_{H(u_n^{\mathrm{r},\delta}, \alpha_n^{\mathrm{r},\delta} + \xi_n^{\delta})}\big(x_n^{\mathrm{r},\delta}\big) \\ &= x_n^{\mathrm{r},\delta} - \frac{\Big\langle u_n^{\mathrm{r},\delta}, x_n^{\mathrm{r},\delta} \Big\rangle - \big(\alpha_n^{\mathrm{r},\delta} + \xi_n^{\delta}\big)}{\big\|u_n^{\mathrm{r},\delta}\big\|^2} u_n^{\mathrm{r},\delta}. \end{aligned} \tag{3.15}$$

Compute $\tilde{x}_{n+1}^{\mathrm{i},\delta}$ *analogously and set* $\tilde{x}_{n+1}^{\delta} = \tilde{x}_{n+1}^{\mathrm{r},\delta} + i \cdot \tilde{x}_{n+1}^{\mathrm{i},\delta}$.
Then the descent property

$$\left\|z - \tilde{x}_{n+1}^{\delta}\right\|^2 \leq \left\|z - x_n^{\delta}\right\|^2 - \Big(\left\|R_n^{\delta}\right\|\big(\left\|R_n^{\delta}\right\| - \delta - c_{\mathrm{tc}}\big(\left\|R_n^{\delta}\right\| + \delta\big)\big)\Big)^2 \cdot \Big(\|u_n^{\mathrm{r},\delta}\|^{-2} + \|u_n^{\mathrm{i},\delta}\|^{-2}\Big)$$

is valid for all $z \in M_{F(x)=y}$.
If $\tilde{x}_{n+1}^{\mathrm{r},\delta} \in H_{n-1}^{\mathrm{r},\delta}$, *we have* $\tilde{x}_{n+1}^{\mathrm{r},\delta} = P_{H_n^{\mathrm{r},\delta} \cap H_{n-1}^{\mathrm{r},\delta}}\big(x_n^{\mathrm{r},\delta}\big)$. *Analogously, if* $\tilde{x}_{n+1}^{\mathrm{i},\delta} \in H_{n-1}^{\mathrm{i},\delta}$, *we have* $\tilde{x}_{n+1}^{\mathrm{i},\delta} = P_{H_n^{\mathrm{i},\delta} \cap H_{n-1}^{\mathrm{i},\delta}}\big(x_n^{\mathrm{i},\delta}\big)$. *If both conditions are fulfilled, we are done. Otherwise, go to step (ii).*

(ii) First, in case the condition from step (i) is not fulfilled for $\tilde{x}_{n+1}^{\mathrm{r},\delta}$, *decide whether* $\tilde{x}_{n+1}^{\mathrm{r},\delta} \in H_{>}\big(u_{n-1}^{\mathrm{r},\delta}, \alpha_{n-1}^{\mathrm{r},\delta} + \xi_{n-1}^{\delta}\big)$ *or* $\tilde{x}_{n+1}^{\mathrm{r},\delta} \in H_{<}\big(u_{n-1}^{\mathrm{r},\delta}, \alpha_{n-1}^{\mathrm{r},\delta} - \xi_{n-1}^{\delta}\big)$. *Calculate accordingly*

$$x_{n+1}^{\mathrm{r},\delta} := P_{H(u_n^{\mathrm{r},\delta}, \alpha_n^{\mathrm{r},\delta} + \xi_n^{\delta}) \cap H(u_{n-1}^{\mathrm{r},\delta}, \alpha_{n-1}^{\mathrm{r},\delta} \pm \xi_{n-1}^{\delta})}\big(\tilde{x}_{n+1}^{\mathrm{r},\delta}\big),$$

i.e., determine $x_{n+1}^{\mathrm{r},\delta} = \tilde{x}_{n+1}^{\mathrm{r},\delta} - t_{n,n}^{\mathrm{r},\delta} u_n^{\mathrm{r},\delta} - t_{n,n-1}^{\mathrm{r},\delta} u_{n-1}^{\mathrm{r},\delta}$ *such that* $\big(t_{n,n}^{\mathrm{r},\delta}, t_{n,n-1}^{\mathrm{r},\delta}\big)$ *minimizes the function*

$$h_{r,2}\big(t_1^{\mathrm{r}}, t_2^{\mathrm{r}}\big) := \frac{1}{2}\left\|\tilde{x}_{n+1}^{\mathrm{r},\delta} - t_1^{\mathrm{r}} u_n^{\mathrm{r},\delta} - t_2^{\mathrm{r}} u_{n-1}^{\mathrm{r},\delta}\right\|^2 + t_1^{\mathrm{r}}\big(\alpha_n^{\mathrm{r},\delta} + \xi_n^{\delta}\big) + t_2^{\mathrm{r}}\big(\alpha_{n-1}^{\mathrm{r},\delta} \pm \xi_{n-1}^{\delta}\big).$$

Proceed analogously with $\tilde{x}_{n+1}^{\mathrm{i},\delta}$.
Then we have $x_{n+1}^{\mathrm{r},\delta} = P_{H_n^{\mathrm{r},\delta} \cap H_{n-1}^{\mathrm{r},\delta}}\big(x_n^{\mathrm{r},\delta}\big)$ *as well as* $x_{n+1}^{\mathrm{i},\delta} = P_{H_n^{\mathrm{i},\delta} \cap H_{n-1}^{\mathrm{i},\delta}}\big(x_n^{\mathrm{i},\delta}\big)$ *and we set* $x_{n+1}^{\delta} = x_{n+1}^{\mathrm{r},\delta} + i \cdot x_{n+1}^{\mathrm{i},\delta}$. *For all* $z \in M_{F(x)=y}$ *the descent property*

$$\left\|z - x_{n+1}^{\delta}\right\|^2 \leq \left\|z - x_n^{\delta}\right\|^2 - \big(S_n^{\mathrm{r},\delta} + S_n^{\mathrm{i},\delta}\big) \tag{3.16}$$

is fulfilled, where

$$\begin{aligned} S_n^{\mathrm{r},\delta} := & \left(\frac{\left\|R_n^{\delta}\right\|\big(\left\|R_n^{\delta}\right\| - \delta - c_{\mathrm{tc}}\big(\left\|R_n^{\delta}\right\| + \delta\big)\big)}{\left\|u_n^{\mathrm{r},\delta}\right\|}\right)^2 \\ & + \left(\frac{\left|\langle u_{n-1}^{\mathrm{r},\delta}, \tilde{x}_{n+1}^{\mathrm{r},\delta}\rangle - \big(\alpha_{n-1}^{\mathrm{r},\delta} \pm \xi_{n-1}^{\delta}\big)\right|}{\gamma_n^{\mathrm{r},\delta}\left\|u_{n-1}^{\mathrm{r},\delta}\right\|}\right)^2 \end{aligned}$$

with

$$\gamma_n^{\mathrm{r},\delta} := \left(1 - \left(\frac{\left|\langle u_n^{\mathrm{r},\delta}, u_{n-1}^{\mathrm{r},\delta}\rangle\right|}{\left\|u_n^{\mathrm{r},\delta}\right\| \cdot \left\|u_{n-1}^{\mathrm{r},\delta}\right\|}\right)^2\right)^{\frac{1}{2}} \in (0, 1]$$

and analogously defined $S_n^{\mathrm{i},\delta}$ *and* $\gamma_n^{\mathrm{i},\delta}$.

Remark 3.3. *As before, we give a few interpretations of the above method.*

(a) The statements (3.13) *and* (3.14) *are again a consequence of our choice* (3.12) *and can be derived in exactly the same way as for the respective statement in Algorithm 1.21. Here we also see that we need - or rather must - not adapt the width of the stripes.*

(b) The descent properties follow directly from

$$\left\|z - x_{n+1}^{\delta}\right\|^2 = \left\|\mathrm{Re}\big(z - x_{n+1}^{\delta}\big)\right\|^2 + \left\|\mathrm{Im}\big(z - x_{n+1}^{\delta}\big)\right\|^2$$

and the descent properties that hold for the metric projection in real Hilbert spaces.

(c) *Splitting up the iterates and defining separate stripes for real and imaginary part yields an interesting advantage. By optimizing real and imaginary part separately, the optimization parameters t are calculated independently of the respective other part of the iterate, i.e., the imaginary part of the new iterate is calculated without having to take into account the real part and vice versa. This is a further option to accelerate the method in comparison to the Landweber iteration, where the relaxation parameter ω is chosen as a constant. In the case of the inverse problem of THz tomography, numerical experiments have shown that ω has to be chosen very small to get good reconstructions for both the real and the imaginary part. To reconstruct only the real part, which is mainly determined by the refractive index n, the value of ω can be chosen larger, yielding a faster reconstruction.*

(d) *The calculation of the search direction u_n^δ contains both the real and the imaginary part, which reflects the underlying physical model, where the complex refractive index is treated as one parameter. In the case of THz tomography, we consequently do not have to increase the number of evaluations of the Helmholtz equation by splitting up the subspace optimization, such that the additional computational cost is limited to the additional calculations of the optimization parameters t. As we have mentioned before, the computational effort in this case is comparatively low. The expressions for the optimization parameters are given explicitly for Algorithm 1.21, see Section A.2, and can be directly adapted to the complex case.*

3.2. Reconstruction of the complex refractive index from simulated data

To conclude this work, we will present numerical reconstructions of m from synthetic noisy data, using a Gaussian beam with a frequency within the lower THz spectrum.

Again, we will restrict ourselves to a purely rotating THz tomograph, i.e., the object is fixed in the middle of the domain defined by the receivers. During the measuring process, the receivers are rotated around the object in equidistant steps $2\pi/J$, where $J = |\mathbf{J}|$ is the number of positions. The receivers are arranged in a circle with a fixed distance to their neighbors. By neglecting the shifting of the object, we can work with only one domain $\Omega = \Omega^j$ for all $j \in \mathbf{J}$ during the whole process. For the later reconstruction, this means that we can again rotate the receivers and fix the object's position.

Parameter	**Value**
Frequency f	$0.1 \cdot 10^{11}$ Hz
Wave length λ	$2.998 \cdot 10^{-3}$ m
Beam waist W_0	0.015 m
Rayleigh zone y_0	0.02 m
Number of receivers N	40
Number of positions J	180
c_{tc}	0.9
τ	20

Table 3.1.: Parameters of the numerical RESESOP experiment

For our first reconstruction, we choose an object similar to the one we used before in Section 2.6.

The tested object is again a plastic block with complex refractive index

$$m_1 = 1 - (1.5 + i \cdot 0.005)^2 = -1.249975 - i \cdot 0.015.$$

Inside the object, there are two inclusions. One is a hole filled with air ($m_2 \equiv 0$), the other one is a material with a higher optical density, its complex refractive index is

$$m_3 = 1 - (1.8 + i \cdot 0.02)^2 = -2.2396 - i \cdot 0.072.$$

Both inclusions are circular, now with a smaller defect in the range of the beam's wave length. We now use radiation in the low THz frequency range,

$$f = 0.1\,\mathrm{THz},$$

which corresponds to the wave number $k_0 = {}^{2\pi f}/_{c_0} \approx 2095.8\,\mathrm{m}^{-1}$, and generate synthetic data for the reconstruction with Algorithm 3.2. We note that the higher frequency calls for a refinement of the finite element mesh, such that a reconstruction using the RESESOP method is especially interesting in order to reduce the number of iterations. Also, we increase the number of receivers (in practice, when only a small number of receivers is available, this can be realized by rotating the receivers while fixing the position of the emitter).

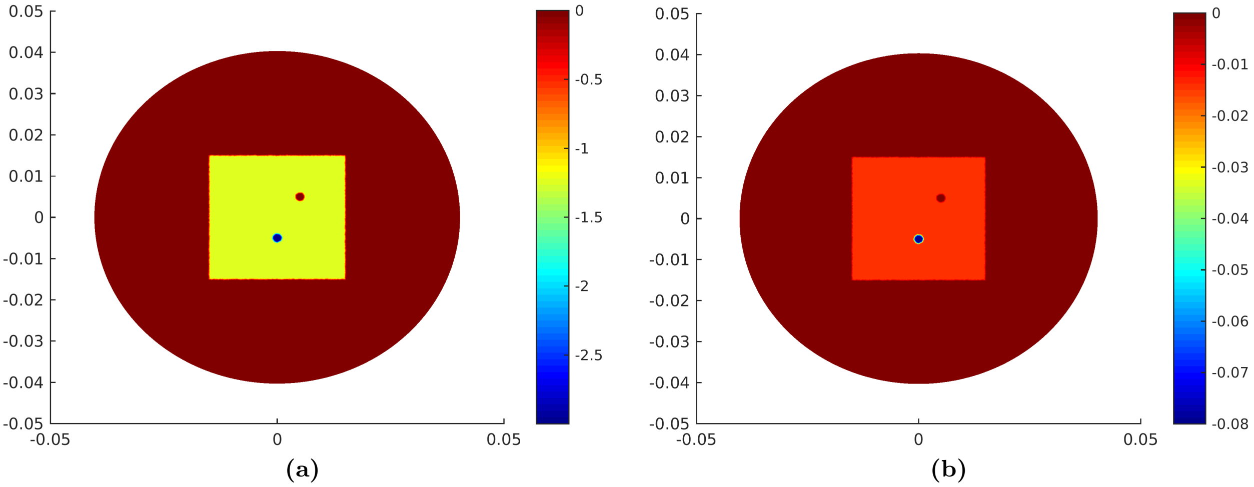

Figure 3.1.: Real (a) and imaginary (b) part of m.

As an a priori information, we use the knowledge of the object's outer interfaces and set the starting value to $m_0(\mathbf{x}) = (-1 - i \cdot 0.001) \cdot \chi_D(\mathbf{x})$ as before. The key data of the reconstruction are listed in Table 3.2, the reconstructions from synthetic data obtained with Algorithm 3.2 are displayed in Figure 3.2

Number of iterations n_*	30
Execution time	14 h 13 min 51 s
Relative error in reconstructed real part Re(m)	7.98 %
Relative error in reconstructed imaginary part Im(m)	456.33 %

Table 3.2.: Some key data to evaluate the performance of the RESESOP method (Algorithm 3.2) at the identification of m of the tested object using a Gaussian beam with a frequency $f = 0.1\,\mathrm{THz}$.

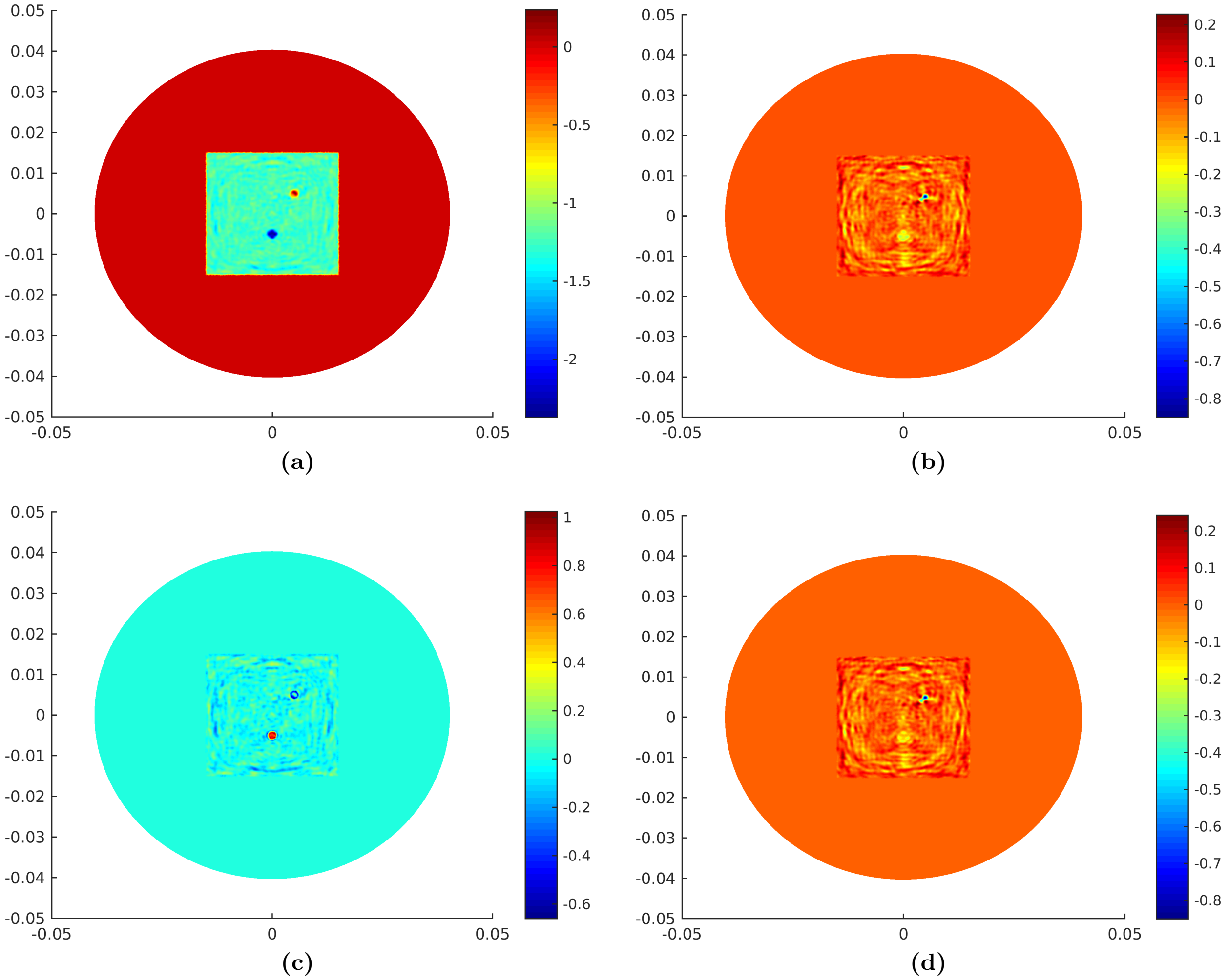

Figure 3.2.: Reconstruction $m^{\delta}_{n_*}$ of real (a) and imaginary (b) part of m after $n_* = 30$ iterations with the RESESOP method (using two search directions, Algorithm 3.2) and the respective error in the reconstruction $m - m^{\delta}_{n_*}$ ((c) real part and (d) imaginary part). The object was scanned by a Gaussian beam of frequency $f = 0.1\,\text{THz}$.

Similar to the results from the Landweber experiment, the real part $\text{Re}(m)$ is reconstructed much more accurately than the imaginary part $\text{Im}(m)$. The error plots indicate that the reconstructed real part allows quantitative and qualitative conclusions, while the reconstructed imaginary part yields at most some qualitative information about the position of the unknown defects.
Let us consider only the reconstruction of the real part of m. We note that the upper defect - the hole filled with air - is identified almost accurately, the minor difference is due to the discretization. The inclusion of the denser material in the middle of the object's lower part shows an offset in the reconstruction. The absolute value of $\text{Re}(m_3)$ is reconstructed too small. The reason could be the relatively high absorption coefficient, which causes a lower penetration depth of the radiation into the inclusion.

Remark 3.4. *This numerical experiment yields some insight into the application of Algorithm 3.2 in THz tomography:*

(a) The importance of an adequate choice for the parameter c_{tc} *from the tangential cone condition*

(1.32) becomes apparent. Several tests indicate the divergence of Algorithm 3.2 for a lower value of c_{tc}. Since the constant τ from Morozov's discrepancy principle has to be chosen such that $\tau > (1 + c_{\mathrm{tc}}) \cdot (1 - c_{\mathrm{tc}})^{-1}$, we have to settle for a higher tolerance in the data fitting term $\|R_n^\delta\|$.

(b) The choice of c_{tc} may depend on the multiple other parameters, such as the number of receivers, the size of the receivers, and most of all on the incident beam, in particular the wave number k_0.

(c) These findings might give a hint that the tangential cone condition (1.32) is indeed valid for c_{tc} close to 1.

To conclude, we present the results of two further experiments. In both experiments, we use synthetic data with additional 2% noise as before. First, we want to compare the performance of our RESESOP method 3.2 to the Landweber method from the previous chapter. To this end, we generated synthetic noisy data as before, using the frequency $f = 2.5 \cdot 10^{10}$ Hz, for the object we already used in the example in Chapter 2 with the larger inclusions. For the reconstruction, we now use Algorithm 3.2. We choose the same parameters for the setup as in the Landweber experiment, see Table 2.1, and choose c_{tc} and τ as in our previous RESESOP experiment. The performance is illustrated in Table 3.3.

Number of iterations n_*	20
Execution time	1 h 12 min 40 s
c_{tc}	0.9
τ	20

Table 3.3.: Some key data to evaluate the performance of the RESESOP method (Algorithm 3.2) in comparison with the Landweber method at the identification of m of the object from Chapter 2, using the microwave frequency $f = 2.5 \cdot 10^{10}$ Hz.

We are mainly interested in the execution time, which is significantly lower than in the Landweber experiment. This complements the results from the numerical experiment in Chapter 1, underlining the main advantage of our subspace methods. The reconstructions are presented in Figure 3.3.

However, it is important to remark that the performance of the RESESOP method can be improved by choosing a smaller constant c_{tc}, keeping in mind that this constant depends on the wave number k_0. Numerical experiments have shown that it is sufficient to choose $c_{\mathrm{tc}} = 0.6$ for $f = 2.5 \cdot 10^{10}$ Hz, which allows a smaller parameter τ in the discrepancy principle.

Second, we generated synthetic data y^δ by illuminating the object presented in Figure 3.1 with a Gaussian beam, now at a frequency of $2.5 \cdot 10^{10}$ Hz. All other parameters are preserved. For a better comparability and given the small size of the inclusions, we have not adapted the maximal element size of the triangularization to the larger wave length. The performance is illustrated in Table 3.4, the plots of the reconstructions in Figure 3.4.

A comparison with the results that were obtained with the THz frequency $f = 0.1$ THz shows the advantage of using a Gaussian beam with a higher frequency. As expected, the resolution increases with the frequency, which is well visible in our experiments. When testing the object with THz radiation, we are able to reconstruct the refractive index quantitatively and qualitatively, permitting a precise identification of the defects without any a priori information about them. The results we obtained with the microwave radiation now hardly enable a characterization of the object's state. The inclusions are barely visible and we can expect that smaller defects are not detectable at all

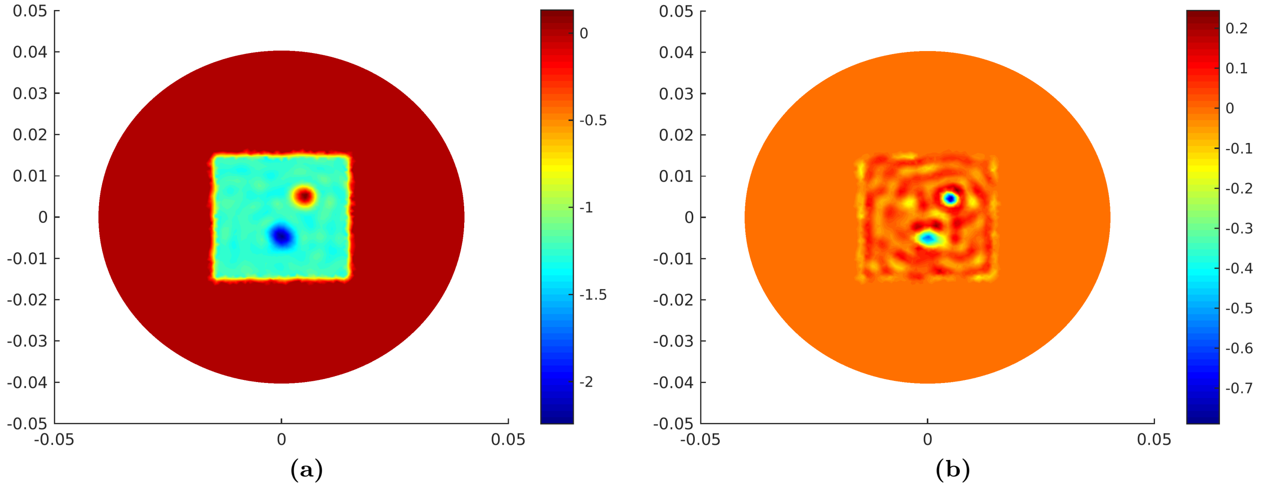

Figure 3.3.: Reconstruction $m^{\delta}_{n_*}$ of real (a) and imaginary (b) part of m after $n_* = 20$ iterations with the RESESOP method (using two search directions, Algorithm 3.2). The object was scanned by a Gaussian beam of frequency $f = 2.5 \cdot 10^{10}$ Hz.

Number of iterations n_*	32
Execution time	13 h 36 min 13 s
Relative error in reconstructed real part $\mathrm{Re}(m)$	9.43 %
Relative error in reconstructed imaginary part $\mathrm{Im}(m)$	473.63 %

Table 3.4.: Some key data to evaluate the performance of the RESESOP method (Algorithm 3.2) at the identification of the complex refractive index of the tested object using a Gaussian beam with a microwave frequency $f = 2.5 \cdot 10^{10}$ Hz.

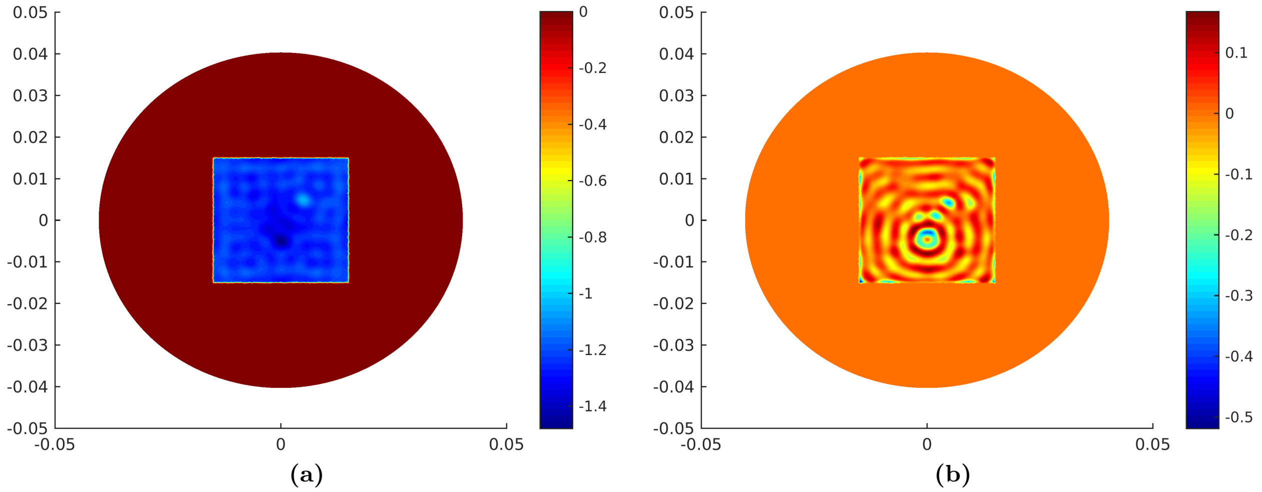

Figure 3.4.: Reconstruction $m^{\delta}_{n_*}$ of real (a) and imaginary (b) part of the complex refractive index m after 32 iterations with the RESESOP method (using two search directions, Algorithm 3.2 and the frequency $f = 2.5 \cdot 10^{10}$ Hz).

when using microwave radiation. Regarding the imaginary part of m, the defect in the lower part of the object is visible as a peak, allowing a localization, whereas the hole in the top right corner is not visible in the reconstruction.

For both frequencies, we see that a reconstruction of the imaginary part is not satisfactory. This suggests that a model, which is inspired by electromagnetic scattering, is not suitable to describe the absorption of an electromagnetic beam by dielectric materials. In our case, we are interested in the nondestructive testing of objects consisting of materials with a very low absorption coefficient, such that these objects are almost opaque for the electromagnetic radiation. One of the approximations we made in the modeling is the use of the superposition principle. This physical law fails if the illuminated objects are absorbing: If an electromagnetic wave travels through an absorbing medium, it loses energy. This medium has to be considered as a sink term in Maxwell's equations, which are, in that case, no longer linear partial differential equations. For this reason, an application of the superposition principle (i.e., the property that if two functions solve a linear equation, their sum also solves it) yields at most an approximation, as it is no longer strictly valid.

Reflection or refraction on the other hand are well modeled by our approach. These effects are determined by the refractive index, for which we have assumed that it fulfills the limit of geometrical optics. As we have

$$\mathrm{Re}(m) = \mathrm{Re}\big(1 - (n + i\kappa)^2\big) = 1 - n^2 + \kappa^2 \approx 1 - n^2$$

due to the low attenuation coefficient κ of the relevant objects, it is not surprising that the real part of m is reconstructed nicely, whereas the imaginary part is not reconstructed satisfactorily at all.

An alternative is a separate reconstruction of the refractive index n and the attenuation coefficient κ according to different physical models. Our findings show that the scattering approach is well suited for the reconstruction of the refractive index. The knowledge of the refractive index yields a geometric description of the beam's propagation through the medium. Hence, we obtain good estimates for the *ray paths* of the electromagnetic beam. The absorption coefficient causes the attenuation of the beam while it travels along these ray paths through the medium, such that the total attenuation of the ray by the object can be modeled with the help of an adapted Radon transform, which has been done by Tepe et.al. in [71] and yields far better results for the absorption coefficient than our approach. A combination of both methods in the shape of a *hybrid reconstruction method*, which exploits both models, is likely to increase the quality of the reconstructions and also the resolution.

Conclusion and outlook

In the first part of this thesis, we have developed a novel iterative reconstruction method for nonlinear inverse problems based on the sequential subspace optimization method for linear problems [56, 68, 69]. The basic idea is a sequential projection onto stripes for both exact and noisy data. The position and geometry of these stripes are designed to contain the solution set of the underlying nonlinear operator equation by taking into account the local character of nonlinear operators and the tangential cone condition. By using the current gradient of the least squares functional as a search direction in each step of the SESOP iteration, we obtain at least a weakly convergent subsequence. For a special choice of search directions, we have been able to prove convergence and stability results. In particular, we obtain a regularization method for the solution of the inverse problem, when only noisy data are given. Furthermore, we have presented a fast algorithm that uses two search directions per iteration. This algorithm particularly yields a good understanding of our subspace methods and is well suited for implementation. Our findings have been published in [72]. We have applied our SESOP and RESESOP methods to solve a well-understood nonlinear parameter identification problem from the knowledge of exact and noisy data. In comparison to a standard Landweber method, we have observed a significant increase in the speed of reconstructions by applying Algorithm 1.21, were we have used the current and the previous gradient as the two search directions in each iteration.
Additionally, we have obtained a Landweber type method with step size adaption, based on Algorithm 1.19 with a single search direction, which is also significantly faster than the standard Landweber method, but not as fast as Algorithm 1.21. A direct comparison of the two subspace methods underlines that the additional computational cost per iteration due to the second search direction reduces the total number of iterations (until the algorithm is stopped by the discrepancy principle) and also the total reconstruction time. The reason is the expensive calculation of a new search direction.

The performance of our methods suggested an application for the solution of a more challenging inverse problem, in particular the reconstruction of the complex refractive index m from THz tomographic measurements. In this context, we have discussed a model for THz tomography based on the Helmholtz equation. The forward operator, a nonlinear parameter-to-solution mapping combined with a linear observation operator, has been analyzed regarding boundedness, continuity and differentiability properties. In addition, we have obtained representations of the Fréchet derivative and its adjoint, such that we are able to calculate the gradient of the least squares functional, which plays a central role in the reconstruction techniques we employ.

In order to apply SESOP methods to solve the inverse problem of THz tomography, we made some adjustments to fit the requirements of complex Hilbert spaces. In Algorithm 3.2, these considerations have been taken into account and we have obtained an adapted fast reconstruction method, based on Algorithm 1.21. This algorithm has been implemented to recover the complex refractive index of test objects from noisy synthetic data. The resulting reconstructions of $\mathrm{Re}(m)$ are suitable for the detection and identification of defects and material properties, whereas the respective imaginary part $\mathrm{Im}(m)$ merely allows conclusions on the existence and position of defects.

Future research

A natural continuation of our work regarding sequential subspace optimization for nonlinear inverse problems, and also of the results presented in [68, 69], is the extension to Banach spaces. Banach spaces are usually not equipped with an inner product, such that orthogonality, orthogonal projections and distances have to be replaced by appropriate alternatives such as Bregman distances and Bregman projections. As a Banach space is in general not isomorphic to its dual space, duality mappings, which correspond to the identity mapping in Hilbert spaces, become a basic tool in the theory of inverse problems. The underlying functional analytic theory can be found in [16, 70], along with an extensive overview of regularization methods in Banach spaces.

Using Banach spaces as source (or data) space may yield advantages in some situations: In the case that the source $x \in X$ is an element of some L^p space ($p > 2$), we also have $x \in L^2(\Omega)$, but at the same time we neglect available information about x, i.e., its regularity. Banach space methods make it possible to pay respect to these properties. Specifically in our inverse problem of THz tomography, an expansion of our SESOP methods to Banach spaces may be reasonable: We know that $m \in L^\infty(\Omega)$, which is not a reflexive Banach space, but by using $m \in L^p(\Omega)$ we can use Banach space methods and approximate the essential boundedness of m by letting $p \to \infty$. In [70] some examples are presented that illustrate the advantages of using Banach spaces.

Regarding THz tomography, a reconstruction from real data is the next step. To this end, several adaptions are necessary. First of all, the object is usually not only rotated, but also shifted during the measuring process. This is a minor adaption mostly based on the integration of the respective transformation

$$\begin{pmatrix} x \\ y \end{pmatrix} \mapsto \begin{pmatrix} \cos(\theta_{j_1}) & \sin(\theta_{j_1}) \\ -\sin(\theta_{j_1}) & \cos(\theta_{j_1}) \end{pmatrix} \cdot \begin{pmatrix} x \\ y \end{pmatrix} + \begin{pmatrix} d_{j_2} \\ 0 \end{pmatrix},$$

where we have used the notation from Section 2.4.4. However, the implementation of the direct and adjoint problem have to be altered in order to take into account the changing domains $\Omega^{\mathbf{j}}$. The second adaption refers to the type of data that are generated by the receivers. For our purposes, we are mainly interested in an evaluation of intensity data or *transmittivities*. To this end, the measuring process has to be well understood and the resulting observation operator $Q^{\mathbf{j}}$ has to be defined and analyzed. In any case, a suitable observation operator is nonlinear, which demands some further analysis regarding for example the adjoint of the forward operator's linearization. A possible choice for the observation operator is

$$Q^{\mathbf{j}}(\gamma^{\mathbf{j}} u^{\mathbf{j}}) = \frac{1}{K} \left(\int_{E_\nu^{\mathbf{j}}} e_\nu^{\mathbf{j}}(\mathbf{x}) \left| \gamma^{\mathbf{j}} u^{\mathbf{j}}(\mathbf{x}) \right|^2 \, \mathrm{d}s_{\mathbf{x}} \right)_{\nu=1,\dots,N},$$

where K is a constant that is obtained by calibrating the tomograph, such that the data are related to the measured intensities in vacuum. This value might also depend on the receiver $E_\nu^{\mathbf{j}}$ and could yield a basis to evaluate the model for the measuring process.

Given the high numerical effort that has to be invested in order to obtain quantitative reconstructions, an alternative approach might be to stop the iteration as soon as the shape of the defects become visible. By means of image analysis, the interfaces inside the object can be extracted. For a reconstruction of the complex refractive index with the adapted algebraic reconstruction technique (adapted ART), see [71], the knowledge of the object's outer interfaces is necessary. The additional knowledge of inner interfaces can also be used as a priori information and is likely to increase the accuracy of the results with the adapted ART.

Interfaces can be characterized for example by applying a differential operator such as the Laplacian to the reconstruction: If $\Delta m(\mathbf{x})$ is large in $\mathbf{x}$, it is probable that $\mathbf{x}$ is an interface point. By defining

$$\mathrm{Int}(\mathbf{x}) := \begin{cases} 1, & \text{if } |\Delta m(\mathbf{x})| \geq C, \\ 0, & \text{else} \end{cases}$$

for all $\mathbf{x} \in \mathrm{supp}(m)$ and some suitable threshold $C > 0$, we obtain a characteristic function, which is equal to 1 only at the interfaces. Depending on the artifacts, more elaborate techniques from image analysis may yield better results.

From a more theoretical point of view, a generalization of the statements from Chapter 2 regarding the properties of the scattering map and the occurring boundary value problems is of interest. In particular, the use of Robin boundary conditions instead of the more common Dirichlet or Neumann boundary conditions is a major concern. Arendt et al. (see, e.g., [3, 4]) have addressed these questions, in addition to boundary value problems in connection to inverse problems [2]. An analysis in the context of their methods might yield interesting results, also for applications.

A final goal is the development of a *hybrid model* and an according hybrid algorithm for the numerical solution of the inverse problem of THz tomography. In the previous chapter, we have already mentioned the deficit of the model we used in this work, which is the attenuation of the electromagnetic radiation by the tested object. In computerized tomography, the attenuation is computed from its Radon transform. A similar approach in THz tomography is possible, if the propagation of the THz radiation along refracted lines is taken into account. We are thus dealing with a Radon transform along refracted lines. These could be obtained by the knowledge of the object's refractive index n, which is well reconstructed by the methods we have used so far. The approach via a generalized Radon transform has already been successfully addressed by Tepe et al. in [71]. A combination of the two models is likely to yield promising results for the inverse problem of THz tomography.

A. Notation and formulas

A.1. Notations

The following notation is used throughout the thesis.

$\mathbb{N} = \{0, 1, 2, ...\}$	the natural numbers
$\lVert\cdot\rVert_X$	a norm in the space X
$(\cdot,\cdot)_X$, $\langle\cdot,\cdot\rangle_X$	inner products on X
$\lVert\cdot\rVert_{X\to Y}$	the operator norm of a mapping $X \to Y$
$\lVert\cdot\rVert_{X^*}$	the norm of a functional $X \to \mathbb{K}$
$(\cdot,\cdot)_{X^*\times X}$	the dual pairing in X
$\lim$	the limit of a strongly convergent sequence
$\sigma\text{-}\lim$	the limit of a weakly convergent sequence
$\mathcal{D}(F)$	the domain of an operator F
$\mathcal{N}(F)$	the null space of an operator F
$\mathcal{R}(F)$	the range of an operator F

A.2. Optimization parameters for the RESESOP algorithm with two search directions

In Algorithm 1.21, the current iterate is projected onto the intersection of the two given stripes in two steps. We have

$$x_n^\delta \in H_>\big(u_n^\delta, \alpha_n^\delta + \xi_n^\delta\big) \cap H_{n-1}^\delta$$

which implicates

$$x_n^\delta \in H_>\big(u_n^\delta, \alpha_n^\delta + \xi_n^\delta\big) \cap H_\leq\big(u_{n-1}^\delta, \alpha_{n-1}^\delta + \xi_{n-1}^\delta\big),$$

such that Proposition 1.8 can be applied. By substituting $u_1 := u_n^\delta$, $u_2 := u_{n-1}^\delta$, and

$$x_1 := \tilde{x}_{n+1}^\delta, \quad \alpha_1 := \alpha_n^\delta + \xi_n^\delta, \quad \alpha_2 := \alpha_{n-1}^\delta \pm \xi_{n-1}^\delta,$$

the same calculations as in the proof of Proposition 1.8 yield the optimal parameters

$$\begin{aligned} t_{n,n}^\delta &= \left(\frac{\left\langle u_n^\delta, u_{n-1}^\delta \right\rangle}{\left\langle u_n^\delta, u_{n-1}^\delta \right\rangle^2 - \left(\lVert u_n^\delta \rVert \cdot \lVert u_{n-1}^\delta \rVert \right)^2} \right) \cdot \left(\left\langle u_{n-1}^\delta, \tilde{x}_{n+1}^\delta \right\rangle - \left(\alpha_{n-1}^\delta + \xi_{n-1}^\delta \right) \right) \\ &= \left(\frac{\left\langle u_n^\delta, u_{n-1}^\delta \right\rangle}{\left\langle u_n^\delta, u_{n-1}^\delta \right\rangle^2 - \left(\lVert u_n^\delta \rVert \cdot \lVert u_{n-1}^\delta \rVert \right)^2} \right) \\ &\qquad \cdot \left(\left\langle u_{n-1}^\delta, \tilde{x}_{n+1}^\delta \mp x_{n-1}^\delta \right\rangle + \left(\lVert R_n^\delta \rVert^2 \mp \lVert R_n^\delta \rVert \left(\delta + c_{\mathrm{tc}}(\lVert R_n^\delta \rVert + \delta) \right) \right) \right) \end{aligned} \tag{A.1}$$

and

$$
\begin{aligned}
t^\delta_{n,n-1} &= -\left\|u^\delta_n\right\|^2 \left(\left\langle u^\delta_n, u^\delta_{n-1}\right\rangle^2 - \left(\|u^\delta_n\| \cdot \|u^\delta_{n-1}\|\right)^2\right)^{-1} \\
&\qquad\qquad \cdot \left(\left\langle u^\delta_{n-1}, \tilde{x}^\delta_{n+1}\right\rangle - \left(\alpha^\delta_{n-1} + \xi^\delta_{n-1}\right)\right) \\
&= -\left\|u^\delta_n\right\|^2 \left(\left\langle u^\delta_n, u^\delta_{n-1}\right\rangle^2 - \left(\|u^\delta_n\| \cdot \|u^\delta_{n-1}\|\right)^2\right)^{-1} \\
&\qquad\qquad \cdot \left(\left\langle u^\delta_{n-1}, \tilde{x}^\delta_{n+1} \mp x^\delta_{n-1}\right\rangle + \left(\|R^\delta_n\|^2 \mp \|R^\delta_n\| \left(\delta + c_{\mathrm{tc}}(\|R^\delta_n\| + \delta)\right)\right)\right).
\end{aligned}
\tag{A.2}
$$

These parameters can be used directly for an implementation of Algorithm 1.21 and, of course, of Algorithm 3.2, were the optimization parameters are calculated separately for real and imaginary part of the iterates according to the respective definitions.

B. Some supplementary mathematical theory

B.1. Functional analytic tools

The following definitions and statements can be found in many textbooks concerning partial differential equations and functional analysis (e.g. [5], [27], [32], [64]).

Throughout this thesis, we deal with $\mathbb{K}$-Hilbert spaces X, where $\mathbb{K} = \mathbb{R}$ or $\mathbb{K} = \mathbb{C}$ is the ground field of X. We usually use the norm that is induced by the inner product $(\cdot, \cdot) : X \times X \to \mathbb{K}$.

Definition B.1. *A mapping $a : X \times X \to \mathbb{C}$ is called a* sesquilinear form, *if*

$$\begin{aligned} a(u_1 + \lambda u_2, v_1) &= a(u_1, v_1) + \lambda a(u_2, v_1), \\ a(u_1, v_1 + \lambda v_2) &= a(u_1, v_1) + \overline{\lambda} a(u_1, v_2) \end{aligned}$$

for all $u_1, u_2, v_1, v_2 \in X$ and all $\lambda \in \mathbb{C}$.

Definition B.2. *A sesquilinear form is called X-*elliptic, *if there exist $\gamma > 0$ and $\sigma \in \mathbb{C}$ with $|\sigma| = 1$, such that*

$$\mathrm{Re}(\sigma a(u, u)) \geq \gamma \|u\|_X^2$$

for all $u \in X$.

Lemma B.3. *(*Lax-Milgram lemma*, [64]) Let X be a Hilbert space. If the sesquilinear form $a : X \times X \to \mathbb{C}$ is X-elliptic and bounded, the variational problem*

$$a(u, v) = \psi(v) \quad \textit{for all } v \in X$$

has a unique solution $u \in X$ for all functionals $\psi \in X^*$ and

$$\|u\|_X \leq \frac{1}{\gamma} \|\psi\|_{X^*},$$

where γ is chosen as in Definition B.2.

Remark B.4. *The condition of the X-ellipticity of the sesquilinear form a in the Lax-Milgram lemma can be replaced by the* coercivity *condition*

$$|a(u, u)| \geq \gamma \|u\|_X^2 \quad \textit{for all } u \in X, \tag{B.1}$$

see [64].

Theorem B.5. *(*Riesz representation theorem*, [5, 64]) For every bounded linear functional ψ on X there is a uniquely determined $w \in X$ such that*

$$a(w, v) = \psi(v)$$

for all $v \in X$, where a is a coercive bounded sesquilinear form.

Theorem B.6. *(*Fredholm alternative*, [12, 64, 76]) Let $T : X \to X$ be a compact linear operator and $\lambda \in \mathbb{C} \setminus \{0\}$ a constant. The homogeneous operator equation*

$$\lambda x - Tx = 0$$

either has only the trivial solution and the inhomogeneous equation

$$\lambda x - Tx = \tilde{x}$$

is uniquely solvable for each $\tilde{x} \in X$, or there are $n = \dim\big(\mathcal{N}(\lambda - T)\big) < \infty$ linearly independent solutions of the homogeneous equation (the space $\mathcal{N}(\lambda - T)$ is the kernel of the operator $\lambda - T$).

B.2. Partial differential equations

B.2.1. Some theory for linear elliptic partial differential equations

Definition B.7. *A linear elliptic differential operator L has the form*

$$Lu = a_{ij}(\mathbf{x})D_{ij}u + b_i(\mathbf{x})D_i u + c(\mathbf{x})u,$$

where $\mathbf{x} = (x_1, ..., x_n) \in \Omega \subseteq \mathbb{R}^n$, $n \geq 2$, and the matrix $A(\mathbf{x}) = (a_{ij}(\mathbf{x}))_{i,j=1,...,n}$ is symmetric and positive definite. The differential operators D_{ij} and D_i are given by

$$D_{ij} = \frac{\partial^2}{\partial x_i \partial x_j} \quad \text{and} \quad D_i = \frac{\partial}{\partial x_i}.$$

For a function f on Ω, we consider linear elliptic partial differential equations of the form

$$Lu = f.$$

Given the function f in some suitable function space on Ω, we are interested in the existence and uniqueness of solutions u, in particular in solutions of the Helmholtz equation.

Remark B.8. *By setting $a_{ij}(\mathbf{x}) = \delta_{ij}$, $b_i(\mathbf{x}) = 0$ and $c(x) = k^2(1 - m(\mathbf{x}))$ for all $\mathbf{x} \in \Omega$, where $m \in L^\infty(\Omega)$ and $\operatorname{supp}(m) \subseteq \Omega$, we obtain the Helmholtz equation*

$$\Delta u + k^2(1 - m)u = f.$$

Definition B.9. *Let $u \in L^p(\Omega)$ for some $p \geq 1$ and $\alpha := (\alpha_1, ..., \alpha_n)$ be a multiindex, such that*

$$D_\alpha \varphi := \left(\frac{\partial^{\alpha_1}}{\partial x_1^{\alpha_1}}\right) \cdots \left(\frac{\partial^{\alpha_n}}{\partial x_n^{\alpha_n}}\right) \varphi$$

for $\varphi \in C^{|\alpha|}(\Omega)$. A p-integrable function $g : \Omega \to \mathbb{R}$ is called the α-th weak derivative of u, if

$$\int_\Omega \varphi g \,\mathrm{d}\mathbf{x} = (-1)^{|\alpha|} \int_\Omega u D_\alpha \varphi \,\mathrm{d}\mathbf{x}$$

for all $\varphi \in C_0^{|\alpha|}(\Omega)$, and we write

$$g = D_\alpha u.$$

The functions φ are called test functions*.*
The Sobolev spaces $W^{k,p}(\Omega)$ are defined for $k \in \mathbb{N}$ and $1 \leq p < \infty$ by

$$W^{k,p}(\Omega) := \{u \in L^p(\Omega) \,:\, D_\alpha u \in L^p(\Omega) \text{ for all } |\alpha| \leq k\}$$

and are equipped with the norm

$$\|u\|_{W^{k,p}(\Omega)} := \left(\sum_{|\alpha| \leq k} \int_\Omega |D_\alpha u|^p \right)^{1/p} .$$

Remark B.10. *The Sobolev spaces $W^{k,p}(\Omega)$ are Banach spaces (see [27]). For $p = 2$ we obtain the Hilbert spaces*

$$H^k(\Omega) := W^{k,2}(\Omega),$$

which are equipped with the inner product

$$(u, v)_{H^k(\Omega)} := \sum_{|\alpha| \leq k} (D_\alpha u, D_\alpha v)_{L^2(\Omega)} .$$

We thus have $H^0(\Omega) = L^2(\Omega)$.

The following definition and statements are essential for the estimates in Chapter 2.

Definition B.11. *Let X_1 and X_2 be two Banach spaces with $X_1 \subseteq X_2$. The space X_1 is* continuously embedded *in X_2, if*

$$\|x\|_{X_2} \leq c\|x\|_{X_1} \tag{B.2}$$

for all $x \in X_1$. The space X_1 is compactly embedded *in X_2, if it is continuously embedded in X_2 and if each bounded sequence in X_1 has a convergent subsequence in X_2.*

Proposition B.12. *The space $H^1(\Omega)$ is continuously embedded in $L^2(\Omega)$, such that*

$$\|u\|_{L^2(\Omega)} \leq c\|u\|_{H^1(\Omega)} \tag{B.3}$$

for all $u \in H^1(\Omega)$ (see e. g. [64]). Note that we can choose $c = 1$ due to the definition of the norm $\|\cdot\|_{H^1(\Omega)}$.

The trace operator has been defined in Chapter 2. The trace theorem along with the subsequent statement is to be found for example in [3, 27].

Theorem B.13. *(*Trace theorem*) Let $\partial\Omega$ be of class C^1. The trace operator $\gamma : H^1(\Omega) \to L^2(\partial\Omega)$ is the unique continuous, linear operator such that $\gamma u = u|_{\partial\Omega}$ for all $u \in C(\overline{\Omega}) \cap H^1(\Omega)$.*

Proposition B.14. *As the space $C(\overline{\Omega}) \cap H^1(\Omega)$ is dense in $H^1(\Omega)$, there is a constant $c \geq 0$ such that*

$$\|u|_{\partial\Omega}\|_{L^2(\partial\Omega)} \leq c\|u\|_{H^1(\Omega)} \tag{B.4}$$

for all $u \in C^1(\overline{\Omega})$ (see [27]) and thus for all $u \in H^1(\Omega)$.

Remark B.15. *The existence and uniqueness of the Poisson problem $-\Delta u = f$ on a bounded domain Ω with C^1-boundary and Robin boundary conditions is treated in connection with the trace operator in [3].*

Bibliography

[1] Computer Solutions Europe AB. Partial differential equation toolbox user's guide.

[2] W. Arendt and T. Regińska. An ill-posed boundary value problem for the Helmholtz equation on Lipschitz domains. *Journal of Inverse and Ill-posed Problems*, 17(7):703–711, 2009.

[3] W. Arendt and K. Urban. *Partielle Differenzialgleichungen.* Spektrum Akademischer Verlag, 2010.

[4] W. Arendt and M. Warma. The Laplacian with Robin boundary conditions on arbitrary domains. *Potential Analysis*, 19(4):341–363, 2003.

[5] K. Atkinson and W. Han. *Theoretical Numerical Analysis.* Springer New York, 2001.

[6] G. Bao, Y. Chen, and F. Ma. Regularity and stability for the scattering map of a linearized inverse medium problem. *Journal of Mathematical Analysis and Applications*, 247(1):255–271, 2000.

[7] G. Bao and P. Li. Inverse medium scattering for the Helmholtz equation at fixed frequency. *Inverse Problems*, 21(5):16–21, 2005.

[8] G. Bao and P. Li. Inverse medium scattering problems in near-field optics. *Journal of Computational Mathematics*, 25(3):252–265, 2007.

[9] J.-P. Berenger. A perfectly matched layer for the absorption of electromagnetic waves. *Journal of Computational Physics*, 114(2):185–200, 1994.

[10] L. Borcea. Electrical impedance tomography. *Inverse Problems*, 18(6):R99–R136, 2002.

[11] D. Braess. *Finite Elemente: Theorie, schnelle Löser und Anwendungen in der Elastizitätstheorie.* Springer Berlin Heidelberg, 2013.

[12] H. Brezis. *Functional Analysis, Sobolev Spaces and Partial Differential Equations.* Springer Science+Business Media, 2011.

[13] M. Burger and B. Kaltenbacher. Regularizing Newton–Kaczmarz methods for nonlinear ill-posed problems. *SIAM Journal on Numerical Analysis*, 44(1):153–182, 2006.

[14] W. L. Chan, J. Deibel, and D. M. Mittleman. Imaging with terahertz radiation. *Reports on Progress in Physics*, 70(8):1325–1379, 2007.

[15] M. Cheney, D. Isaacson, and J. C. Newell. Electrical impedance tomography. *SIAM Review*, 41(1):85–101, 1999.

[16] I. Cioranescu. *Geometry of Banach Spaces, Duality Mappings and Nonlinear Problems.* Springer Science & Business Media, 2012.

[17] F. Colonius and K. Kunisch. Stability for parameter estimation in two point boundary value problems. *Journal für die reine und angewandte Mathematik*, 370:1–29, 1986.

[18] D. Colton, J. Coyle, and P. Monk. Recent developments in inverse acoustic scattering theory. *Siam Review*, 42(3):369–414, 2000.

[19] D. Colton and A. Kirsch. A simple method for solving inverse scattering problems in the resonance region. *Inverse Problems*, 12(4):383–393, 1996.

[20] D. Colton and R. Kress. *Inverse Acoustic and Electromagnetic Scattering Theory.* Springer New York, 2013.

[21] W. Demtroeder. *Experimentalphysik 2.* Springer Berlin Heidelberg, 2006.

[22] P. Deuflhard, H. W. Engl, and O. Scherzer. A convergence analysis of iterative methods for the solution of nonlinear ill-posed problems under affinely invariant conditions. *Inverse Problems*, 14(5):1081–1106, 1998.

[23] M. Elad, B. Matalon, and M. Zibulevsky. Coordinate and subspace optimization methods for linear least squares with non-quadratic regularization. *Applied and Computational Harmonic Analysis*, 23(3):346–367, 2007.

[24] J. Elstrodt. *Maß- und Integrationstheorie.* Springer Berlin Heidelberg, 2011.

[25] H. W. Engl, M. Hanke, and A. Neubauer. *Regularization of Inverse Problems.* Kluwer Academic Publishers, 2000.

[26] H. W. Engl, K. Kunisch, and A. Neubauer. Convergence rates for Tikhonov regularisation of non-linear ill-posed problems. *Inverse problems*, 5(4):523–540, 1989.

[27] L. C. Evans. *Partial Differential Equations.* Graduate studies in mathematics. American Mathematical Society, 1998.

[28] B. Ferguson, S. Wang, D. Gray, D. Abbot, and X.-C. Zhang. T-ray computed tomography. *Opt. Lett.*, 27(15):1312–1314, 2002.

[29] B. Ferguson, S. Wang, D. Gray, D. Abbott, and X.-C. Zhang. Towards functional 3D T-ray imaging. *Physics in Medicine and Biology*, 47(21):3735–3742, 2002.

[30] B. Ferguson and X.-C. Zhang. Materials for terahertz science and technology. *Nat Mater*, 1(1):26–33, 2002.

[31] W. Frei. Using perfectly matched layers and scattering boundary conditions for wave electromagnetics problems, Comsol Blog, 2015.

[32] D. Gilbarg and N. Trudinger. *Elliptic Partial Differential Equations of Second Order.* Springer Berlin Heidelberg, 2001.

[33] J. P. Guillet, B. Recur, L. Frederique, B. Bousquet, L. Canioni, I. Manek-Hönninger, P. Desbarats, and P. Mounaix. Review of terahertz tomography techniques. *Journal of Infrared, Millimeter, and Terahertz Waves*, 35(4):382–411, 2014.

[34] W. Hackbusch. *Theorie und Numerik elliptischer Differentialgleichungen.* Max-Planck-Institut für Mathematik in den Naturwissenschaften, Leipzig, 2005.

[35] J. Hadamard. *Lectures on Cauchy's Problem in Linear Partial Differential Equations.* Yale University Press, 1923.

[36] M. Haltmeier, R. Kowar, A. Leitao, and O. Scherzer. Kaczmarz methods for regularizing nonlinear ill-posed equations II: applications. *Inverse Problems and Imaging*, 1(3):507–523, 2007.

[37] M. Haltmeier, A. Leitao, and O. Scherzer. Kaczmarz methods for regularizing nonlinear ill-posed equations I: convergence analysis. *Inverse Problems and Imaging*, 1(2):289–298, 2007.

[38] M. Hanke. Regularizing properties of a truncated Newton-CG algorithm for nonlinear inverse

problems. *Num. Funct. Anal. Optim*, 18:971–933, 1997.

[39] M. Hanke, A. Neubauer, and O. Scherzer. A convergence analysis of the Landweber iteration for nonlinear ill-posed problems. *Numerische Mathematik*, 72(1):21–37, 1995.

[40] F. Heber, F. Schoepfer, and T. Schuster. A CG-type method in Banach spaces with an application in computerized tomography. *arXiv:1602.04036*, 2016.

[41] V. Isakov. *Inverse Problems for Partial Differential Equations.* Springer New York, 2006.

[42] B. Kaltenbacher. Some Newton-type methods for the regularization of nonlinear ill-posed problems. *Inverse Problems*, 13(3):729–753, 1997.

[43] B. Kaltenbacher, A. Neubauer, and O. Scherzer. *Iterative Regularization Methods for Nonlinear Ill-Posed Problems.* De Gruyter, 2008.

[44] B. Kaltenbacher, F. Schöpfer, and T. Schuster. Iterative methods for nonlinear ill-posed problems in Banach spaces: convergence and applications to parameter identification problems. *Inverse Problems*, 25(6):065003, 2009.

[45] A. Kirsch. *An Introduction to the Mathematical Theory of Inverse Problems.* Springer Science & Business Media, 2011.

[46] T. Knopp and T. M. Buzug. *Magnetic Particle Imaging: an Introduction to Imaging Principles and Scanner Instrumentation.* Springer Berlin Heidelberg, 2012.

[47] A. Lakhal. A decoupling-based imaging method for inverse medium scattering for Maxwell's equations. *Inverse Problems*, 26(1):015007, 2010.

[48] A. Lakhal and A. K. Louis. Locating radiating sources for Maxwell's equations using the approximate inverse. *Inverse Problems*, 24(4):045020, 2008.

[49] L. Landweber. An iteration formula for Fredholm integral equations of the first kind. *American journal of mathematics*, 73(3):615–624, 1951.

[50] S. Larsson and V. Thomee. *Partielle Differentialgleichungen und numerische Methoden.* Springer Berlin Heidelberg, 2005.

[51] B. Littau, J. Tepe, G. Schober, S. Kremling, T. Hochrein, P. Heidemeyer, T. Schuster, and M. Bastian. *Entwicklung und Evaluierung der Potenziale von Terahertz-Tomographie-Systemen.* Shaker Verlag, 2016.

[52] A. K. Louis. *Inverse und schlecht gestellte Probleme.* Vieweg+Teubner Verlag, 1989.

[53] A. K. Louis. Approximate inverse for linear and some nonlinear problems. *Inverse Problems*, 12(2):175–190, 1996.

[54] P. Maaß and R. Strehlow. An iterative regularization method for nonlinear problems based on Bregman projections. *Inverse Problems*, 32(11):115013, 2016.

[55] D. Mittleman, R. Jacobsen, and M. Nuss. T-ray imaging. *IEEE Journal of selected topics in quantum electronics*, 2(3):679–692, 1996.

[56] G. Narkiss and M. Zibulevsky. Sequential subspace optimization method for large-scale unconstrained optimization. *Technical report, Technion - The Israel Institute of Technology, Department of Electrical Engineering*, 2005.

[57] F. Natterer. *The Mathematics of Computerized Tomography.* Vieweg+Teubner Verlag, 1986.

[58] A. Neubauer. Tikhonov regularization of nonlinear ill-posed problems in Hilbert scales. *Applicable Analysis*, 46(1-2):59–72, 1992.

[59] J. Nocedal and S. J Wright. *Numerical Optimization.* Springer New York, 2006.

[60] W. Nolting. *Grundkurs Theoretische Physik 3, Elektrodynamik.* Springer Berlin Heidelberg, 2013.

[61] B. Recur, J.-P. Guillet, I. Manek-Hönninger, J.-C. Delagnes, W. Benharbone, P. Desbarats, J.-P. Domenger, L. Canioni, and P. Mounaix. Propagation beam consideration for 3D THz computed tomography. *Optics express*, 20(6):5817–5829, 2012.

[62] A. Rieder. On the regularization of nonlinear ill-posed problems via inexact Newton iterations. *Inverse Problems*, 15(1):309, 1999.

[63] A. Rieder. *Keine Probleme mit Inversen Problemen.* Vieweg+Teubner Verlag, 2003.

[64] S. Sauter and C. Schwab. *Randelementmethoden.* Vieweg+Teubner Verlag, 2004.

[65] F. Sauvigny. *Partielle Differentialgleichungen der Geometrie und der Physik.* Springer Berlin Heidelberg, 2005.

[66] F. Scheck. *Theoretische Physik 3.* Springer Berlin Heidelberg, 2010.

[67] O. Scherzer. The use of Morozov's discrepancy principle for Tikhonov regularization for solving nonlinear ill-posed problems. *Computing*, 51(1):45–60, 1993.

[68] F. Schöpfer, A. K. Louis, and T. Schuster. Metric and Bregman projections onto affine subspaces and their computation via sequential subspace optimization methods. *Journal of Inverse and Ill-Posed Problems*, 16(5):479–206, 2008.

[69] F. Schöpfer and T. Schuster. Fast regularizing sequential subspace optimization in Banach spaces. *Inverse Problems*, 25(1):015013, 2009.

[70] T. Schuster, B. Kaltenbacher, B. Hofmann, and K. S. Kazimierski. *Regularization Methods in Banach Spaces.* De Gruyter, 2012.

[71] J. Tepe, T. Schuster, and B. Littau. A modified algebraic reconstruction technique taking refraction into account with an application in terahertz tomography. *Inverse Problems in Science and Engineering*, 2016.

[72] A. Wald and T. Schuster. Sequential subspace optimization for nonlinear inverse problems. *Journal of Inverse and Ill-posed Problems*, 25(4):99–117, 2016.

[73] S. Wang, B. Ferguson, D. Abbott, and X.-C. Zhang. T-ray imaging and tomography. *Journal of Biological Physics*, 29(2-3):247–256, 2003.

[74] S. Wang and X.-C. Zhang. Pulsed terahertz tomography. *Journal of Physics D: Applied Physics*, 37(4):R1–R36, 2004.

[75] Y. M. Wang and W. C. Chew. An iterative solution of the two-dimensional electromagnetic inverse scattering problem. *International Journal of Imaging Systems and Technology*, 1(1):100–108, 1989.

[76] D. Werner. *Funktionalanalysis.* Springer New York, 2011.

[77] Q. Wu, T. D. Hewitt, and X.C. Zhang. Twodimensional electrooptic imaging of THz beams. *Applied Physics Letters*, 69(8):1026–1028, 1996.

[78] X. Yin, B. W.-H. Ng, B. Ferguson, and D. Abbott. Wavelet based local tomographic image using terahertz techniques. *Digital Signal Processing*, 19(4):750–763, 2009.

[79] X.-C. Zhang. Terahertz wave imaging: horizons and hurdles. *Physics in Medicine and Biology*, 47(21):3667–3677, 2002.

[80] L. Zschiedrich, R. Klose, A. Schaedle, and F. Schmidt. A new finite element realization of the perfectly matched layer method for Helmholtz scattering problems on polygonal domains in two dimensions. *Journal of Computational and Applied Mathematics*, 188(1):12–32, 2006.